

DOCTORAL THESIS IN PHYSICS

**ab initio Calculations for Co nanoparticles,
Fe₂CoO₄ and Co₂FeO₄ Spinel and,
Ni–Mn–Ga & Ni–Mn–Sn Heusler alloys**

Mahboobeh Safarabadi

University of Bielefeld
Department of Physics
Thin Films and Physics of Nanostructures

May 2014

Declaration

I hereby declare that I wrote this thesis by myself and used none but the indicated resources.

Mahboobeh Safarabadi

Bielefeld, March 2014

*„To my Parents,
the Angels without wings of my life.“*

Contents

1	Introduction	1
2	Density Functional Theory (DFT)	4
	2.1 Hartree-Fock Approximation	6
	2.2 Electron Correlation	7
	2.3 Exchange Interaction	7
	2.4 Pseudopotentials	7
3	SPRKKR Method	10
	3.1 Dyson Equation	11
	3.2 Transition Matrix	11
4	DOS Calculations for Co and Fe₂CoO₄ and Co₂FeO₄	13
	4.1 Cobalt characterization in different Phases	13
	4.2 DOS Calculation for Cobalt in three Phases	14
	4.3 Spinel Ferrites Compounds	20
5	Heusler Alloys and Shape Memory Effect	30
	5.1 Structural Properties of Magnetic Heusler Alloys	31
	5.2 Magnetic field Effect on Strain	36
	5.3 Jahn-Teller Effect	37
	5.4 Slater-Pauling rule	38
6	Shape Memory Effect in Ni₂MnGa	39
	6.1 Martensitic structure of Ni ₂ MnGa	39
	6.2 Composition and Temperature dependence of the Crystal Structure of Ni-Mn-Ga alloys	40
	6.3 Density of States Calculation for Ni ₂ MnGa	40
7	Shape Memory Effect in Ni–Mn–Sn alloy	54
	7.1 Density of States Calculation for Ni ₂ MnSn	54
8	Multilayer systems consisting of Ni₂MnGa and Ni₂MnSn	58
9	Shape Memory Effect of Non-Stoichiometric Compounds	84
10	Summary and Conclusions	90
11	Outlook	93
	Bibliography	94
	Acknowledgements	101

1 Introduction

The main aim of this work is to apply „ab initio calculations“ either DFT- or KKR Green's function- based to gain further information about the band structure of materials and stability in different phases such as Co nanoparticles, Fe_2CoO_4 and Co_2FeO_4 ferrite spinels and some kinds of Heusler alloys. To fulfill this goal, different Simulation Programms including elk, Quantum-Espresso (*opEn Source Package for Research in Electronic Structure, Simulation, and Optimization*) and SPRKKR (*spin-polarized relativistic Korringa-Kohn-Rostoker*) have been used.

In chapter 2 the Density Functional Theory (DFT) is described in detail; in this work Density Of States (DOS) of Cobalt in 3 fcc-, hcp- and ϵ -structures have been calculated by using „Elk program“ which is a DFT-based program. But to do the same calculations for „ Fe_2CoO_4 “ and „ Co_2FeO_4 “ spinels, due to underestimating the band gaps in these compounds, Elk-code was not proper to do these calculations. In order to solve the problem DFT+U based calculations were used, where U is the „Coulomb Potential“ which should be considered to simulate better the real system. In fact the position of Valence Band Maxima (VBM) has been corrected to a large extent by adding Hubbard “ U_{eff} ” to the transition metal d-orbital. „ U_{eff} is generally expressed as the difference between parameters U and J. The Hubbard U is the Coulomb-energetic cost to place two electrons at the same site, and J is an approximation to the Stoner exchange parameter“ [1] which defines ferromagnets. For this thesis with consideration the available calculated results for DOS in literature [2, 3], it has been tried to change U_{eff} as a parameter in the way that band gaps presented in those references be attained. Afterwards experimental results obtained by our experimentists have also confirmed the calculation results which showed that Fe_2CoO_4 is an insulator and Co_2FeO_4 is a half-metal. Doing these calculations with elk-code which is an „all-electron potential“ was too time-consuming, thus the „Quantum-Espresso“ program which contains „pseudopotentials“ has been used for spinels and Heusler alloys. The kinds of pseudopotentials and their basics are also explained in chapter 2.

In chapter 3 the SPRKKR method enabling to do calculations for off-stoichiometric Heusler alloys is introduced.

As it is well-known the aim of spintronics is searching for highly spin polarized materials to enhance tunneling magnetoresistance (TMR) of magnetic tunnel junctions (MTJs). There are several ways to achieve high spin-polarization; the most practical way is to apply fully spin-polarized ferromagnetic metals named half-metals (HM). Another possibility is to utilize the features of the band structure of tunnel barrier materials such as MgO to filter the electronic wave functions according to their symmetry. The least explored way is using the spin-filtering effect based on ferromagnetic or ferrimagnetic insulating barriers. In spin filtering phenomenon electrons with spin parallel to the magnetization of the material will be low scattered and transit nearly hundred percent through the material in contrast to other electrons will be strongly scattered. As a result spin-dependent gap should result in a spin-dependent barrier. „Since the tunneling probability depends

exponentially on the barrier height, the spin filtering efficiency can be very high [4].“
 Fe_2NiO_4 , Fe_2CoO_4 , and Fe_2MnO_4 are candidates for spin filtering.

Chapter 4 contains the calculated Density Of States for Co in three phases which also have been observed in experiments and for Co_2FeO_4 and Fe_2CoO_4 spinels.

The prospect of exploiting the latent energy in the systems has arisen recently. The origin of this energy is variation the entropy of the system resulted from the changing the macroscopic properties of the system such as volume, temperature and strain on it and further for the ferromagnetic systems could be also attained by applying an external magnetic field. As a result the Heusler alloys which show a shape memory effect and among them Ni_2MnGa which is also ferromagnetic have attracted high attention. Ni_2MnGa shows a shape memory effect originated in the martensitic transition which takes place through cooling about 200K from the cubic $L2_1$ Heusler austenite structure to a tetragonal martensite phase. The origin of this transition is lowering the energy of system due to the hybridization between d-electrons of Ni with p-electrons of Ga atoms which results in a lowering in tetragonality (c/a) of the unit cell. This transformation is a simple contraction along [100] direction of the cubic phase without any change in atomic positions. There is a strong deformation of the cell ($c/a=0.94$) but a light change in cell volume of only $\approx 1\%$. The outstanding point for this transformation is that in spite of a strong deformation of the unit cell, this transformation is reversible [5,6]. An alternative for Ni-Mn-Ga alloy system could be Ni-Mn-Sn-based Heusler alloys. „The Martensitic Transformation (MT) in offstoichiometric Ni-Mn-Sn-based alloys is often accompanied by the abrupt changes of magnetization and resistance“ [7]. Quantum-Espresso and SPRKKR programs by applying PBE (Perdew, Burke and Ernzerhof), generalized gradient approximation (GGA), as exchange-correlation functional within the spin-polarized scalar relativistic approximation have been used to calculate the DOS for stoichiometric Ni_2MnGa and Ni_2MnSn and for offstoichiometric compounds such as $\text{Ni}_{54.5}\text{Mn}_{20.5}\text{Ga}_{25}$ and $\text{Ni}_{47}\text{Co}_{3.1}\text{Mn}_{36.6}\text{Sn}_{13.3}$ for both austenite and martensite states SPRKKR program has been used.

Chapter 5 introduces the Heusler alloys and their applications based on magnetic and structural transitions taken from literature. Structural properties in both austenite and martensite states, effect of magnetic field on strain observed in these alloys have been discussed in this chapter.

In Chapter 6 shape memory effect for Ni_2MnGa has been studied by calculating the Density Of States and investigating it at Fermi level for the three minima of energies taken from literature [8]. And the stability between these three phases are discussed as well. The charge density distribution is also calculated for these three minima by utilizing Q-Espresso program. Total magnetic moment and contributions associated with individual atoms in Ni_2MnGa as a function of tetragonality taken from literature [8] are also mentioned in this chapter

Chapter 7 involves study of shape memory effect in Ni_2MnSn alloy which seems to be a good alternative for Ni_2MnGa . The charge density distribution and total magnetic moment and contributions associated with individual atoms in Ni_2MnSn as

a function of tetragonality is also calculated by applying Quantum-espresso code and presented in this chapter.

In chapter 8 a series of multilayers consisting of Ni_2MnGa and Ni_2MnSn in different configurations have been investigated to study the magnetic moment behaviors of individual atoms inside the layers and in interfaces and as well the possibility to occur martensitic transition and finally spin polarization is also studied in these configurations.

Chapter 9 presents the calculated DOS and magnetic moments resulting of SPRKKR simulation for two off-stoichiometric compounds including $\text{Ni}_{54.5}\text{Mn}_{20.5}\text{Ga}_{25}$ and $\text{Ni}_{47}\text{Co}_{3.1}\text{Mn}_{36.6}\text{Sn}_{13.3}$.

Chapter 10 involves summary and conclusions and finally chapter 11 including outlook for the further investigations is followed.

2 Density Functional Theory (DFT)

The aim of most ab initio methods is to solve the time-independent, non-relativistic Schrödinger equation. In 1964 Hohenberg & Kohn discovered all properties of a stationary electronic system can be described by its ground-state density $n_0(\mathbf{r})$; that is one scalar function of position. The density is a physical observable quantity and depends only on three spatial coordinates. Hohenberg & Kohn also disclosed a variational principle in terms of the density whose minimum gives the exact ground state density. Within the Kohn-Sham approach, the electrons are presumed as non interacting particles under an effective external potential, V_{KS} . The effective potential is usually written as follows

$$V_{KS}(\mathbf{r}) = V_{\text{ext}}(\mathbf{r}) + V_{\text{Hartree}}(\mathbf{r}) + V_{xc}(\mathbf{r}) \quad (2.1)$$

where the first term is the external potential (normally the Coulomb interaction between the electrons and the nuclei), whereas the second term accounts for the classical electrostatic interaction between the electrons. All other many-body complex effects are contained in the unknown exchange-correlation (xc) functional dependence on the density, V_{xc} . Whether the solution of the Schrödinger equation results in the exact solutions depends on the accuracy of the approximation to the xc potential. Kohn & Sham proposed a simple approximation for V_{xc} as well, named the „local density approximation (LDA)“. This approach is based on the homogeneous electron gas and turned out to be quite accurate for a number of applications, and is still widely used. Fig. 2-1 presents the relation established by Hohenberg and Kohn between exact many-body interacting system with a non-interacting auxiliary system. The assumption of density as the fundamental variable, and the Kohn-Sham approach construct the basis of „density functional theory (DFT)“. DFT provides a powerful tool for computations of the quantum state of atoms, molecules and solids. It was built in its initial naïve and approximative version by Thomas and Fermi immediately after the foundation of the quantum mechanics, in 1927.

The Schrödinger equation can be further simplified if the significant differences between the masses of nuclei and electrons are taken into account. Hence, the nuclei move much slower than the electrons. The practical consequence is to consider the electrons as moving particles in the field of fixed nuclei. This is the famous „Born-Oppenheimer approximation“.

From the Kohn-Sham orbitals, $\varphi_i(\mathbf{r},t)$, the electron density can be calculated by following formula

$$n(\mathbf{r},t) = \sum_i^N |\varphi_i(\mathbf{r},t)|^2 \quad (2.2)$$

In 1996, Perdew, Bruke, and Ernzerhof proposed an exchange-correlation functional referred to PBE which is a subset of GGA functionals that satisfy as many formal properties and sacrifice only those terms to be energetically less important (Perdew et al., 1996). In this work PBE functionals are used to approximate the exchange-correlation potential between electrons.[9, 10, 11, 12] Fig. 2-2 represents a schematic self-consistent loop for solution the Kohn-Sham equations.

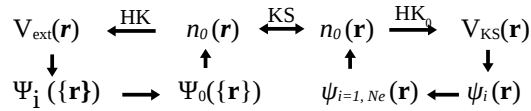


Figure 2-1. Schematic representation of *Kohn-Sham ansatz*. The notation HK_0 denotes the *Hohenberg-Kohn theorem* applied to the non-interacting problem. The arrow labeled KS provides the connection in both directions between the many-body and independent-particle systems, so that the arrows connect any point to any other point. Therefore, in principle, solution of the independent-particle *Kohn-Sham* problem determines *all properties* of the full many-body system [12].

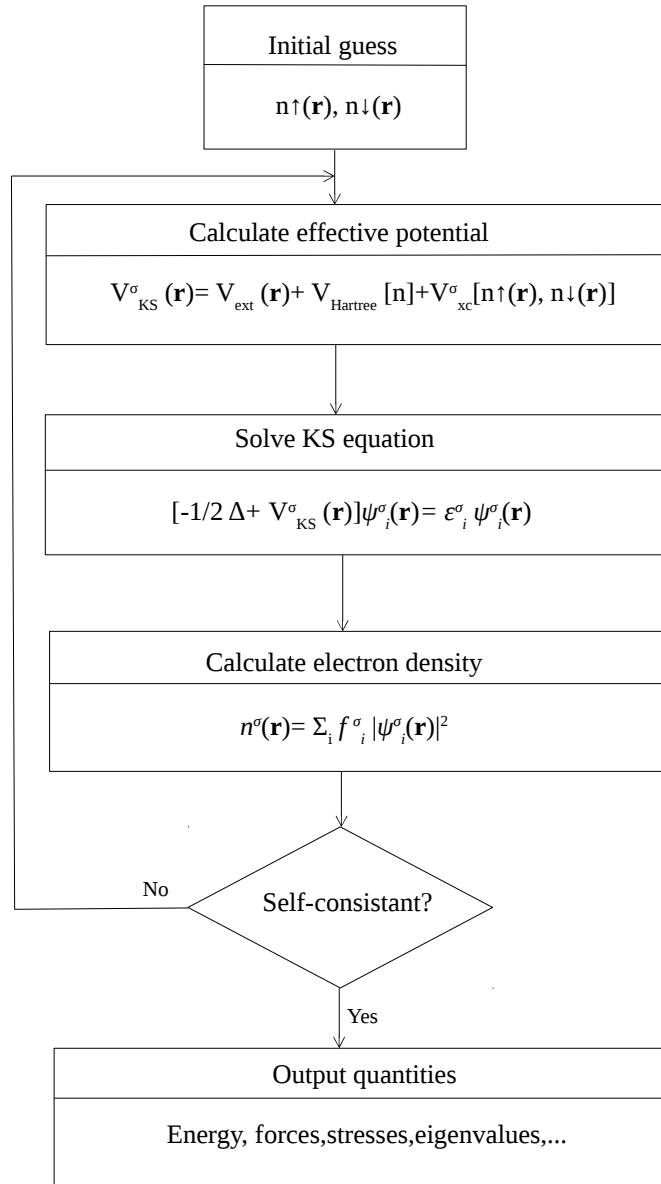


Figure 2-2. Schematic representation of the self-consistent loop for solution of *Kohn-Sham* equations. In general, this loop must be iterated simultaneously for both spin-ups and -downs, with the potential as a functional of the density of both spins for each spin [12].

2.1 Hartree-Fock Approximation

The Hartree-Fock (HF) scheme is the simplest approximation yet purposed to resolve the complex many-body wave function equation where a system consists of M nuclei and N electrons. It approximates the N -electron wave function by an antisymmetrized product of N one-electron wave functions, $\chi_i(\mathbf{x}_i)$. John C. Slater introduced the „Slater determinants, Φ_{SD} “, based on utilizing matrices to ensure the antisymmetry of a wave function [13]. The one-electron functions, $\chi_i(\mathbf{x}_i)$, called „spin orbitals“ are composed of a spatial orbital $\varphi_i(\mathbf{r})$ and a spin function $\sigma(s)$; where σ represents spin direction of electrons.

$$\chi(\mathbf{x}) = \varphi(\mathbf{r}) \sigma(s) \quad (2.3)$$

for such a system the HF energy is given by

$$E_{HF} = \langle \Phi_{SD} | \hat{H} | \Phi_{SD} \rangle = \sum_i^N (i|\hat{h}|i) + \frac{1}{2} \sum_i^N \sum_j^N (ii|jj) - (ij|ji) \quad (2.4)$$

where

$$(i|\hat{h}|i) = \int \chi_i^*(\mathbf{x}_1) \left\{ \frac{-1}{2} \nabla^2 - \sum_A^M \frac{Z_A}{r_{1A}} \right\} \chi_i(\mathbf{x}_1) d\mathbf{x}_1 \quad (2.5)$$

defines the one electron contribution to the Hamiltonian due to its kinetic energy and the electron-nucleus attraction and the following integrals

$$(ii|jj) = \iint |\chi_i(\mathbf{x}_1)|^2 \frac{1}{r_{12}} |\chi_j(\mathbf{x}_2)|^2 d\mathbf{x}_1 d\mathbf{x}_2 \quad (2.6)$$

$$(ij|ji) = \iint \chi_i(\mathbf{x}_1) \chi_j^*(\mathbf{x}_1) \frac{1}{r_{12}} \chi_j(\mathbf{x}_2) \chi_i^*(\mathbf{x}_2) d\mathbf{x}_1 d\mathbf{x}_2 \quad (2.7)$$

are the so-called „Coulomb“ and „exchange integrals“, respectively which simply represent the possible interactions between two electrons.

These N equations can be written in the form of eigenvalue equations, $f_i \chi_i(\mathbf{x}) = \varepsilon_i \chi_i(\mathbf{x})$, where the orbital energies, ε_i , are the eigenvalues of the operators f_i . The Fock operator, f , is an effective one-electron operator defined as

$$f = \frac{-1}{2} \nabla_i^2 - \sum_A^M \frac{Z_A}{r_{iA}} + V_{HF}(i) \quad (2.8)$$

The first two terms are the kinetic energy and the potential energy due to the electron-nucleus attraction. The Hartree-Fock potential, $V_{HF}(i)$, is the average repulsive potential experienced by the i 'th electron. Generally, V_{HF} comprises of two Coulomb, J , and exchange, K , operators:

$$V_{HF}(\mathbf{x}_1) = \sum_j^N (\hat{J}_j(\mathbf{x}_1) - \hat{K}_j(\mathbf{x}_1)) \quad (2.9)$$

The Coulomb operator \hat{J} is defined as

$$\hat{J}_j(\mathbf{x}_1) = \int |\chi_j(\mathbf{x}_2)|^2 \frac{1}{r_{12}} d\mathbf{x}_2 \quad (2.10)$$

and represents the potential that an electron at position \vec{x}_1 experiences due to the average charge distribution of another electron in spin orbital χ_j . The exchange operator \hat{K} has no classical equivalent and can only be defined through its effect when operating on a spin orbital as follows: [9]

$$\hat{K}_j(\mathbf{x}_1)\chi_i(\mathbf{x}_1) = \int \chi_j^*(\mathbf{x}_2) \frac{1}{r_{12}} \chi_i(\mathbf{x}_2) d\mathbf{x}_2 \chi_j(\mathbf{x}_1) \quad (2.11)$$

2.2 Electron Correlation

It is noted that the „Slater determinant“, Φ_{SD} , as an approximate wave function never corresponds to the exact wave function. In the Hartree-Fock scheme the electrons come often too close to each other because the electrostatic interaction is treated in an average manner. As a consequence, the electron-electron repulsion term is too large resulting in E_{HF} lies above E_0 . The difference between these two energies is named the „correlation energy“ by Löwdin in 1959 and is defined as follows [9]

$$E_C^{HF} = E_0 - E_{HF} \quad (2.12)$$

2.3 Exchange Interaction

The exchange energy or interaction is the energy required to align all other existing spins in the system with itself. Mathematically, it can be expressed in terms of the dot-product of spin operators. With this assumption that the orbital components are fixed, the exchange Hamiltonian can be written as follows:

$$H_{ex} = \sum_{i,j} J_{ij} \mathbf{S}_i \cdot \mathbf{S}_j \quad (2.13)$$

where J_{ij} is called the „exchange-coupling constant“. Exchange-couplings are called „ferromagnetic“ or „antiferromagnetic“, if they align parallel or antiparallel to the interacting spins, respectively. [14]

2.4 Pseudopotentials

As it will be seen in this thesis the „elk-program“ which treats all valence and core electrons in the same way is not able to do band structure calculations for compounds including transition metal oxides. The reason is the rapidly fluctuations of electron densities in the vicinity of atomic cores resulted from strongly attractive potential of the nucleus. In order to resolve this problem a new generation of potentials named „Pseudopotentials“ are established which discard the effect of bare core, such as „norm-conserving“ and „ultrasoft-pseudopotentials“. In the next sections „Pseudopotentials“ properties will be discussed. [15, 16]

2.4.1 Norm-Conserving and Ultrasoft Pseudopotentials

In order to construct pseudopotentials it is needed to consider appropriate electrons configurations (e.g., Fe $3d^7 4s^1$) and pseudopotential radii, r_c which are spherical cutoff radii to truncate potential to make it calculable. Generally, pseudopotentials must fulfill the following conditions:

- They must have no nodes to avoid using higher cutoff radius (Fig.2-4).
- Above the cutoff radius pseudo-functions and -potentials behave like the exact ones.
- If the charge surrounded within the pseudopotential radius is equal to that of the all-electron potential, the „norm-conserving“ pseudopotential will be resulted.
- The eigenvalues of equations applying pseudofunctions must be similar to those of the all-electron solution at least for the reference configuration.

In 1990, Vanderbilt suggested to drop „the norm-conserving“ requirement and just be needed that the spheres centered on different atoms not be overlapped which will result in a larger cutoff radius. Hence, the pseudo-functions and -potentials will be much softer (Fig. 2-3). [15, 16]

Figure 2-3. Schematic representation of the pseudofunction of an ultrasoft pseudopotential compared to the pseudofunction of a norm-conserving pseudopotential [15].

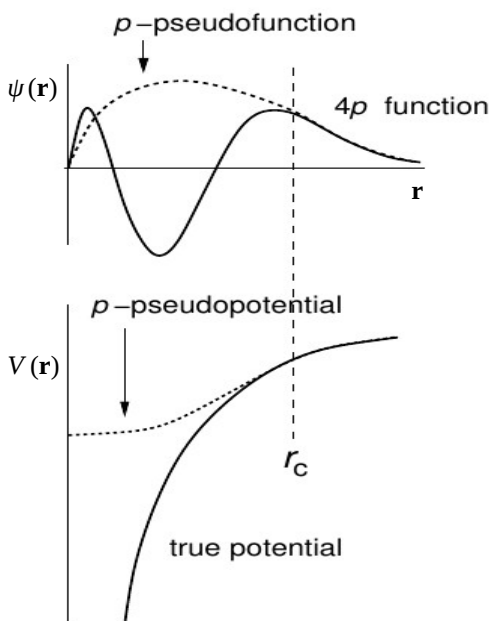
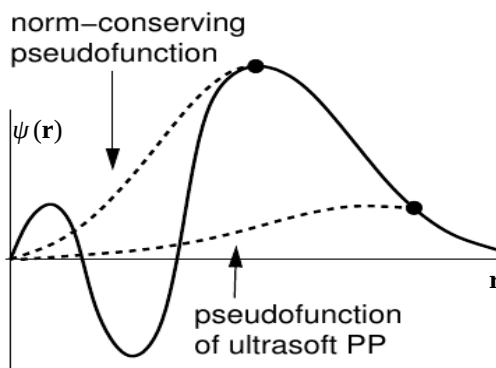


Figure 2-4. Schematic view of pseudofunctions and corresponding pseudopotentials. The pseudofunction is smooth and has no nodes in contrast to the „true“ one. At $r > r_c$, the pseudofunction coincides the all-electron wavefunction [15].

2.4.2 Pseudopotentials in Spin-Polarised Calculations

For magnetic materials, the peak in the d-wavefunction is shifted outward to make the pseudopotentials softer, as a result, the valence-core overlap is artificially reduced. As a result the spin enhancement factor $\xi(\mathbf{r})$, Eq. (2.14), is overestimated, where $m(\mathbf{r})$ is the magnetic moment of atoms and $n_{\text{valence}}(\mathbf{r})$ and $n_{\text{core}}(\mathbf{r})$ are the density of states for valence and core electrons, respectively.

$$\xi(\mathbf{r}) = \frac{m(\mathbf{r})}{n_{\text{valence}}(\mathbf{r}) + n_{\text{core}}(\mathbf{r})} \quad (2.14)$$

Thus pseudopotentials fail in spin-polarised calculations. [17]

3 SPRKKR Method

The KKR method of band-structure calculation was introduced in the 1940s by Korringa and Kohn and Rostoker. But first after developing by application of the „multiple scattering theory“, this method became popular. This implies that the information on the electronic structure of a system is not expressed in terms of Bloch wave functions and eigenvalues but the corresponding Green’s function leading to an extreme flexibility of the method. This method covers electronic structure calculation in non-relativistic, scalar-relativistic as well as fully relativistic modes. Although it is not counted among the fastest band structure methods, it is usually regarded as a very accurate technique. The advantage of the KKR method lies in this fact that allows to express the Green’s function in terms of single-site scattering and geometrical or structural quantities. A second outstanding feature of the KKR method is the Dyson equation relating the Green’s function of a perturbed system with the Green’s function of the corresponding unperturbed reference system. Because of this property, the KKR Green’s function method allows to deal with substitutional disorder including both impurities and concentrated alloys. Hence for this thesis SPRKKR method is used to do density of state calculations for stoichiometric and offstoichiometric Heusler alloys to investigate DOS at Fermi level more accurately. The spin-polarized relativistic Korringa-Kohn-Rostoker Green’s function method is based on the following Dirac-Hamiltonian,

$$\left[\frac{\hbar}{i} c \boldsymbol{\alpha} \cdot \nabla + \beta m c^2 + V(\mathbf{r}) + \beta \boldsymbol{\sigma} \cdot \mathbf{B}_{\text{eff}}(\mathbf{r}) \right] \psi_k(\mathbf{r}, E) = E \psi_k(\mathbf{r}, E) \quad (3.1)$$

$$V = V_n + V_H + V_{xc} \quad (3.2)$$

In this equation the potential V contains the Coulomb potential due to the nuclei (V_n) and the other electrons (V_H). The contribution due to the exchange-correlation potential has been split into a spin-averaged part (V_{xc}) included in V and a spin-dependent part ($\beta \boldsymbol{\sigma} \cdot \mathbf{B}_{\text{eff}}$). The effective magnetic field \mathbf{B}_{eff} in the latter term arises from the dependence of the exchange-correlation energy E_{xc} on the spin magnetization density \mathbf{m} :

$$\mathbf{B}_{\text{eff}}(\mathbf{r}) = \mathbf{B}_{\text{ext}}(\mathbf{r}) + \frac{\partial E_{xc}[n, \mathbf{m}]}{\partial \mathbf{m}(\mathbf{r})} \quad (3.3)$$

where n is the particle density. The spin-dependent term in Eq.(3.1) strongly reduces the symmetry.

In the *Spin-Polarized Relativistic Korringa-Kohn-Rostoker* (SPRKKR) Green’s function method the differential Schrödinger equation,

$$[-\nabla^2 + V(\mathbf{r})] \psi_k(\mathbf{r}, E) = E_k \psi_k(\mathbf{r}, E) \quad (3.4)$$

is replaced by the integral Lippmann-Schwinger equation,

$$\psi_k(\mathbf{r}, E) = e^{i\mathbf{k} \cdot \mathbf{r}} + \int d^3 \mathbf{r}' G_0(\mathbf{r}, \mathbf{r}', E) V(\mathbf{r}') \psi_k(\mathbf{r}', E) \quad (3.5)$$

representing scattering of a plane wave at a target with free electron Green's function $G_0(\mathbf{r}, \mathbf{r}', E)$. [18,19,20,21,22,23]

Principle of multiple scattering theory- The concept of XAFS (X-ray Absorption Fine Structure) theory is used to calculate electronic structure. In this way that a perturbation is applied to the Hamiltonian of the system to get information about the structure configuration and energy levels of atoms (Fig.3-1).

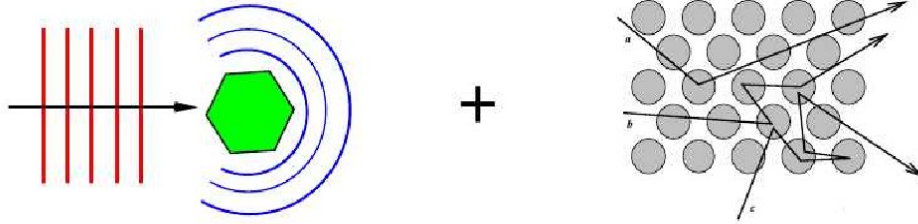


Figure 3-1. SPRKKR separates structural and scatterers information [21].

3.1 Dyson Equation

If H_0 and $H = H_0 + V(\mathbf{r})$ are Hamiltonians of system before and after perturbation, respectively, where $V(\mathbf{r})$ is the applied perturbation, Dyson equations are as follows:

$$(E - H_0)G_0(\mathbf{r}, \mathbf{r}', E) = \delta(\mathbf{r} - \mathbf{r}') \quad (3.6)$$

$$(E - H)G(\mathbf{r}, \mathbf{r}', E) = \delta(\mathbf{r} - \mathbf{r}') \quad (3.7)$$

if the wave functions before and after perturbation are defined by plane and spherical waves, respectively, the perturbed system is defined by

$$\Psi(\mathbf{r}, E) = e^{i\mathbf{k}\cdot\mathbf{r}} + f(\theta, \varphi) \frac{e^{i\mathbf{k}\cdot\mathbf{r}}}{r} \quad (3.8)$$

where the first term represents the incoming plane waves (φ_k) and the second term the outgoing spherical waves ((Fig.3-1) and $f(\theta, \varphi)$ is the scattering amplitude, then the free electron Green's function is [24]

$$G_0(\mathbf{r}, \mathbf{r}', E) = \frac{1}{(2\pi)^3} \int d^3\mathbf{k} \frac{e^{i\mathbf{k}\cdot\mathbf{r}} e^{-i\mathbf{k}\cdot\mathbf{r}'}}{E - k^2} = \frac{-1}{4\pi} \frac{e^{-i\sqrt{E}|\mathbf{r}-\mathbf{r}'|}}{|\mathbf{r}-\mathbf{r}'|} \quad (3.9)$$

3.2 Transition Matrix

To solve the Lippmann-Schwinger equation a transition or T-matrix which relates the unperturbed and perturbed systems via $V|\psi_k\rangle = T|\varphi_k\rangle$ defined by inserting $|\psi_k\rangle = |\psi_0\rangle + g_0 V |\psi_k\rangle$ as follows where $G_0(\mathbf{r}, \mathbf{r}', E) = \langle \mathbf{r} | g_0(E) | \mathbf{r}' \rangle$

$$T = V + Vg_0V + Vg_0Vg_0V + \dots \quad (3.10)$$

by substituting T in the Dyson equation in the same way one is led to $Vg = Tg_0$ and the Lippmann-Schwinger and Dyson equations by inserting T become

$$\text{Lippmann-Schwinger equation } |\psi_1\rangle = |\psi_0\rangle + g_0 T |\psi_0\rangle \quad (3.11)$$

$$\text{Dyson equation } g = g_0 + g_0 T g_0 \quad [24]. \quad (3.12)$$

4 DOS Calculations for Co, Fe₂CoO₄ and Co₂FeO₄

4.1 Cobalt characterization in different Phases

The materials involving cobalt are very interesting and desirable for academic researches and industrial applications due to their particular magnetic and electronic properties being useful as magnetic data storage or as spin-current source and spin-filters in spintronic field. Metallic cobalt can crystallize in three different crystal structures: (1) hcp, hexagonal closed-packed (α -phase), (2) fcc, face-centered cubic (β -phase) and (3) primitive cubic phase (ϵ -phase).

Under atmospheric pressure Cobalt is only in two structures stable; below 425°C α -phase and at higher temperatures β -phase. Hence, small temperatures or pressure variations lead to changes in the crystal phase. In ϵ -phase, the Co particles present a complex cubic primitive structure (P4₁32) similar to the manganese β -phase with 20 atoms in a cubic unit cell with 6.09Å side. The ϵ -structure is considered as a soft magnetic material (like β -phase) and its magnetic properties favor the formation of ordered films applicable in magnetic recording. The ϵ -phase seems to be a good precursor to obtain α -Co nanoparticles desired for magnetic storage uses.

These three phases possess similar energetic stabilities that is also confirmed through the calculations done for this thesis as it is discussed in next section (Table 4-I). Studies show a strong correlation between crystal structure and magnetic properties in Co-based materials. Although α - and β -Co phases can coexist at different conditions, at room temperature and atmospheric pressure the α -phase is more stable which is also confirmed through calculations done for this thesis.

There is strong relation between crystal structure and the magnetic properties of cobalt. The α -phase (hcp structure) with high magnetic coercivity is proper for permanent magnet applications such as recording media, while the more symmetric low coercivity β -phase (fcc structure) is good for soft magnetic applications.

Both hcp and fcc structures are consisted of close-packed atoms but they differ in the stacking sequence of the [111] plane. Fig. 4-1 shows TEM image of 0.1 micrometer cobalt crystals with epsilon structure. Fig. 4-2 displays an X-ray powder diffraction pattern of these 3 phases of cobalt to compare. [25, 26, 27,28]

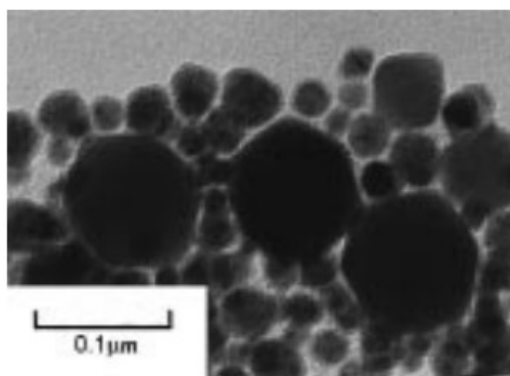


Figure 4-1. TEM image of 0.1 μm cobalt crystals with the ϵ -cobalt structure [28].

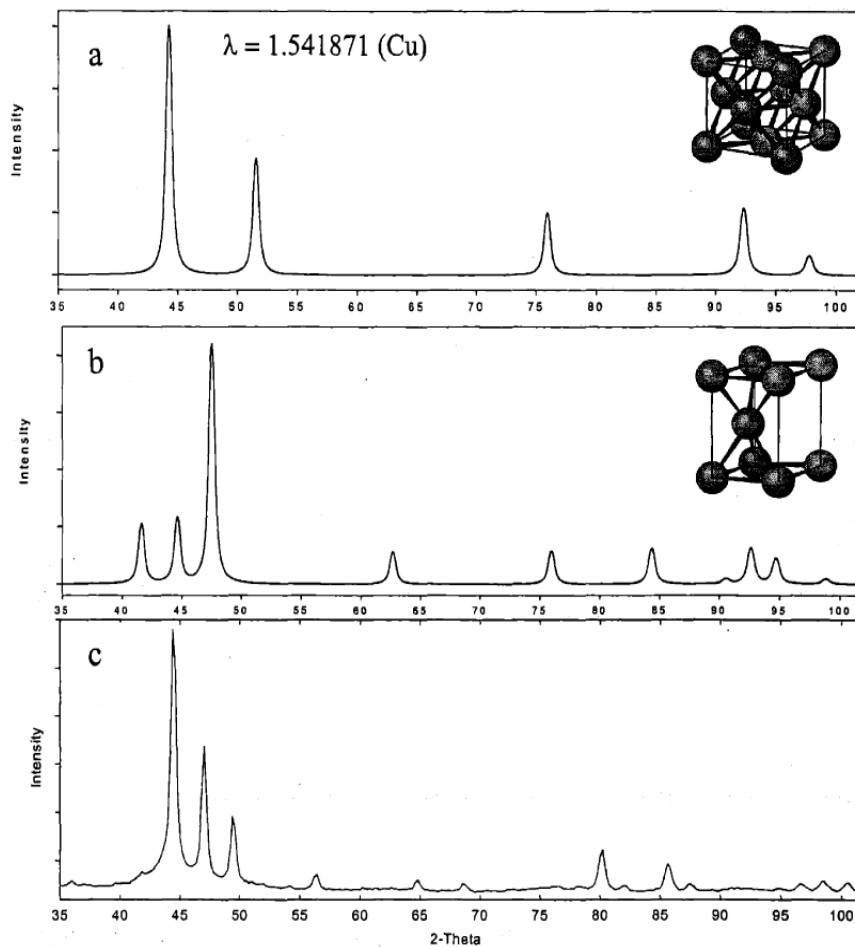


Figure 4-2. Comparison between two known diffraction patterns of (a) fcc-cobalt (simulated) and (b) hcp-cobalt (simulated) with (c) ϵ -cobalt (experimental) [27].

4.2 DOS Calculation for Cobalt in three Phases

For this section to do calculations Elk code [29], a DFT-based program is used, in chapter 2 a brief description has been presented to introduce the mechanism of DFT-based programs. Since Cobalt has a magnetic structure, spin polarized version of DFT solving the Schrödinger equation separately for spin up and down electrons with considering PBE functionals as exchange-correlation potentials are used. The initial unit cell constants are taken from the experimental lattice constants. For the α -, β -, and ϵ -Co the unit cell involves 2, 4, and 20 atoms, respectively. The results obtained correspond to 0 K. The ϵ -Co, described by Dinega et al. [27] posses a cubic structure (space group $P4_132$) with a unit cell similar to that of β -manganese. This structure contains 20 cobalt atoms per unit cell dependent on the position are divided in two types: eight atoms of type I and twelve atoms of type II. These two types of

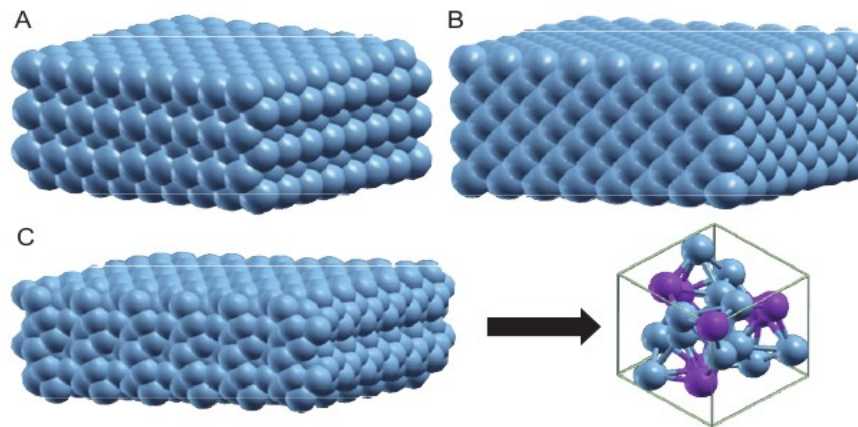


Figure 4-3. A sketch of different cobalt structures: (A) hcp or α -phase, (B) fcc or β -phase, and (C) ϵ -phase and its unit cell with specified two types of atoms [25].

atoms differ in the number of neighbors. An ideal close-packed structure has twelve nearest neighbors, whereas ϵ -cobalt has only three nearest neighbors for Type I atoms and two nearest for Type II ones (Fig. 4-3). [25,27,28]

The calculated total energy per cobalt atom shows that, for generalized-gradient approximation (GGA) calculations, the α -Co phase is more stable than the β - and ϵ -Co phases. However, the structural stability should be expressed as energy per unit cell volume (E_x/V_x , where x is Co-phase), the calculated $\Delta(E/V) \sim (E_\alpha/V_\alpha - E_x/V_x)$, where x is Co-phase) values show that the α -Co structure is the most stable (Table 4-I) which is in accordance with the experiments. Table 4-I presents lattice parameters achieved from both „ab initio calculations“ and experiments taken from literature and energy per atom and energy per unit cell volume and spin magnetic moments in magneton bohr (μ_B) unit for three phases.

Table 4-I. Lattice parameter (a), total energy per cobalt atom (E), energy per volume unit $\Delta E/V$, spin moment (σ) and Fermi energy (E_F).

	Phase	a^a (Å)	E (eV/Co _{atom})	$\Delta E/V^b$ (htr/Å ³)	σ (μ_B)	E_F (eV)
GGA	hcp (α)	1.620	37918.590	0.0000	1.6881	8.6849
	fcc (β)	3.498	37918.577	118.76	1.6915	9.3114
	ϵ (FM)	6.057	37918.223	3.9113	1.6140 [type I:1.5426 , type II:1.6616]	9.5216
Expt.	hcp (α)	1.633	–	–	1.72 ^c	–
	fcc (β)	3.545	–	–	1.75 ^d	–
	ϵ (FM)	6.097	–	–	1.70 ^e	–

^a Correspond to a cell parameter for fcc and epsilon phase and c/a for hcp phase.

^b $\Delta E/V=(E_{\alpha}/V_{\alpha}-E_{\beta}/V_{\beta})$, where x is the Co phase.

^c Reference 30.

^d Reference 31.

^e Reference 28.

The obtained spin density per atom (σ_{Co}) for the different phases- For the hcp and fcc phases the σ_{Co} values for all atoms are almost identical with values of $1.69\mu_B$. In the case of epsilon phase different σ_{Co} values are obtained as a function of the atom type. The eight atoms of *type I* exhibit a lower σ_{Co} value of $1.54\mu_B$ while for the twelve atoms of *type II* the atomic spin density is larger $1.66\mu_B$.

Graphs of DOS for α -, β -, and ϵ -Co phases are presented in (Figs. 4-4 to 4-9), respectively. In this diagrams TDOS is the total density of state and PDOS is partial density of states showing contribution of atom orbitals in the unit of states/Hartree/unit cell and energy is in unit of Hartree which equals to 27.2114 eV.

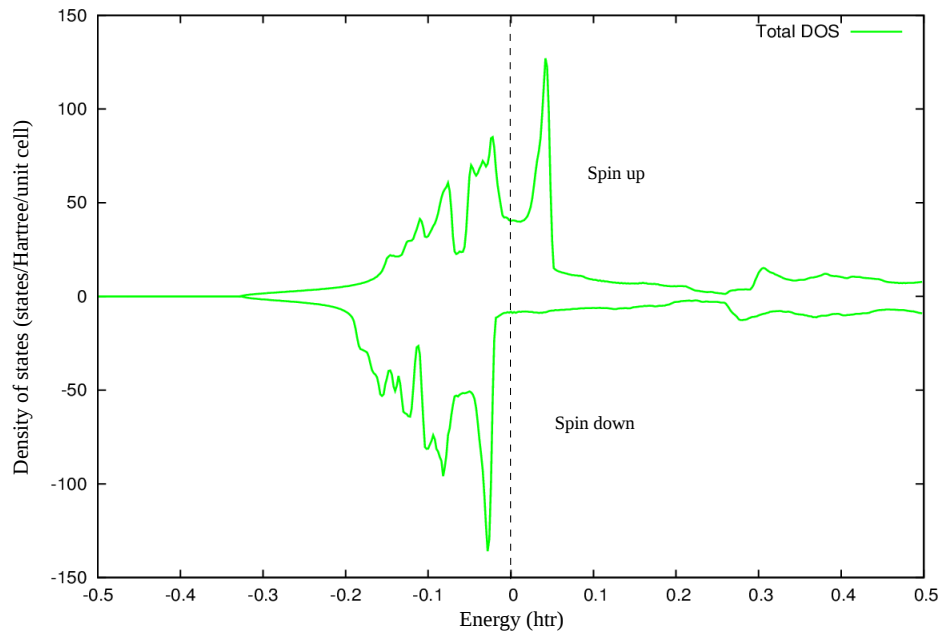


Figure 4-4. Total density of state for hcp or α -phase of cobalt.

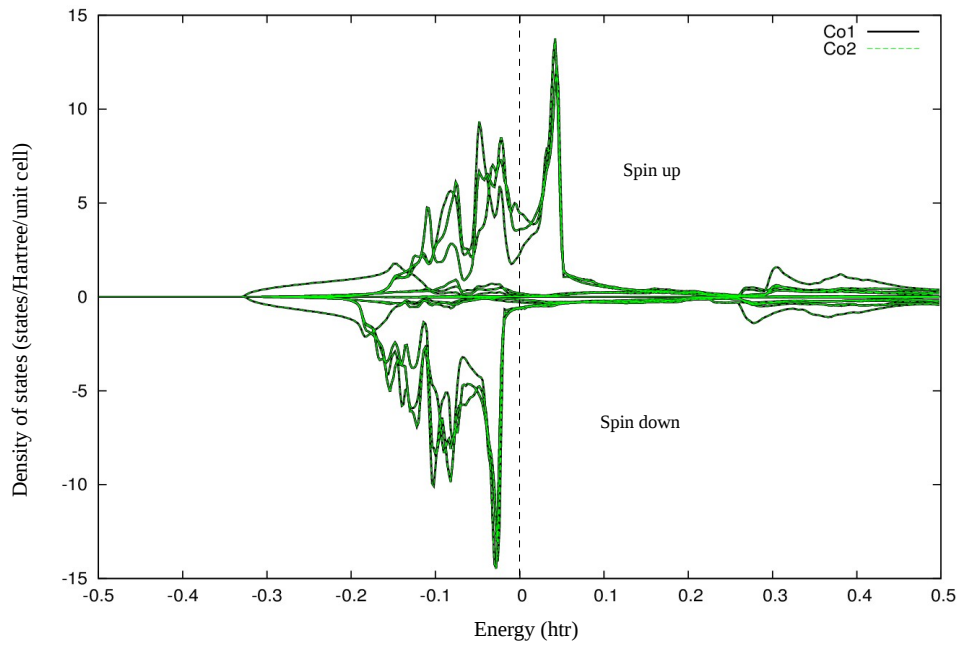


Figure 4-5. Partial density of state for cobalt atoms involving hcp or α -phase unit cell.

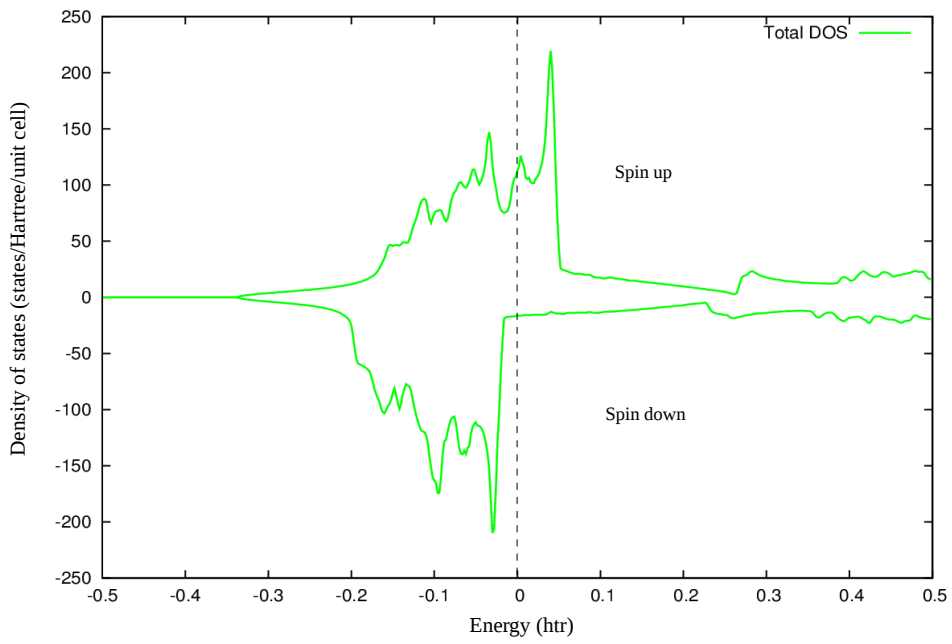


Figure 4-6. Total density of state for fcc or β -phase of cobalt.

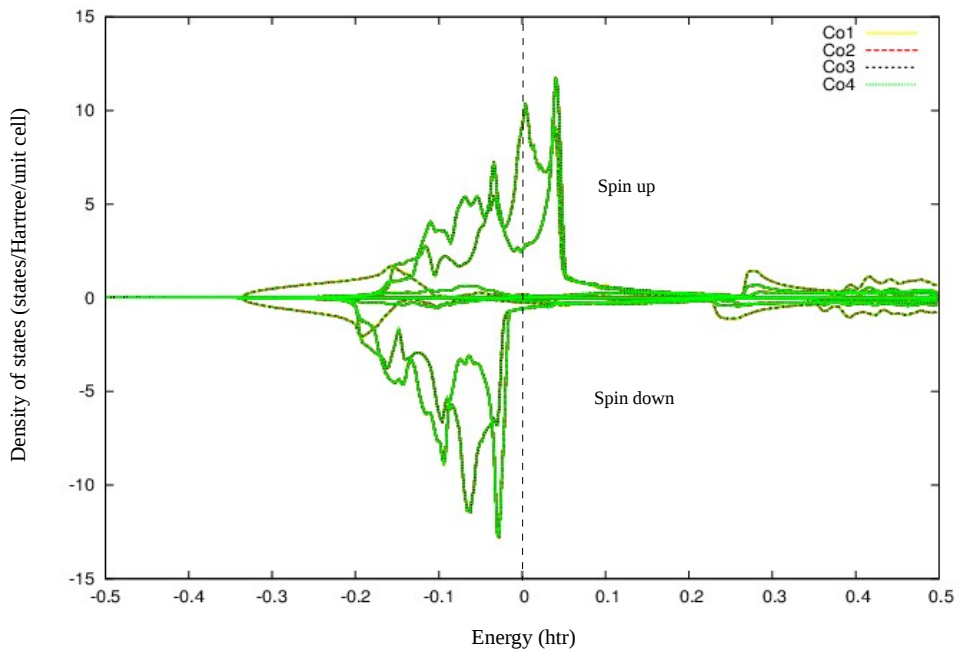


Figure 4-7. Partial density of state for cobalt atoms involving fcc or β -phase unit cell.

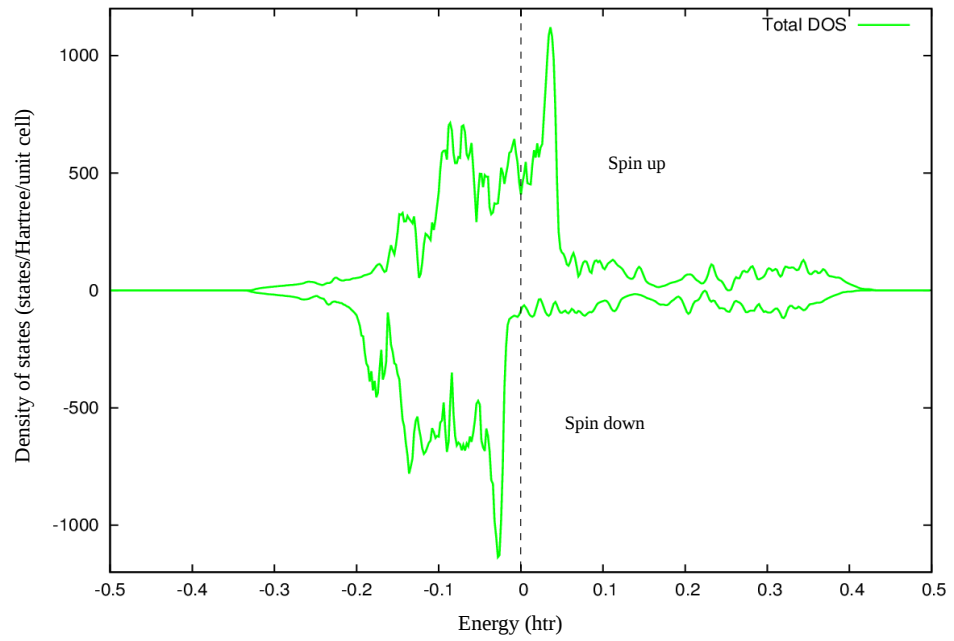


Figure 4-8. Total density of state for ϵ structure of cobalt.

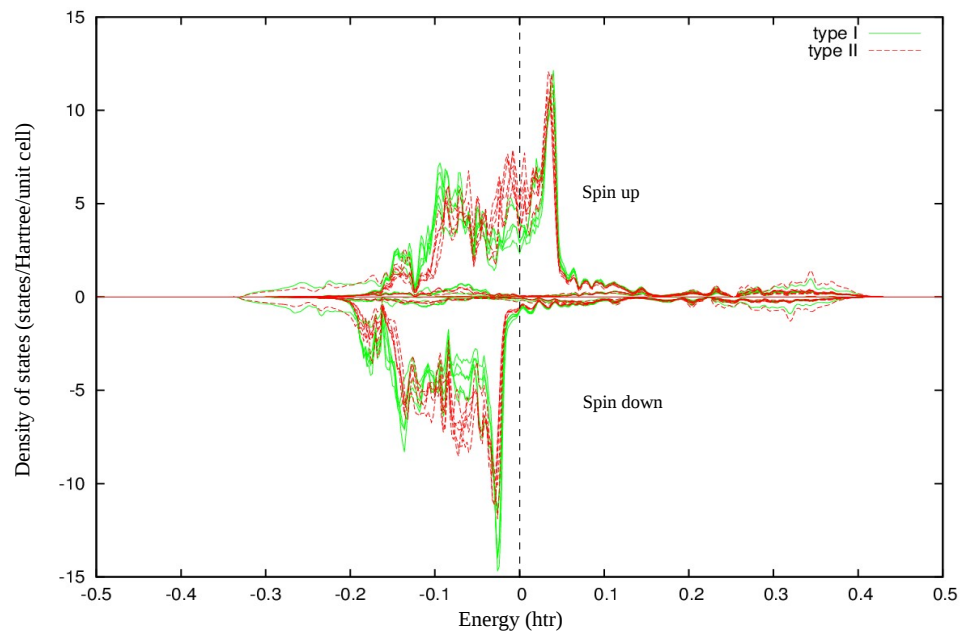


Figure 4-9. Partial density of state for type I and II Co atoms involving ϵ -phase unit cell.

Conclusion- from these figures for Density of states for Cobalt in three phases, it is concluded that cobalt is a half-metal because at Fermi level only one channel of electrons (spin up electrons) are present. And as it was expected Co in ϵ -phase shows the highest density of states due to the more atoms that are present in the unit cell, therefore it can be a good source for spintronics field.

4.3 Spinel Ferrites Compounds

The spinels with unit formula AB_2X_4 are one of the most interesting and important families of compounds, where A, B and X represent, a divalent cation, a trivalent cation and a divalent anion, respectively. Where one of the cation sites are occupied with iron they are named spinel ferrites. Majority of the spinel ferrites form cubic spinel structure belonging to space group $Fd\bar{3}m$. The cations A and B can occupy two different sites, i.e. octahedral (O_h) and tetrahedral (T_d) sites within the fcc X sublattices. In „normal spinel“ tetrahedral and octahedral sites are occupied by divalent and trivalent cations, respectively, while in „inverse spinel“ half of the trivalent cations occupy tetrahedral sites and a mixture of di- and trivalent cations are distributed on the octahedral sites. Depending upon the nature (magnetic or non-magnetic) and distribution of cations among A and B sublattices, spinel ferrites can exhibit different magnetic properties such as ferrimagnetic, antiferromagnetic and paramagnetic. The ferrimagnetic features are mediated by antiferromagnetic coupling between the magnetic moments at the A and B sites. The spinel ferrites are used widely in industry due to their magnetic and electronic properties such as high magnetostriction, cubic magnetocrystalline anisotropy, high coercivity, moderate saturation magnetization, high Curie temperature, high chemical stability and good electrical insulation, in particular the „spinel cobalt ferrite“, Fe_2CoO_4 , has a wide range of applications including electronic devices, ferrofluids, magnetic delivery microwave devices and high density information storage. Fig. 4-10 presents cubic spinel structure.

In this thesis, density of states, stability and magnetic properties of Co_2FeO_4 and Fe_2CoO_4 spinel ferrites are studied. The experimental work on these compounds are very limited. The probable reason for Co_2FeO_4 could be the spinel phase stability over a small temperature range about 900°C.

Crystal field splittings and expected occupation of the 3d electrons of Co and Fe in their divalent and trivalent oxidation states are shown in Fig. 4-11. In the tetrahedral crystal field, the doubly-degenerate e_g states are lowered in energy with respect to the t_{2g} triplet states due to the electrostatic repulsion of the d_{zy} , d_{yz} and d_{xz} orbitals, while in the octahedral site it is vice versa, the d_z^2 and $d_{x^2-y^2}$ orbitals are repelled and possess higher energy. Experimental measurements of the magnetic moments confirm the fact that Co tends towards low spin configurations, while Fe favors high spin ones. [1, 32, 33]

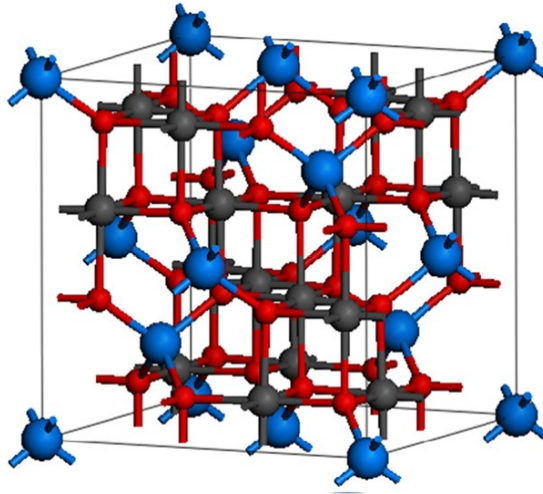


Figure 4-10. Illustration of the cubic AB_2O_4 spinel structure. The A atoms colored blue occupy tetrahedral sites and the B atoms colored dark gray occupy octahedral sites within a fcc oxygen sublattice colored red [1].

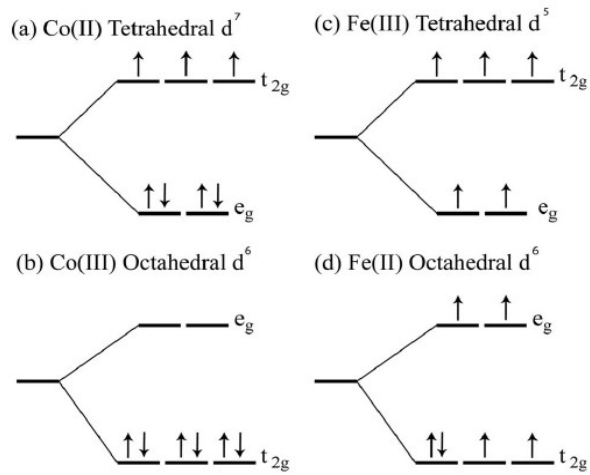


Figure 4-11. Schematic crystal field splitting and occupations of the Co and Fe 3d electrons in tetrahedral and octahedral sites [33].

4.3.1 DOS Calculation for Fe₂CoO₄ and Co₂FeO₄

It is noted for these calculations the „Elk“ -program was not able to produce the reliable results due to the failure in band gap estimations, hence „Quantum Espresso“ [34] is used which is an integrated suite of computer codes for electronic structure calculations and materials modeling, although it is also a DFT-based program, the applied pseudopotentials which presume not the effect of the bare nuclei, but rather the potentials screened by the core electrons, makes it proper to do these calculations. These potentials are more flattened than the “true” one. The acronym ESPRESSO stands for *opEn Source Package for Research in Electronic Structure, Simulation, and Optimization*.

Calculation Method- it was started with the experimentally determined lattice constants, ultrasoft pseudopotentials are used and the exchange-correlation effects were treated by the generalized gradient approximation (GGA).

DFT band gap error- the DFT resulted band gap is underestimated, as the valence band maxima (VBM) lies too high and the conduction band minimum (CBM) lies too low with respect to vacuum conditions. Mainly the reason for this deficiency is the self-interaction contained in the LDA and GGA exchange–correlation potentials. There are variant ways to correct the band gap errors. One is to use a non-multiplicative potential, for example „Hybrid functionals“ by replacing a fraction of exact exchange potential with the LDA or GGA exchange, improve the band gap. However, in the most cases the hybrid methods are not appropriate. Another possibility is the LDA+U method, where U is the „Hubbard term“ but it can only be applied to correlated and localized electrons, such as 3d or 4f electrons in transition and rare-earth oxides. In this thesis the second method is applied to resolve the band gap problem. By adding the Hubbard parameter, “U_{eff}” to the transition metal d-orbital the position of VBM is corrected to a large extent. U_{eff} is the difference between parameters U and J. The Hubbard U is the amount of energy which should be supplied to conquer the Coulomb-energy to place two electrons at the same site, and J is an approximation to the Stoner exchange parameter (for more details refer to [35]). In contrast to the Local Spin Density Approximation (LSDA) which produces the metallic solution for these spinels, the LSDA+U shows an insulating behavior for Fe₂CoO₄. The calculated value of U_{eff} depends on the theoretical approximations and for this work it is sufficient to regard the value of U_{eff} as a parameter and try to ascertain its value from comparison of the calculated physical properties with experiments.

In the LDA+U method the double-counted Coulomb energies should be corrected. This means the Hubbard Hamiltonian can not be simply added to the LDA, but those contributions that have already been taken into account in the LDA must be subtracted in a mean-field way. There are three different approximations to define such a mean-field corrected Hubbard Hamiltonian in the literature; namely the “around mean field” (AMF) correction, the “fully localized limit” (FLL), and the interpolation scheme between these two cases. [1,36,37,38,39,40]

For the Fe_2CoO_4 and Co_2FeO_4 spinel ferrites also DFT-based calculations failed to describe insulating and magnetic properties. To improve the results DFT+U method is used and the theoretical information available in literature [33] is taken into account as reference for starting magnetic moments (Table 4-II). And from these references it was known Fe_2CoO_4 is an insulator but no information was available for Co_2FeO_4 . By applying Hubbard U parameter the correct band gaps are attained. The results show an insulating behavior for Fe_2CoO_4 and a half-metallic for Co_2FeO_4 which is also confirmed by our experimentalists. The total Density Of States (DOS) are calculated for both Normal- (N) and Inverse- (I) structures. The graphs of them are presented in Figs. 4-14 to -20). The calculated magnetic moments are presented in Table 4-III.

Table 4-II. Magnetic moments (μ_B) for Co and Fe taken as reference [33]

Material	Co^{tet}	Co^{oct}	Fe^{tet}	Fe^{oct}
Fe_2CoO_4 (N)	2.45			-4.06
Fe_2CoO_4 (I)		0.13	3.51	-4.05
Co_2FeO_4 (N)		-0.22	3.78	
Co_2FeO_4 (I)	2.47	0.09		-4.05

The calculated total energies (Table 4-IV) show that Co_2FeO_4 in inverse structure possesses the lowest energy. However, the structural stability should be expressed as energy per unit cell volume (E_x/V_x). The calculated energies per unit cell volume by considering the Co_2FeO_4 -inverse structure total energy as reference (Table 4-IV) show that the Co_2FeO_4 in normal structure is unstable but the others are stable. Fig. 4-12 presents the phase diagram of Co-Fe-O taken from [41,42,43], in this diagram the red dots indicate the stable phases and purple dot, the Co_2FeO_4 as unstable phase confirming the results obtained from the calculations done for this thesis. Fig. 4-13 shows the total energy of compounds with respect to Co_2FeO_4 -inverse total energy taken as reference versus absolute magnetization.

Table 4-III. Calculated magnetic moments (μ_B) for Co and Fe

Material	Co^{tet}	Co^{oct}	Fe^{tet}	Fe^{oct}
Fe_2CoO_4 (N)	1.68			-3.87
Fe_2CoO_4 (I)		2.74	3.02	-3.50
Co_2FeO_4 (N)		-2.35	2.47	
Co_2FeO_4 (I)	3.49	-2.50		-2.50

Table 4-IV. Calculated absolute magnetic moments, total energy and energy per unit cell volume ($\Delta E/V$)

<i>Material</i>	<i>total energy (eV)</i>	<i>absolute magnetic moment (μ_B/unit cell)</i>	$\Delta E/V^a$ (eV/Å ³)
<i>Fe₂CoO₄ (N)</i>	-8506.8	20.28	5.7642
<i>Fe₂CoO₄ (I)</i>	-8512.2	18.45	0.3816
<i>Co₂FeO₄ (N)</i>	-8967.8	16.02	-0.0034
<i>Co₂FeO₄ (I)</i>	-8992.3	17.52	0.0000

^a $\Delta E/V = (E_{\text{CoFeO-i}}/V_{\text{CoFeO-i}} - E_x/V_x)$, where x is the spinel compound

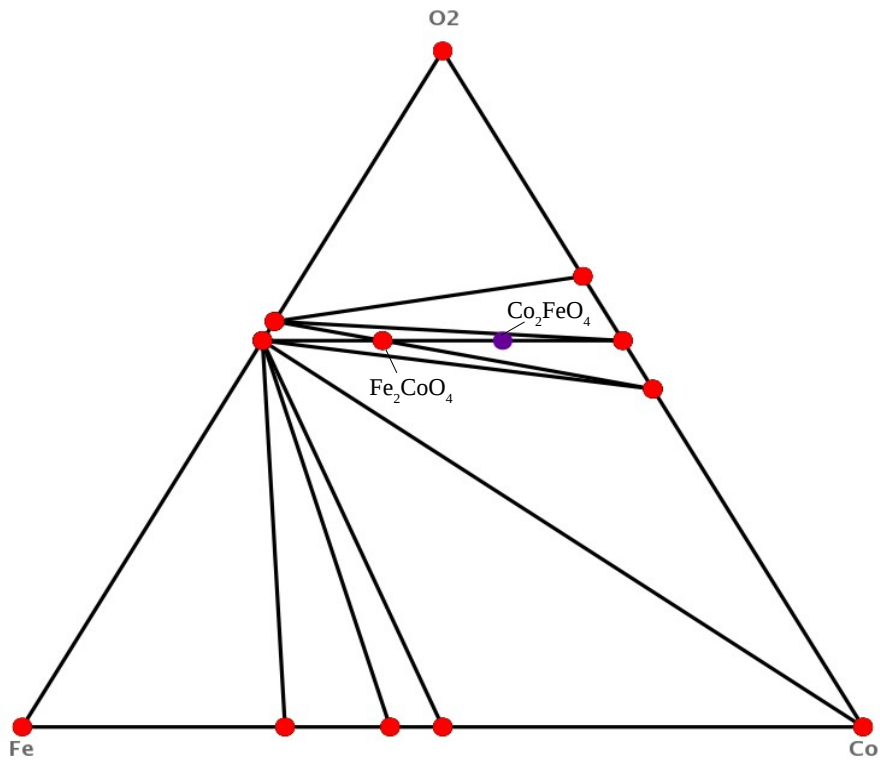


Figure 4-12. (Color online) Co-Fe-O phase diagram, red dots show the stable phases and purple dot the unstable Co_2FeO_4 one.

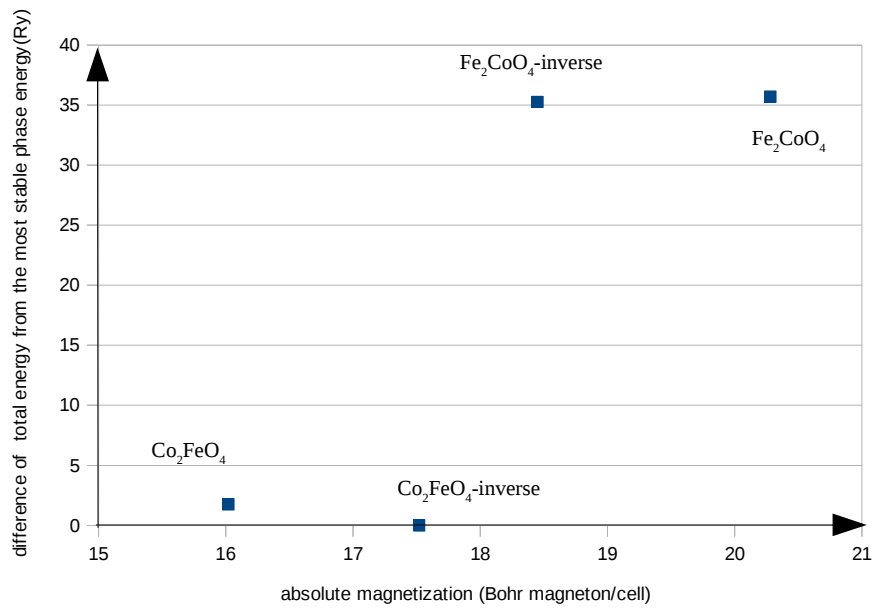


Figure 4-13. Difference of either total energy from the total energy of the most stable phase Co_2FeO_4 -inverse vs. the absolute magnetization in (μ_B /unit cell).

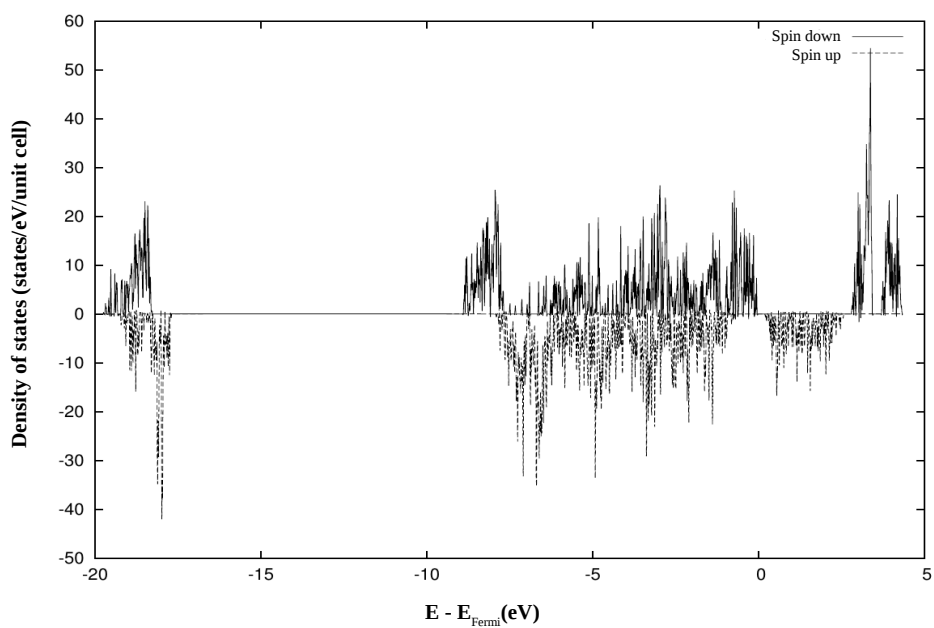


Figure 4-14. Density of states for Fe₂CoO₄ normal spinel vs. energy (eV) for spin up and down electrons.

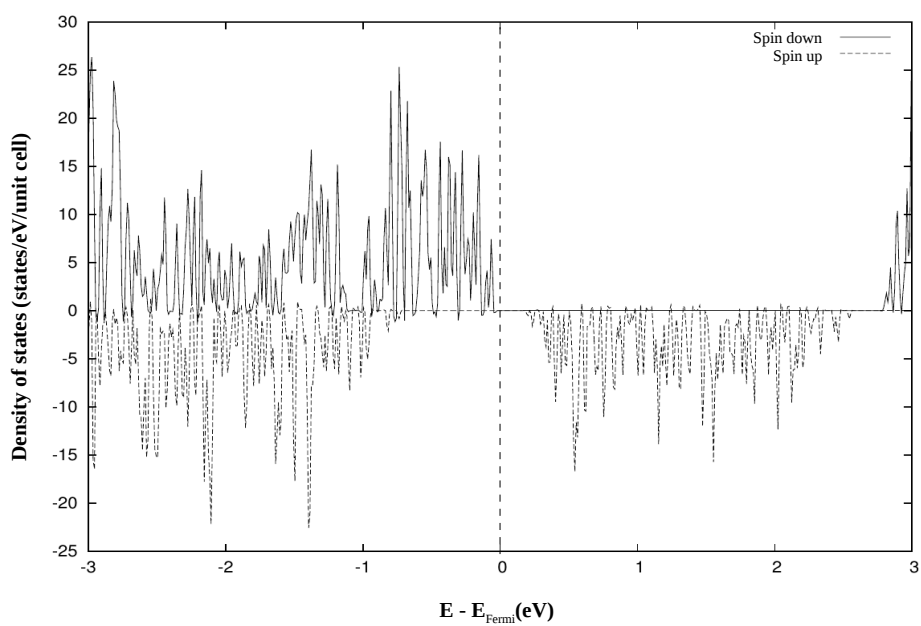


Figure 4-15. Density of states for Fe₂CoO₄ normal spinel vs. energy (eV) for spin up and down electrons close to the Fermi level.

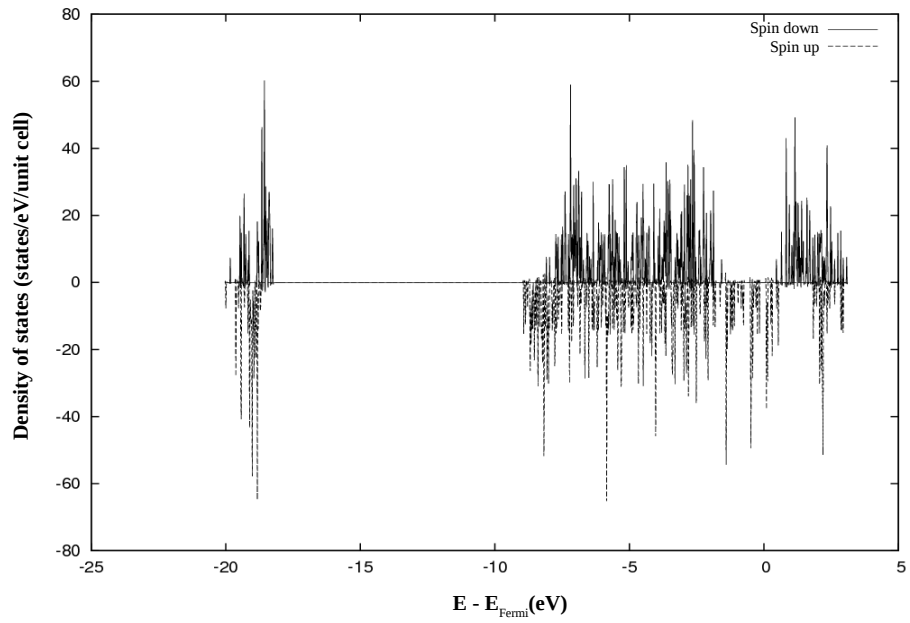


Figure 4-16. Density of states for Fe₂CoO₄ inverse spinel vs. energy (eV) for spin up and down electrons.

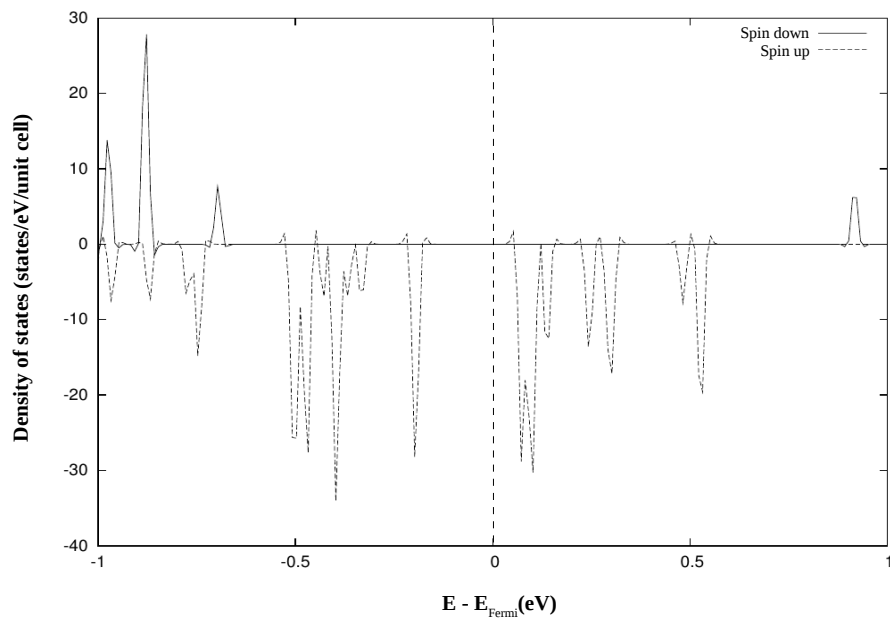


Figure 4-17. Density of states for Fe₂CoO₄ inverse spinel vs. energy (eV) for spin up and down electrons close to the Fermi level.

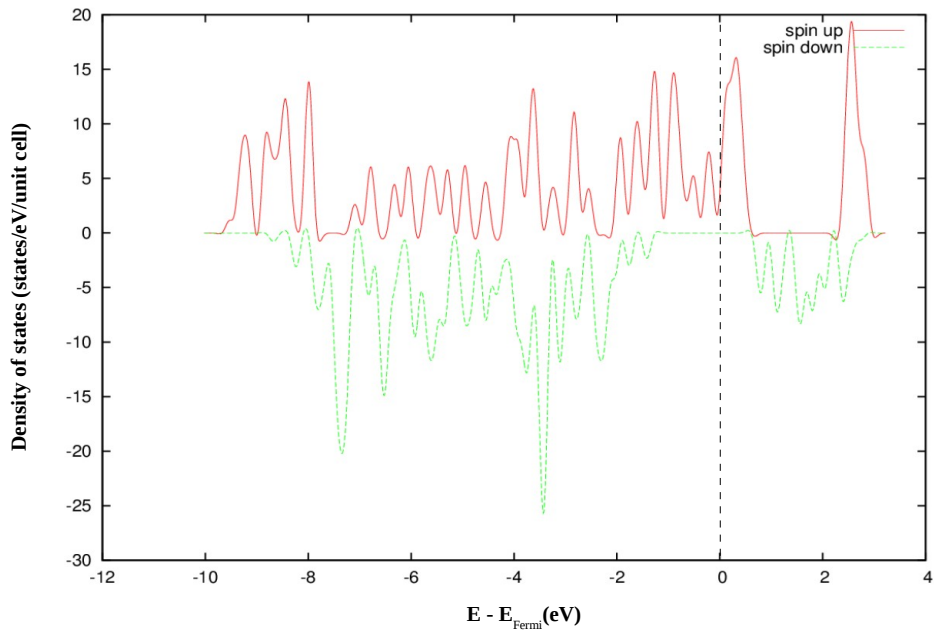


Figure 4-18. Density of states for Co₂FeO₄ normal spinel vs. energy (eV) for spin up and down electrons.

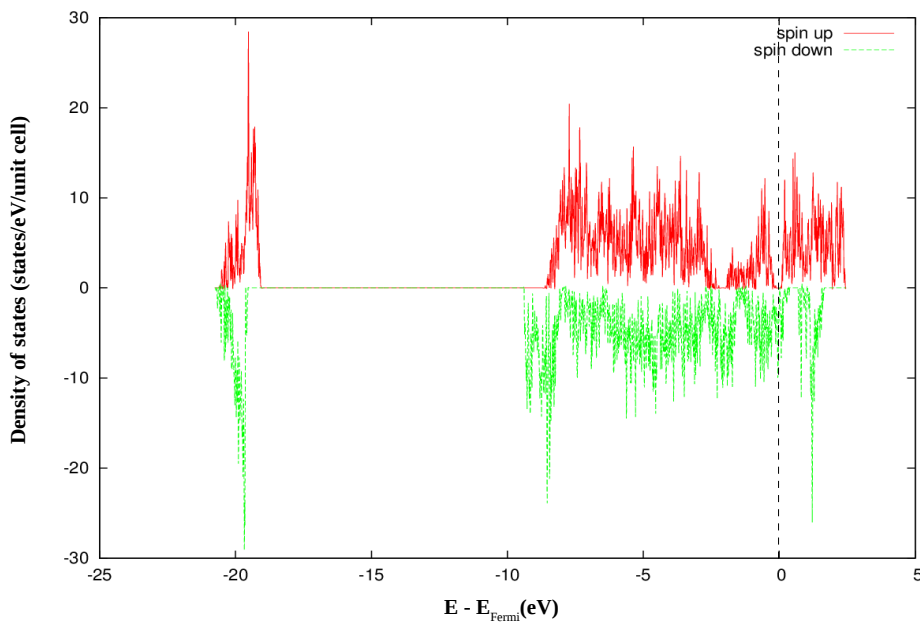


Figure 4-19. Density of states of Co₂FeO₄ inverse spinel vs. energy (eV) for spin up and down electrons.

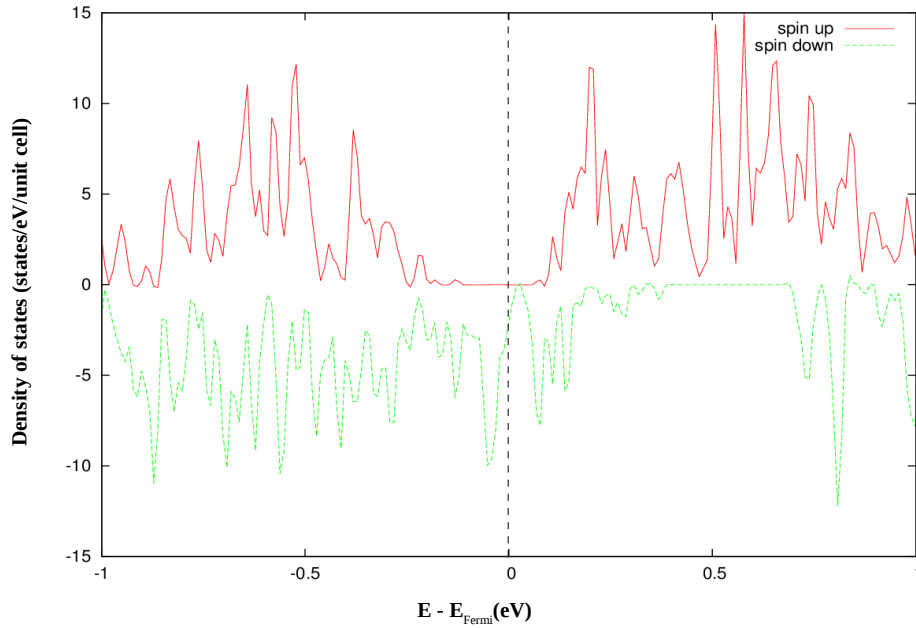


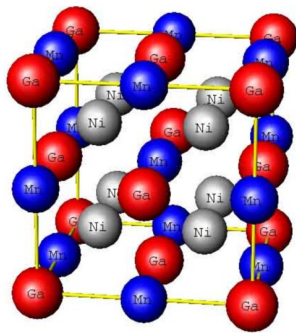
Figure 4-20. Density of states for Co_2FeO_4 inverse spinel vs. energy (eV) for spin up and down electrons close to Fermi level.

Conclusion- According to these results Fe_2CoO_4 in both structures is an insulator with a gap about 0.21 eV for Normal structure which is in a good agreement with [4] and 0.24 eV for Inverse one which does not correspond to [4] with a gap of 0.8 eV, while Co_2FeO_4 is a half-metal which corresponds to the experiments of Anna-Lena Wolff. As the data in Table 4-III shows the calculated magnetic moments in comparison to Table 4-II, taken magnetic moments as reference, the magnetic moments for Co are overestimated as a result of what is discussed in section 2.6. From Fig. 4-13 it seems that the higher the absolute magnetic moment is, the less stable is the compound. Fig. 4-12 shows the phase diagram of Co-Fe-O taken from [41,42,43], in this diagram red dots indicate the stable phases and purple dot, the Co_2FeO_4 as unstable phase, according to this diagram the total energy of Co_2FeO_4 is less than the Fe_2CoO_4 which is in a good agreement with the data resulted from the calculations done for this thesis (Table 4-IV). According to these calculations, as indicated in Fig. 4-13, Co_2FeO_4 in inverse structure possesses the lowest total energy, hence it is taken as reference structure to calculate energy per unit cell volume ($\Delta E/V$) to investigate the stability of these compounds. The results are presented in Table 4-IV. Generally compounds in an 'Inverse structure' do have lower total energy than the 'Normal structure'. The stability investigation on these compounds reveals that the Fe_2CoO_4 is in both structures stable while the Co_2FeO_4 is only in Inverse structure stable. As a result Co_2FeO_4 is a metastable phase.

5 Heusler Alloys and Shape Memory Effect

This family of compounds were discovered by Heusler in the 1903 and their remarkable property is to be ferromagnetic, although the elements comprising are not ferromagnetic such as Cu_2MnAl . In section 5.4 the total magnetic moments of this family will be more discussed as „Slater-Pauling rule“. The Heusler alloys with general formula X_2YZ , where X is 3d-metal, Y is usually Mn but could be other 3d-metal or rare-earth elements, Z is one of the elements from groups III or IV of the periodic table crystallize in the L2_1 structure (space group Fm-3m) comprising four interfering fcc sublattices (Fig. 5-1). Different metallic elements with a variety of compositions occupy this structure to generate stoichiometric or nonstoichiometric compounds. Heusler alloys due to the presence of the so-called p elements (Ga, Al, Ge, etc.) which form partially filled bands close to Fermi level favoring to hybridize with the d electrons of transition metals. In the case of Ni_2MnGa , the Ga atoms hybridize with Ni atoms. This hybridization gives a peak for the spin-down electrons in the total electronic density of states right at the Fermi level which can be spontaneously split and induced a phase transition due to the Jahn-Teller effect described in detail in section 5.3.

Figure 5-1. L2_1 structure also called Heusler structure belongs to Fm-3m Space Group presenting Ni_2MnGa compound [44].



On the other hand, Heusler alloys like Cu_2NiAl and Zn_2CuAu are characterized by thermoelastic martensitic transformations presenting strains up to 20%. The transformation is caused either by inducing a structural martensitic transition – a diffusionless first-order solid-solid phase transformation from the high-

temperature austenite to low-temperature martensite phase obtained by the small cooperative movement of the atoms, the L2_1 cubic structure is distorted by a contraction of the c axis to a low symmetry body-centered-tetragonal structure represented by the tetragonality parameter c/a – or by rearranging twin boundaries between domains. The shape memory effect in Heusler alloys is the capability to remember their original shape when they are deformed to the martensitic state by lowering the temperature and then heated to transform to the austenitic state. While the shape memory effect in most of the current commercial actuators is caused by a martensitic phase transformation driven by temperature or applied stress, the magnetic control of such transformations would be faster and more efficient.

The Ferromagnetic Shape Memory Effect was first discovered in Ni_2MnGa ferromagnetic „Heusler alloy“ by O’Handley and collaborators at MIT in 1996. O’Handley et al. were able to induce reversible deformations of 0.2% by application of magnetic fields below 1T. Since then, the study of ferromagnetic shape memory Heusler alloys attracts the interests to explore physics behind this phenomenon and to discover the technologically interesting possibilities for applications. Only a few years after discovery this effect, giant deformations of about 10% were obtained in nonstoichiometric Heusler alloys. [45,46,47,48,49,50]

5.1 Structural Properties of Magnetic Heusler Alloys

The crystal structure of the austenitic parent phase for stoichiometric compound has been determined by neutron diffraction to be cubic with $L2_1$ structure Fig. 5-1. The magnetism is due to 3d electrons of X and Y elements. Depending on martensitic transformation temperature (T_M) the alloy shows different structures. If the alloy transforms at $T < T_M$ usually shows a modulated structure constructed from nanotwinned variants of a tetragonal $L1_0$ phase [Fig. 5-2 (d)] and for $T > T_M$ a nonmodulated structure involving a body center tetragonal (bct) $L1_0$ unit cell is known. For Ni-Mn-Z (where $Z = \text{Ga, In, Sn, Sb, ...}$) alloys, there is a range of composition that during cooling the system first becomes ferromagnetic, and at a lower temperature undergoes the martensitic transition with different magnetic behaviors such as ferro-, para- and non-magnetism. For Ni-Mn-Ga, the range of compositions is very broad and extends from the Mn-poor to the Mn-rich alloys. Ni_2MnGa is so far the only stoichiometric Heusler alloy known that shows a martensitic transition in the ferromagnetic state. [46, 49, 51, 52]

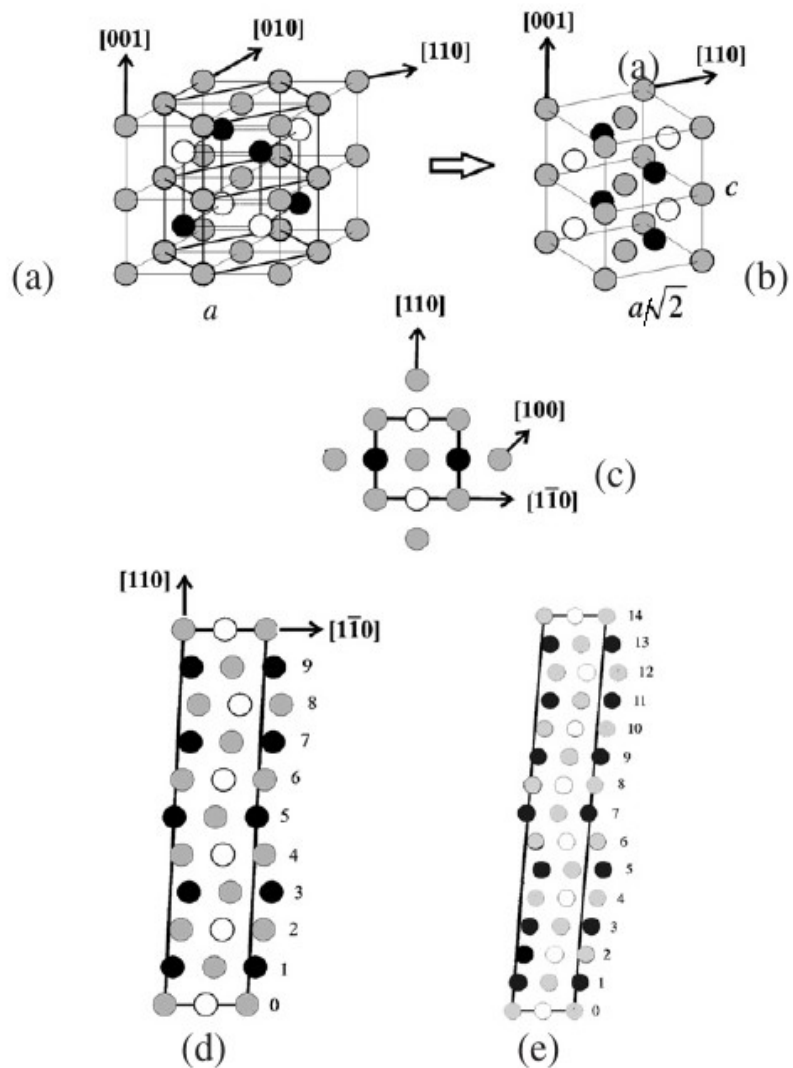


Figure 5-2. Austenite and martensite structures of Heusler alloys shown for the case of Ni_2MnGa . Light grey: Ni, white: Mn, black: Ga. (a) The $L2_1$ Heusler structure showing also the relationship with the tetragonal unit cell which is also shown in part (b). (c) The tetragonal unit cell viewed from the top and (d) the 5M (or 10M) and (e) 7M (or 14M) modulated structures obtained by shearing the tetragonal cell [53].

5.1.1 Martensite Structures

The ferromagnetic shape memory effect takes place only in phases with a modulated structure, where a giant strains of several percent by applying fields due to rearrangement in twinned microstructures are observed.

These modulated phases form by a displacive transition from a high-symmetry austenite to a low-symmetry martensite phase is not stable thermodynamically which is proved by calculations done for this thesis for Ni₂MnGa in next chapter. As presented in Fig. 5-3(a), there are three equivalent ways to transform the cubic unit cell to a tetragonal one. This results in three possible alignments of the tetragonal c_{NM} -axis with respect to the original austenite cube axes a_A . In the absence of external fields or loads, none of the three possible orientations of the tetragonal martensite unit cell is favoured. A uniform distribution is realized by martensite variants with different orientation where one variant consists of neighbouring unit cells with identical orientation (Fig. 5-4). A magnetic field applied in y direction rotates the magnetic moment of the x -variant, thus deforms it due to magnetostriction, while leaving the y -variant undeformed and its magnetic moment unrotated. According to microscopic analysis of Ni–Mn–Ga alloys [54,55], the ends of twin boundaries can be pinned at the cores of twinning dislocations situated at the dislocation walls and the distance between the pinning centers may be of the order of 0.5 μm or even more. The dimensions of cores are of the order of the lattice parameter, and therefore, according to the Wechsler –Liberman – Read theory [56], the estimated lattice misfit induced by magnetostriction is sufficient for the rearrangement of twinning dislocations and the initiation of a detwinning process. The distance traveled by the twin boundary should be dependent not only on the applied stress, but also on the spatial distribution and the strength of the pinning centers- A and B points in Fig. 5-4. In martensitic transformation a habit plane [Fig.5-3(b)] is considered as a lattice invariant interface connecting the two crystal structures. The martensitic structure compensates the lattice mismatch between two crystals by twinning the structure [Fig. 5-3(b)]. By assuming this structure continues to microstructure scale, Khachatryan et al. argue that the modulated structures observed in materials with lattice instabilities could be understood as ultrafinely twinned metastable structures and not as thermodynamically stable phases. In this view, the large and complex unit cell of the modulated phase is composed of nanotwin layers of a thermodynamically simpler stable martensitic phase. The twinning periodicity and hence the modulation is determined by geometrical constraints and the transformation path. A very low nanotwin boundary energy requirement to convert one unstable modulated structure to a simple stable unit cell could be the proof for this explanation. Based on this concept the 14M Ni-Mn-Ga modulated lattice is built from unit cells of thermodynamically stable non-modulated (NM) phase.

The periodic twinning of the tetragonal martensite lattice is expressed through the fraction of the twin layers widths d_1 and d_2 [Fig. 5-3(b)]; $d_1/d_2=(a_{NM}-a_A)/(a_A-c_{NM})$. Here, a_{NM} and c_{NM} represent the lattice constants of the tetragonal martensite and a_A the lattice constant of the cubic austenite.

Figure 5-3. (a) The unit cell of cubic austenite can transform into three equivalent orientations of a tetragonal martensite unit cell. (b) Sketch of the orientation relationship between parent austenite and nanotwinned (adaptive) martensite phase. The different blue background colours mark differently oriented tetragonal martensitic variants which are connected by twin boundaries. The grey plane marks the habit plane. It is drawn with finite thickness to illustrate that it is accompanied by a distortion of the lattice [57].

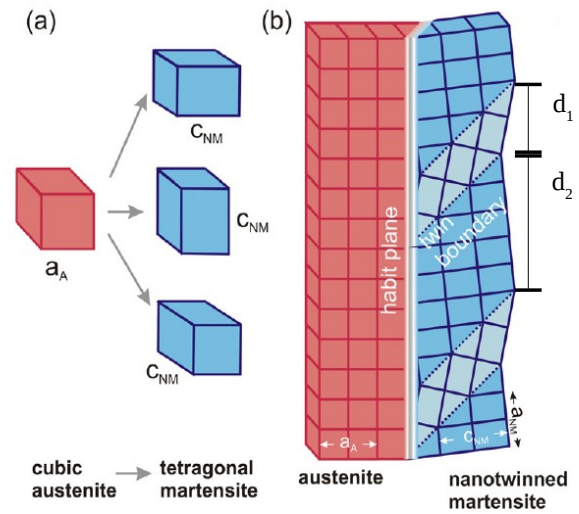
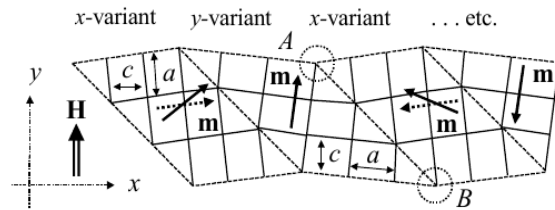
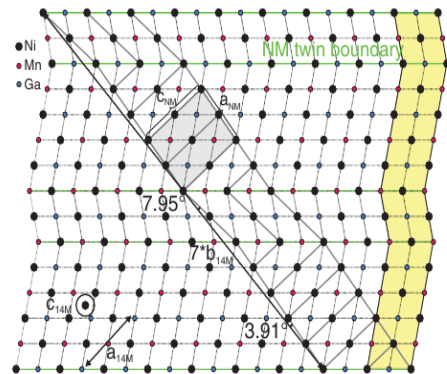


Figure 5-4. Schematic representation of two-twin-variants configuration in a tetragonal ferromagnetic martensite [58].



the nanotwinned modulated structure can be related to nonmodulated (NM) phase by branching. Hence the 14M unit cell can be constructed based on NM unit cells as building blocks (Fig. 5-5). As it will be shown in the following by using the NM lattice constants and the $(5\bar{2})_2$ twinning periodicity one can calculate the lattice constants of the adaptive 14M phase as well as the angles between crystal axes of the tetragonal NM twin variants and the axes of the adaptive 14M unit cell (as sketched in Fig. 5-5).

Figure 5-5. 14M structure constructed by periodic $(5\bar{2})_2$ twinning of tetragonal NM building blocks. One of the NM cells is exemplarily marked in grey. The green lines mark the nanotwin boundaries connecting NM cells. The directions of the three different 14M lattice parameters are sketched with brown color. The angles of the NM unit cells subtended with the 14M supercell (thick lines) are given. The conventional 14M unit cell within the bct reference system is marked in yellow [59].



As the calculations done for this thesis presenting in next chapter show that the modulated structure has higher energy than the NM martensite. By considering the concept of adaptive martensite, the energy difference can be interpreted as twin boundary energy γ of the NM phase.

In Ni-Mn-Ga Heusler alloys by increasing the electron density (e/a) these phase order is commonly observed; austenite, 6M (premartensitic), 10M (5-layer), 14M (7-layer) and NM (nonmodulated) martensite. The tetragonality of the NM martensites increases with the electron density, from $c/a_{NM} = 1.0152$ for 6M to 1.16 for 10M and 1.26 for 14M.

If the 10M- and 14M-type structures own the same stacking unit composed of the distorted $L2_1$ phase [denoted as a face-centered tetragonal (fct) structure in Fig. 5-7], the lattice parameters for the 10M and 14M structures can be evaluated on the basis of the fct structure as follows: $a_{2M} = c_{2M} = (\sqrt{a_{fct}^2 + c_{fct}^2})/2$ and $b_{2M} = a_{fct}$. The monoclinic angle β of the stacking structures can be evaluated as $\tan(\beta - 90^\circ) = A \tan(\beta_0 - 90^\circ)$, where $A [\equiv (n - m) / (n + m)]$ is a parameter indicating the extent of deviation from 90° in the angle β , and β_0 is the monoclinic angle of the 2M structure. For the 2M, 10M, and 14M structures this parameter is $A_{2M} = 1$, $A_{10M} = 0.2$, and $A_{14M} = 0.43$, respectively. By taking into account the 2M and fct structures (Fig. 5-7), lattice parameters for 10M and 14M structures in 2M parameters can be written as follows: $a_{10M} = a_{14M} = a_{2M}$, $b_{10M} = b_{14M} = b_{2M}$, $c_{10M} = 5c_{2M} (\sin \beta_0 / \sin \beta_{10M})$, and $c_{14M} = 7c_{2M} (\sin \beta_0 / \sin \beta_{14M})$. [52,56,57,58,59,60]

Fig.5-6 taken from [58] compares the lattice constants for three phases.

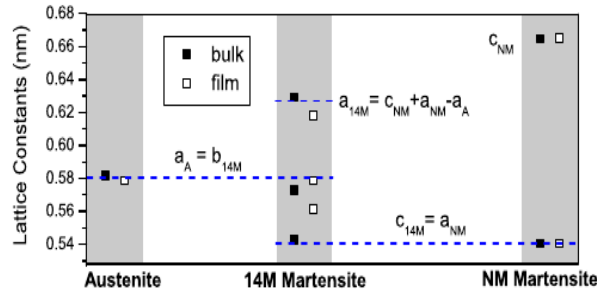


Figure 5-6. Comparison of lattice constants for the three different phases. The blue dashed lines mark the calculated lattice constants of the adaptive martensite phase. For each phase, film, and bulk [51] lattice constants are shown [59].

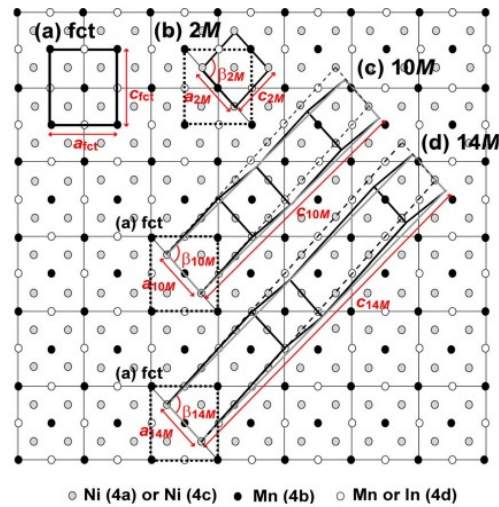


Figure 5-7. Projections of the face-centered tetragonal (a), 2M (b), 10M (c), and 14M (d) structures on b axis [52].

5.1.2 Construction of the layered Structures

A face centred tetragonal (fct) with $L1_0$ lattice is most often supposed as the basic martensitic structure (NM) [Fig. 5-8(a)]. The martensitic modulated structures are commonly constructed as long period stackings of close-packed planes derived either from the $\{110\}$ planes of austenite or from the $\{111\}$ planes of the NM unit cell ($L1_0$). The modulated unit cell is described as a monoclinic lattice with a -, b - and c -axis, respectively aligned along the $[\bar{1}10]$, $[001]$ and $[110]$ planes of the cubic austenite. The stacking sequences of the 14 M and 10 M structures are $(5\bar{2})_2$ and $(3\bar{2})_2$ in Zhdanov notation, respectively. The basal planes, $\{001\}$, are stacked along the c -axis in such a way that two consecutive planes are shifted along the a -axis a distance given by $(1/3+\delta)a$, where δ is an adjustable parameter ($\delta=0$ presents a perfect close-packed structure) [51].

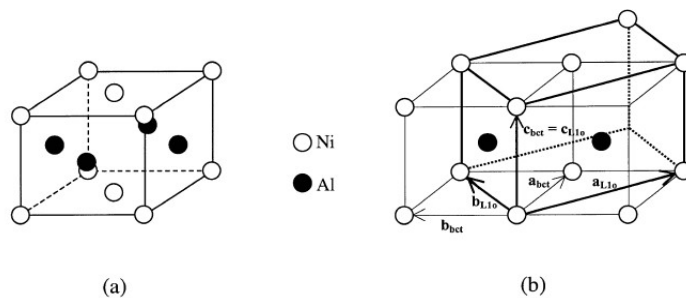


Figure 5-8. (a) Scheme of the $L1_0$ unit cell (b) relations between the „cubic“- and „ $L1_0$ “- structure axes [51].

Zhdanov notation of distorted stacking sequences in close packed crystals- The Zhdanov notation is a helpful notation to symbolize close packed or layered structures with ordered or disordered sequences of stacking. The long period martensitic structures are frequently designated by this compact schematic representation. The periodic shuffling can be noted as a zig-zag sequence of layers : a series of numbers indicate the atomic layers related to a periodical shift corresponding to a fundamental lattice vector, the opposite shift direction of the next stacking of planes is indicated by a minus sign over the number of layers. The suffix means the total number of zig-zag motifs constituting the periodic crystal lattice. In Fig. 5-9 some examples of this notation are illustrated [50].

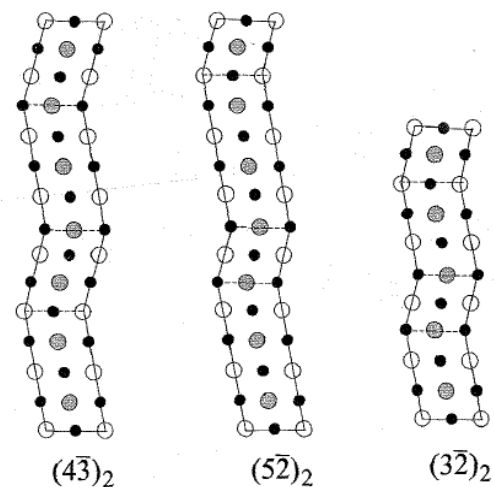


Figure 5-9. Three examples of Zhdanov sequences of martensitic layered structures. The two structures on the left are referred to the 7M modulation and the right structure relates to the 5M modulation. The Zhdanov symbol for each model is displayed under the structures [50].

5.2 Magnetic field effect on Strain

It is known that by applying a magnetic field orthogonal to the magnetization of a single variant large thermoelastic strains are achieved in Ferromagnetic Shape Memory Alloys (FSMA). The field-induced strain is induced by twin boundary motion due to the reorientation of the tetragonal martensite variants. The required driving force for this reorientation is provided by the difference in the Zeeman energy $E_{\text{Zeeman}} = \Delta M \cdot H$ of neighboring variants with different crystallographic anisotropy. In a martensitic transformation, e_0 , the transformation strain, characterizing the crystallographic distortion, depends on the tetragonality c/a of the martensitic phase and is described as

$$e_0 = 1 - c/a \quad (5.1)$$

Besides, the shear strain across the twin boundary is given by

$$\varepsilon_0 = (a/2c)(1 - c^2/a^2) \quad (5.2)$$

Fig. 5-10 shows the field-induced-strain measured in martensitic phase of Ni_2MnGa at 265 K. Fig. 5-11 illustrates how the crystal is bent under applied magnetic field. This change in magnetization direction provides the mechanism for field-induced motion of the atoms constituting twin-boundary motion. [46,61]

Figure 5-10. Strain vs applied field at 265K in the martensitic phase of Ni_2MnGa . Inset, relative orientation of sample, strain direction [110], and applied field [001] for field-induced strain measurements [61].

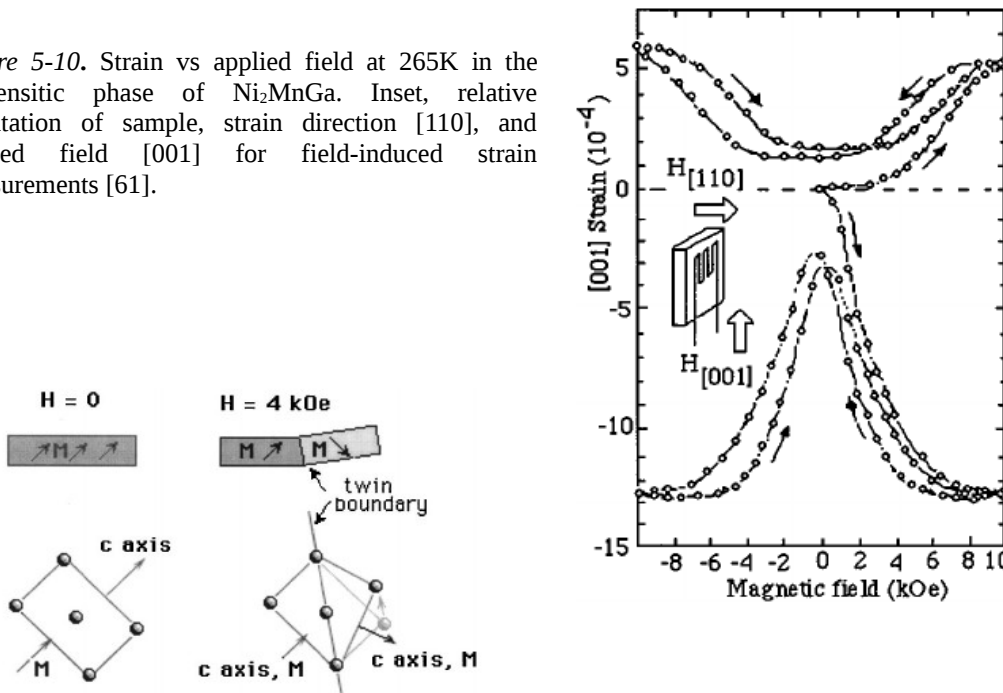


Figure 5-11. (top) schemes of magnetization directions in the sample. (below-left) the orientation of the martensitic unit cell, (below-right) the twinned martensitic cell [61].

5.3 Jahn-Teller effect

One hypothesis for explanation the occurrence of spontaneous phase transition in Heusler alloys is Jahn-Teller theorem. The theorem was originally formulated by Jahn-Teller (1937) to describe the instability of symmetric molecules in the presence of degenerate electronic orbitals. The effect is a phase transition driven by the interaction between the electronic states of one of the constituents of material with the collective lattice vibrations or phonons. This phase transition may be of first or second order and in both these cases involves a symmetry-lowering of the lattice by distortion the lattice and as a result splitting the electronic energy levels. In other words the effect is a result of the electron-phonon interaction. The term electron-phonon implies that both heavy and light particles are involved. The movement of heavy particles (distortions) induced normal coordinates or phonons. The specific property of the Jahn-Teller interaction is that there must be a degeneracy of electronic states to interact with one ore more normal modes of vibration to breaking the symmetry and removing the electronic degeneracy.

The d orbitals contributing in the magnetic moment are presumed to be split by a cubic crystal field into a doubly degenerate e_g and a triply degenerate t_{2g} set which have different spatial distributions (Fig.5-12). The tetragonal distortion splits these orbitals further leading to 1 doubly and 3 singly degenerate sets. The 2 singly degenerate sets $x^2 - y^2$ and $3z^2 - r^2$ are derived from the cubic e_g orbitals and the singly degenerate xy and doubly degenerate $xz \pm yz$ sets from the t_{2g} orbitals (Fig.5-13).

For treatment the strain Kanamori (1960) assumed the phonon states and energies should be a function of the strain. But in most cases this can be neglected because the strain involved is so small. It is useful to divide the lattice modes into three types: the macroscopic strain, acoustic phonons and optic phonons. [62,63,64]

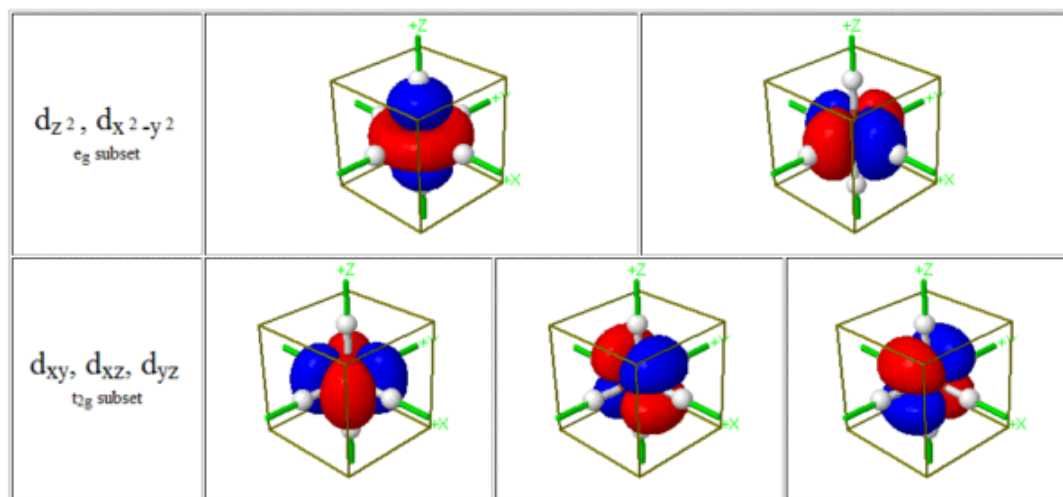


Figure 5-12. Spatial distributions of d-orbitals involving e_g and t_{2g} subsets [65].

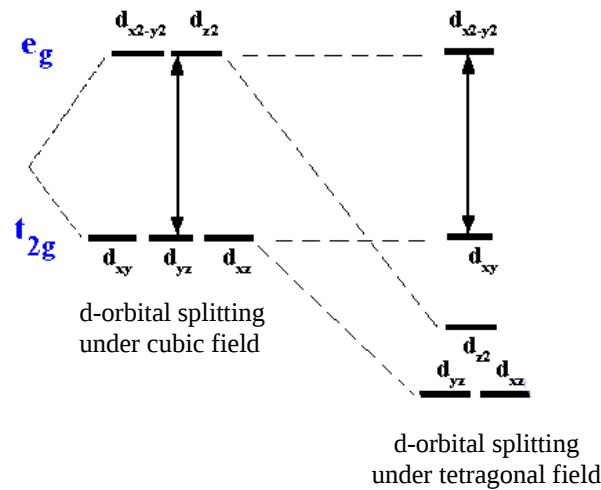


Figure 5-13. Splitting of d-orbital under cubic and tetragonal fields [65].

5.4 Slater-Pauling rule

The Slater-Pauling (SP) rule states that the total magnetic moments of the full Heusler alloys achieved from following formula

$$M_t = Z_t - 24 \quad (5.19)$$

where Z_t is the total number of valence electrons per unit cell. Briefly, the total number of electrons Z_t is given by the sum of the number of spin-up and -down electrons, while the total magnetic moment M_t per unit cell is given by the difference of spin-up and -down states, hence

$$Z_t = N \uparrow + N \downarrow \quad (5.20)$$

$$M_t = N \uparrow - N \downarrow \rightarrow M_t = Z_t - 2N \downarrow \quad (5.21)$$

In this viewpoint it is assumed that first spin down orbitals are filled, hence the occupancy of the spin-down bands does not change and the extra or missing electrons will only occupy the spin-up states. As a result, in Eq-5.19 the number 24 means that there are 12 occupied spin-down states. First, the sp atom creates one s band and three p bands which are fully occupied. In the case of the full-Heusler alloys eight minority d states are occupied per unit cell: the double-degenerated e_g very low in energy, the triple- degenerated t_{2g} orbital, and finally the triple-degenerated t_{1u} just below the Fermi level. In general, the minority valence bands involve twelve electrons: $1 \times s$, $3 \times p$, and $8 \times d$.

It is noted where the total spin magnetic moment is negative the spin-up electrons are designated as the minority and the spin-down ones as the majority states. [66,67,68,69]

6 Shape Memory Effect in Ni₂MnGa

The Ni₂MnGa Heusler alloy showing shape memory effect attracts recently considerable interest due to being ferromagnetic with a Curie temperature T_C of 376 K. The origin of the shape memory effect in Ni₂MnGa is in the martensitic transition which takes place in cooling from the cubic L2₁ Heusler structure to a tetragonal phase around 200 K. The transformation can be described as a simple contraction along one of the [100] directions of the cubic phase without any change in atomic positions. It is notable despite a strong deformation of the unit cell, this transformation is reversible and a single crystal can be cycled through it many times without breaking. The point in this transition is that the lattice distortion breaks the degeneracy of the d bands in the vicinity of the Fermi level causing a redistribution of electrons in these bands with a consequent reduction of the free energy, hence this concept is used to interpret the Density Of State Diagrams in this work. Fig. 6-1 shows a small but distinct anomaly of magnetization occurring in high fields at ≈ 220 K through heating.

This anomaly arises from the change in magnetic anisotropy associated with the structural transition. In the inset of Fig. 6-1 the temperature variation of specific heat is displayed.

Neutron scattering experiments on stoichiometric Ni₂MnGa show that the magnetic moment is mainly localized on the Mn atoms with values ranging from $3.8\mu_B$ to $4.2\mu_B$. Although the magnetic moment of Ni is considerably smaller being about 0.2 - $0.4\mu_B$, Ni atoms are important because they influence the structural stability in L2₁ structure as ab initio calculations in this work show. [64,69,70]

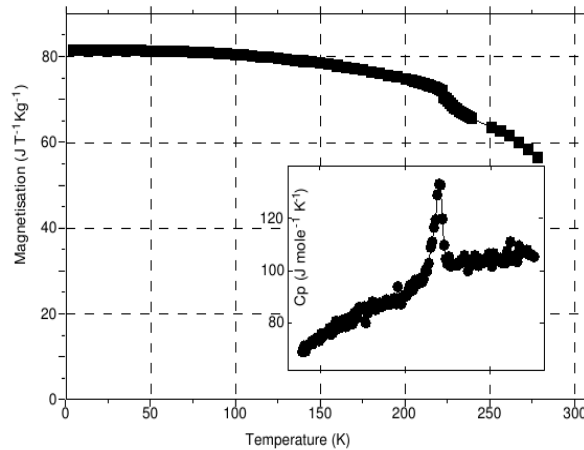


Figure 6-1. Magnetization of Ni₂MnGa at 4.6T plotted as a function of temperature. The inset shows the temperature variation of the specific heat in the vicinity of the phase transition [64].

6.1 Martensitic structure of Ni₂MnGa

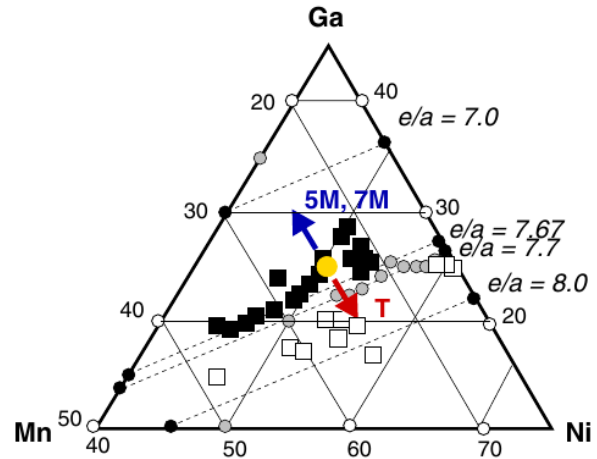
The structure of the martensitic phase for the Ni₂MnGa stoichiometric compound was first studied by neutron elastic scattering and revealed the martensitic structure is

formed by the tetragonal distortion of the initial cubic lattice ($c/a < 1$) and the martensitic unit cell is modulated along the $(110) [1\bar{1}0]_P$ plane and the modulation period is five, seven or ten $(110)_P$ planes (five, seven, ten-layered martensite). For Ni-Mn-Ga the alloys with martensitic transformation temperatures (M_s) below 270K show a five-layered martensite (this group includes the stoichiometric composition); the group with M_s near 270K present five-layered and/or seven-layered martensite, while the group of alloys with M_s above room temperature exhibit the seven-layered martensite or the non-modulated structure without modulation having $c/a > 1$ or a new modulated structure with a period of 10 $(110)_P$ planes (10-layered martensite). It should be noted only 5M and 7M structures show a giant magnetic-field-induced strain MFIS. [50, 51,71]

6.2 Composition and Temperature dependence of the Crystal Structure of Ni–Mn–Ga alloys

The crystal structure of the Ni–Mn–Ga martensitic phase strongly depends on composition and temperature. Increasing e/a with respect to the value of 7.5 for the stoichiometric case stabilizes tetragonal martensite while for $e/a < 7.5$ the modulated phases appear, a behaviour which is qualitatively marked by the arrows in Fig. 6-2 showing a sector of ternary phase diagram of Ni-Mn-Ga. In addition, Fig. 6-2 summarizes the available experimental results from the literature for T_C and T_M which clearly show that there is a relation between the variation of $T_C = T_M$ (i.e. the filled circles marking the magnetostructural transition) with composition which approximately follows the $e/a \approx 7.7$ line. In Ref. [72] the e/a dependence of T_M is described as $T_M = [702.5 (e/a) - 5067]K$ which makes it possible to define the empirical dependence of T_M on the molar Mn content (xMn) and the molar Ga content (xGa) as $T_M = (1960 - 21.1 xMn - 49.2 xGa)$ K. [69,70]

Figure 6-2. a sector of the ternary phase diagram of Ni–Mn–Ga showing the critical range of $7.67 < e/a < 7.7$ of the coupled magnetostructural phase transitions (---). The figure lists experimental data for $T_C < T_M$ (\square), $T_C = T_M$ (\bullet) and $T_C > T_M$ (\blacksquare). The arrows in the figure mark the theoretical prediction for preferred transformation to modulated 5M and 7M and non-modulated tetragonal T structures, respectively. The yellow dot marks the stoichiometric compound Ni_2MnGa [69].



6.3 Density of States Calculation for Ni_2MnGa

Calculation details- In this thesis the calculations were performed by utilizing two different ab initio programs: the open Source Package for Research in Electronic Structure, Simulation, and Optimization (Quantum ESPRESSO) and the full-

potential Korringa-Kohn-Rostoker Munich SPRKKR package. Q-ESPRESSO is an integrated suite of computer codes for electronic-structure calculations and materials modeling, based on density-functional theory, plane waves, and pseudopotentials. The DOS calculations were performed using a spin-polarized scalar-relativistic Hamiltonian, PBE (Pedrew, Bruke, and Ernzerhof) generalized gradient approximation, as exchange-correlation functional.

The calculations done for this work confirmed the literature [45] claimed by lowering the symmetry through tetragonal distortions some degeneracy of the system is removed, and some peaks in the density of states near the Fermi level are split. In this section it will be discussed for Ni₂MnGa.

Fig. 6-3 present calculated total energies for Ni₂MnGa and Ni₂MnSn Heusler alloys as a function of the lattice constant by utilizing the Q-Espresso program. In this Figure can be seen that near lattice constants of 11 a.u. (5.82 Å) and 11.5 a.u. (6.08 Å) for Ni₂MnGa and Ni₂MnSn, respectively, these compounds possess the lowest total energies which confirms the literature [45], as a result to do calculations for these alloys in this thesis the lattice constants of 11 and 11.5 a.u. are considered for Ni₂MnGa and Ni₂MnSn alloys, respectively.

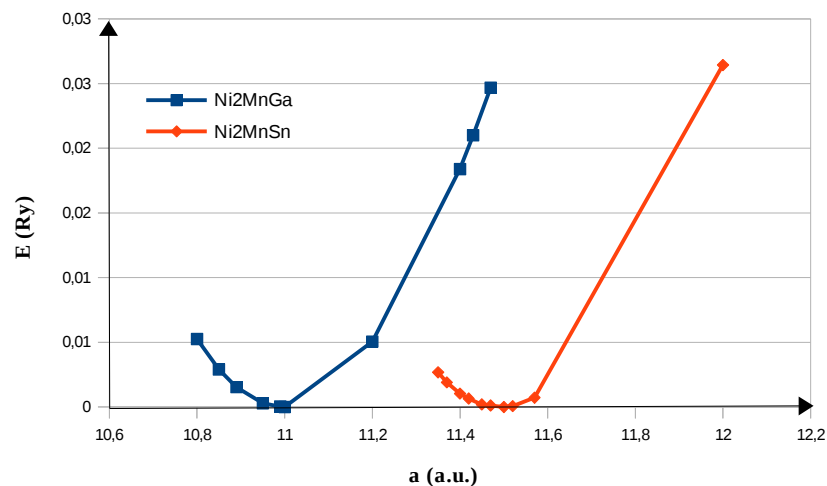


Figure 6-3. The total energy ΔE_{tot} (relative to the lowest energy) variation of Ni₂MnGa and Ni₂MnSn Heusler alloys vs. lattice constants a .

Tetragonal distortions- The unit cell of Heusler alloy crystals can be also regarded as a body centred tetragonal structure which is from „ab initio method“ point of view favorable due to contribution of fewer atoms in unit cell [Fig. 6-4(b)] leading to do time-conserving calculations. The total energy as a function of c/a taken from [45] is presented in Fig. 6-5. In this Figure it can be seen that Ni₂MnGa shows in two points lower energy first in L₂₁ structure with $c/a = 1$ and another in $c/a \approx 1.2$ which is presumed to be the crystal constant in martensite phase.

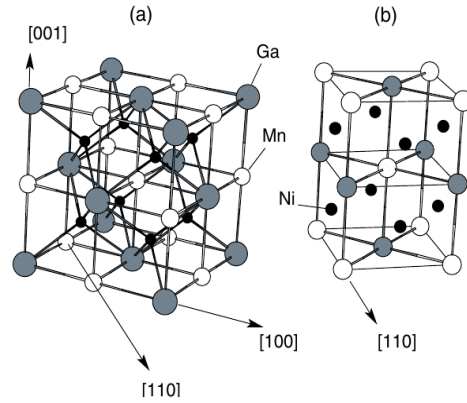


Figure 6-4. (a) The L₂₁ crystal structure with unit cell of space group $Fm\bar{3}m(O_h^5)$ of Ni₂MnGa. The structure of this so-called full Heusler system of type X₂YZ (here X=Ni, Y=Mn and Z=Ga) consists of four interpenetrating fcc lattices and (b) body centered tetragonal unit cell [6].

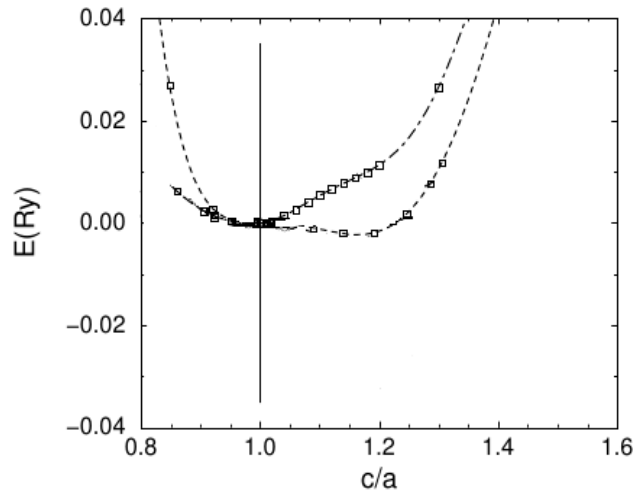


Figure 6-5. The total-energy difference $\Delta E_{tot}^{distorted}$ (relative to the L₂₁ phase) as a function of c/a in the tetragonal distortions for the alloys: Ni₂MnGa (dashed curve); Ni₂MnSn (dotted-dashed) [45].

Fig. 6-6 focused on the energy as a function of the tetragonality c/a for Ni₂MnGa. The inset of Fig. 6-6, with a higher resolution shows in addition to $c/a = 1$ another minimum at $c/a < 1$ with a small energy barrier, about 0.34 meV. The structure with $c/a < 1$ shows smaller energy difference toward $c/a = 1$ than the structure with $c/a > 1$. It is noted the energy required to overcome the barriers in the distortion process is provided by the latent heat. As it is mentioned in literature the latent heat for Heusler alloys varies in the interval of 0.9–5.0 meV/formula unit. Hence it is estimated that at low temperatures the structure with $c/a > 1$ will appear which is confirmed through calculations done for this thesis.

From total energy point of view both programs give for L₂₁ austenite phase the

lowest total energy which contradicts Fig.6-6 but to investigate the stability energy per unit volume is calculated and presented in Table 6-I. As it can be seen martensitic phase with $c/a=0.94$ resulted from both programs is unstable. Therefore as mentioned above at low temperatures the structure with $c/a >1$ is expected to appear. And this can be a proof for „adaptive modulation“ discussed in chapter 5.

The magnetic moments of Ni_2MnGa and contributed Ni and Mn atoms as a function of the tetragonality taken from [8] are presented in Fig. 6-7. Experimentally, the total magnetic moment for the L_{21} cubic structure is $4.17\mu_B$. Fig. 6-7 shows that Ni moment variation around $c/a =1$ looks like the total magnetic variation because two Ni atoms contribute to the total magnetic moment. [8,45,73,74]

The total and local magnetic moments obtained by running „Quantum-Espresso“ and „SPRKKR“ programs are presented in Table 6-II. Total and local density of states for the three minima involving $c/a <1$, $c/a =1$ and $c/a >1$ are presented in Figs. 6-11 to -22.

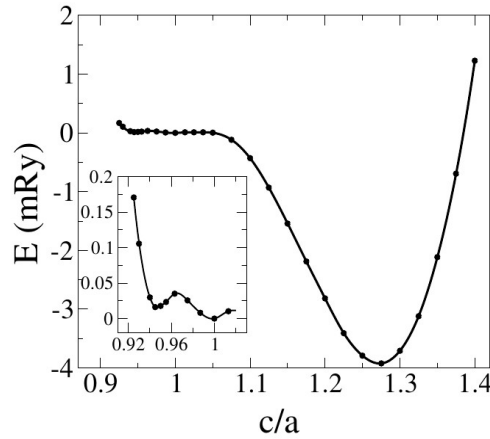


Figure 6-6. Total energy difference $\Delta E_{tot}^{distorted}$ (relative to the L_{21} phase and per formula unit of Ni_2MnGa) as a function of c/a in the tetragonal distortions [8].

Table 6-I. Total energy for the three minima states and energy per unit cell volume $\Delta(E/V)$ calculated by both Q-Espresso and SPRKKR programs.

Structure	Q-Espresso (eV)	SPRKKR (eV)	$\Delta(E/V)^a$ (eV/Å ³)	$\Delta(E/V)^b$ (eV/Å ³)
L_{21}	-7602.67	-166864.65	0.000	0.000
$c/a = 0.94$	-7602.54	-166845.62	-10.05	-214.67
$c/a = 1.25$	-7601.72	-166859.08	31.06	100.64

^a $\Delta(E/V)=(E_{L_{21}}/V_{L_{21}} - E_x/V_x)$, where x is the other states calculated by Q-Espresso

^b calculated by SPRKKR

Table 6-II. Calculated total and local magnetic moments in units of μ_B . Experimental values (Exp.) are taken from [73].

		Ni	Mn	Ga	μ_{tot}
$L2_1$ cubic	Th. (Q-Espresso)	0.36	3.75	-0.14	4.29
	Th. (SPRKKR)	0.30	3.36	-0.06	3.90
	Exp.	0.24	2.74	-0.013	4.17
$c/a = 0.94$	Th. (Q-Espresso)	0.36	3.59	-0.14	4.15
	Th. (SPRKKR)	0.30	2.69	0.00	3.31
	Exp.	0.36	2.83	-0.06	-
$c/a = 1.25$	Th. (Q-Espresso)	0.39	4.14	-0.17	4.71
	Th. (SPRKKR)	0.42	3.88	-0.03	4.69

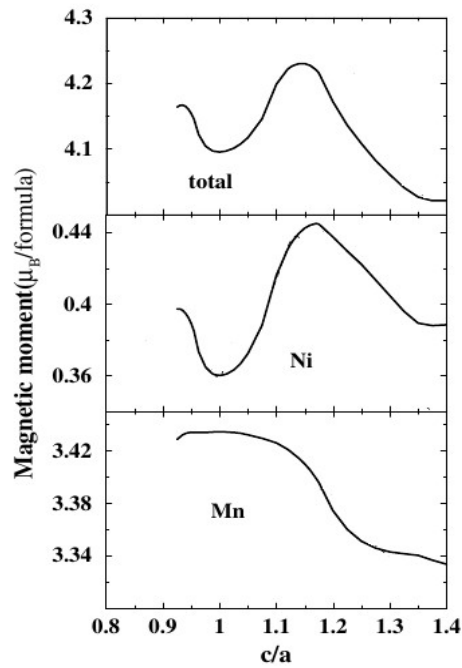


Figure 6-7. Total and local magnetic moments in Ni_2MnGa as a function of tetragonality [8].

First it will be determined for austenite phase which orbitals contribute the most to the local densities of states.

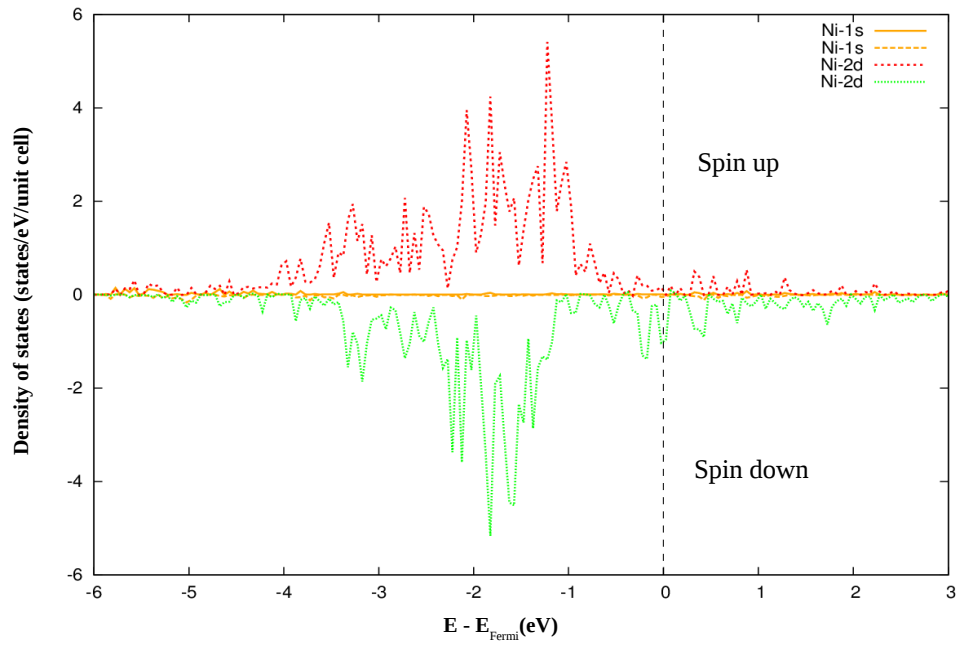


Figure 6-8. Density of states of Ni in Ni_2MnGa for austenite state.

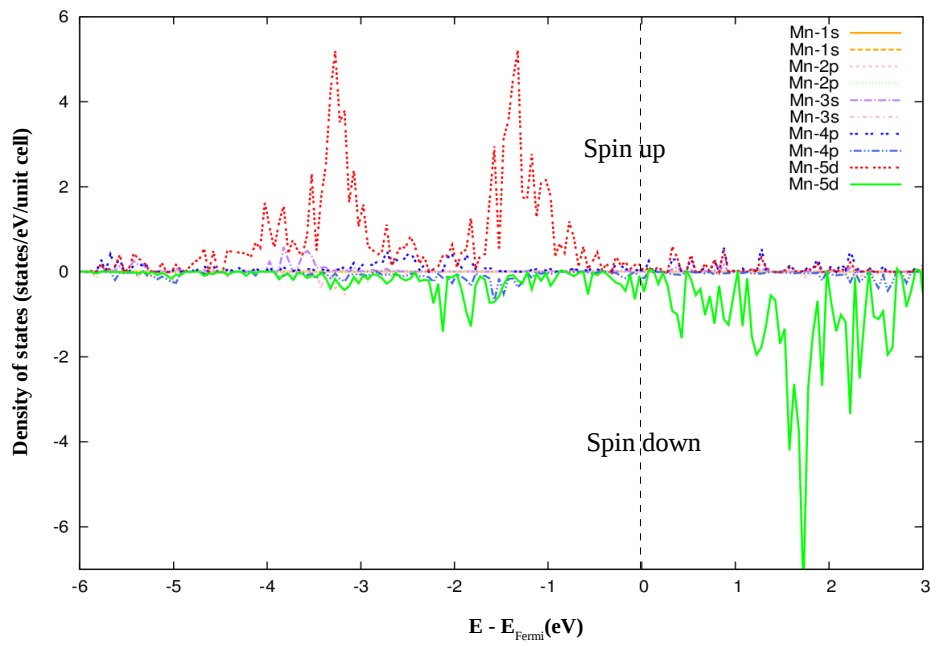


Figure 6-9. Density of states of Mn in Ni_2MnGa for austenite state.

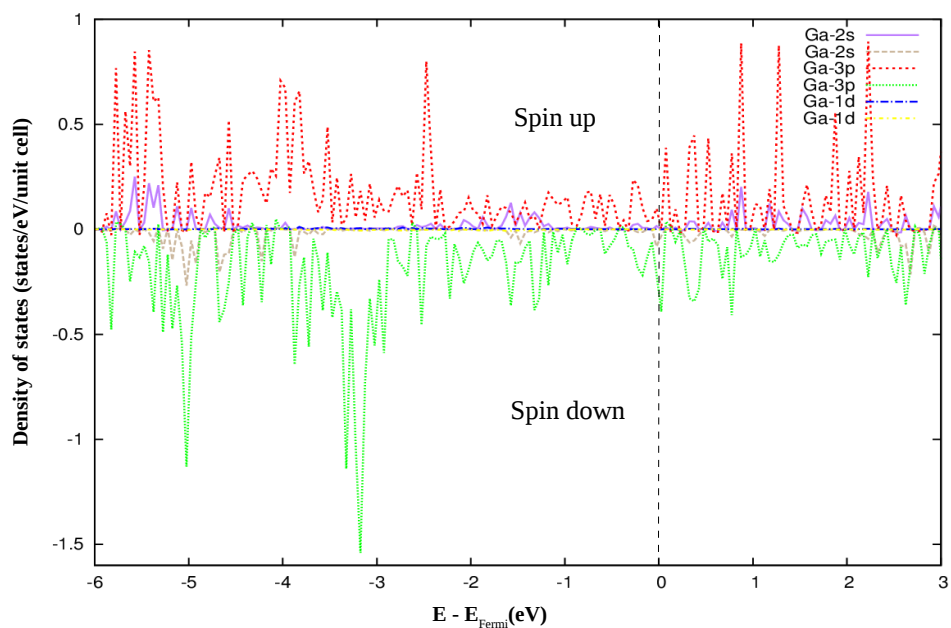


Figure 6-10. Density of states of Ga in Ni₂MnGa for austenite state.

From Figs.6-8 to -10 it is concluded that d-orbitals of Ni and Mn and p-orbital of Ga contribute the most to local density of states which was expected because these orbitals are not full occupied. As a result they contribute the most in total density of state of Ni₂MnGa-L2₁ phase. It can be seen that contribution of Ga p-orbital is negligible. Figs. 6-11 and -12 present the total density of states for Ni₂MnGa in austenite state. Fig. 6-12 shows a peak at Fermi level. Fig 6-13 shows the d-orbital density of states of Ni and Mn for austenitic state. This Figure confirms this fact that at Fermi level minority electrons of Ni play the most important role to occur instability and as a result leads to tetragonal distortion to lower the energy at Fermi level.

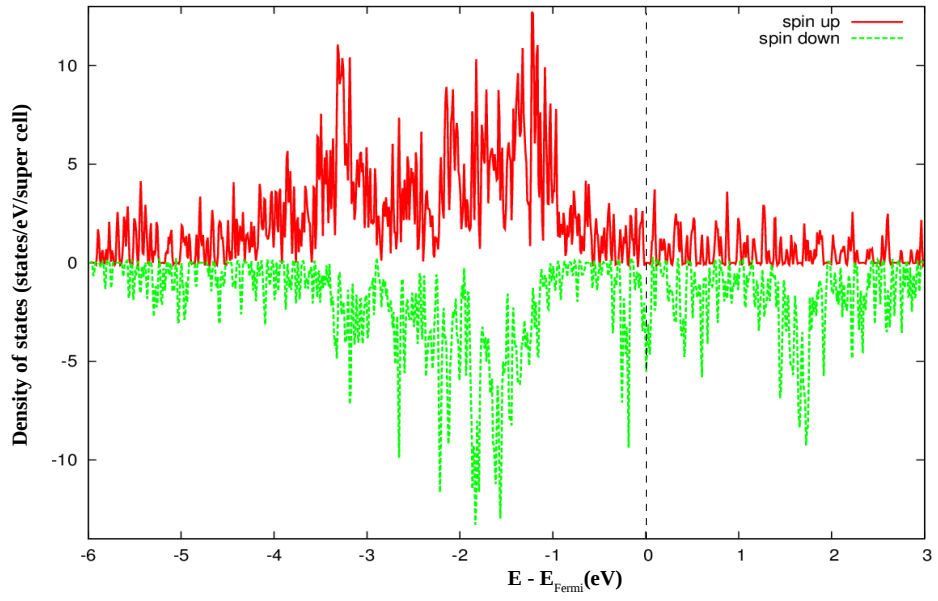


Figure 6-11. Total Density of states for Ni_2MnGa in austenitic phase.

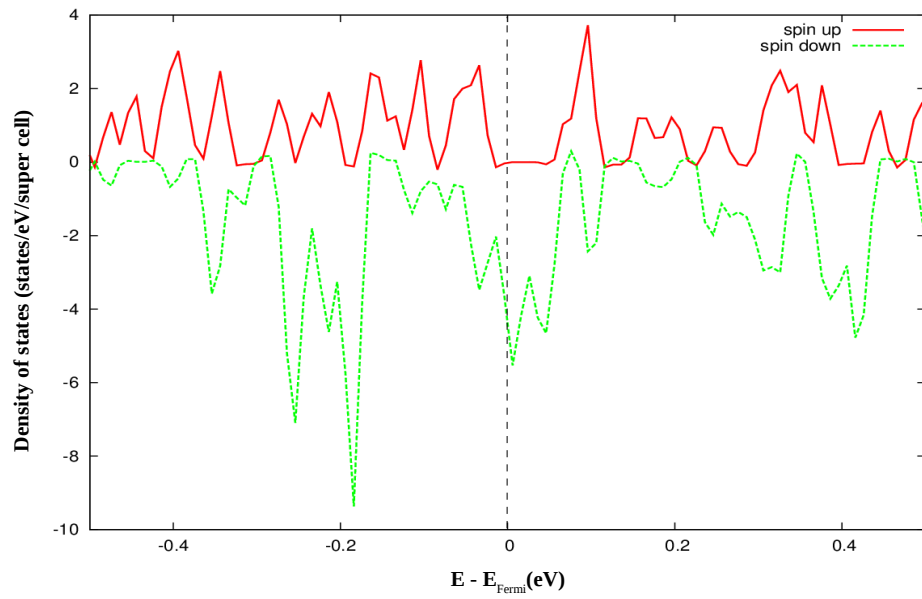


Figure 6-12. Total density of states for Ni_2MnGa in austenitic phase close to Fermi level.

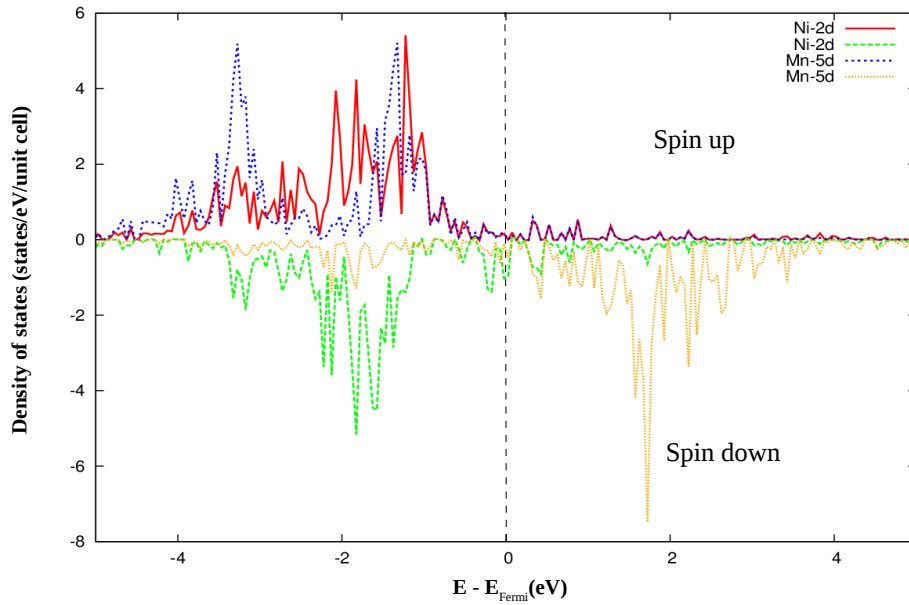


Fig 6-13. Density of states of Ni and Mn d- orbitals for austenitic state.

Fig.6-14 presents the SPRKKR outcome for austenitic phase.

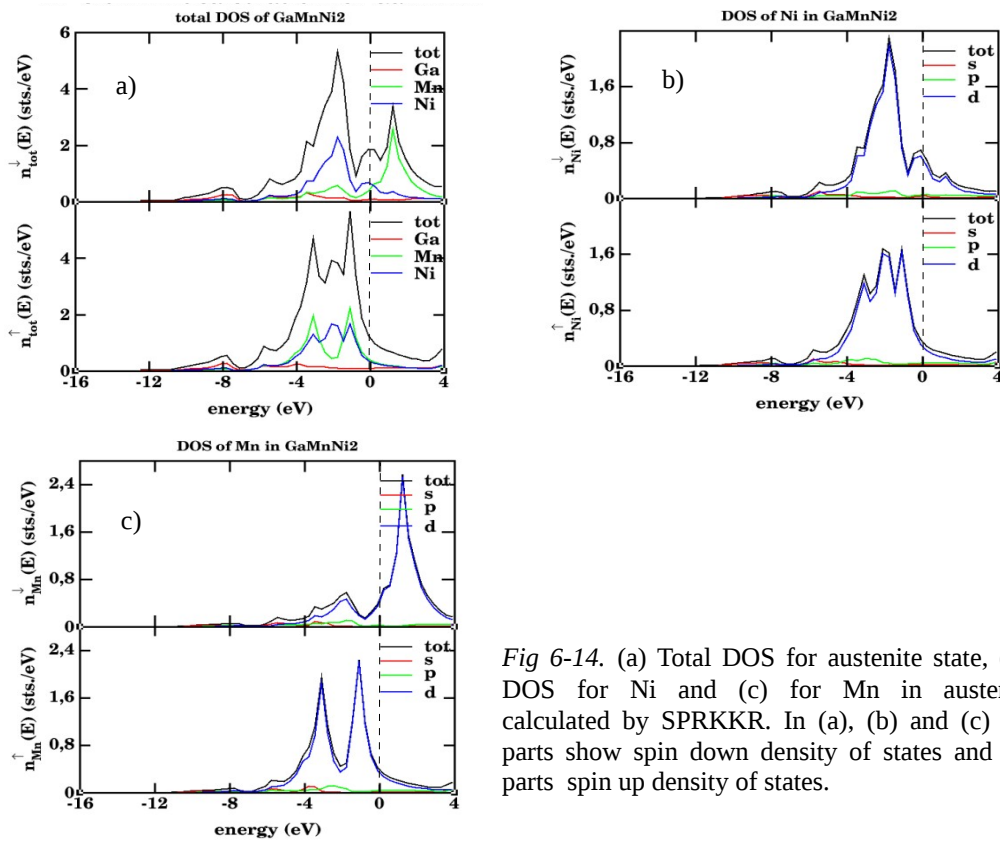


Fig 6-14. (a) Total DOS for austenite state, (b) partial DOS for Ni and (c) for Mn in austenite state calculated by SPRKKR. In (a), (b) and (c) the upper parts show spin down density of states and the lower parts spin up density of states.

As it is seen it shows also a peak at Fermi level due to Ni-minority electrons. For martensite states only Ni and Mn d-orbitals will be investigated, because for austenitic state it has been found out that these orbitals contribute the most to partial and total densities of states for Ni₂MnGa. In the following first the density of states in martensite phase with $c/a < 1$ will be presented and afterwards the ones for $c/a > 1$.

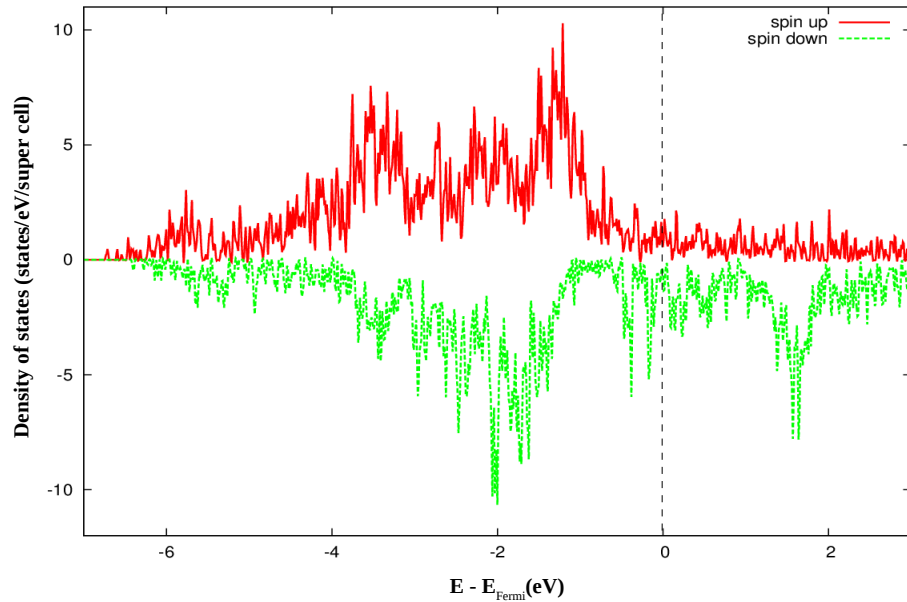


Figure 6-15. Total Density of states for Ni₂MnGa in martensitic phase ($c/a < 1$).

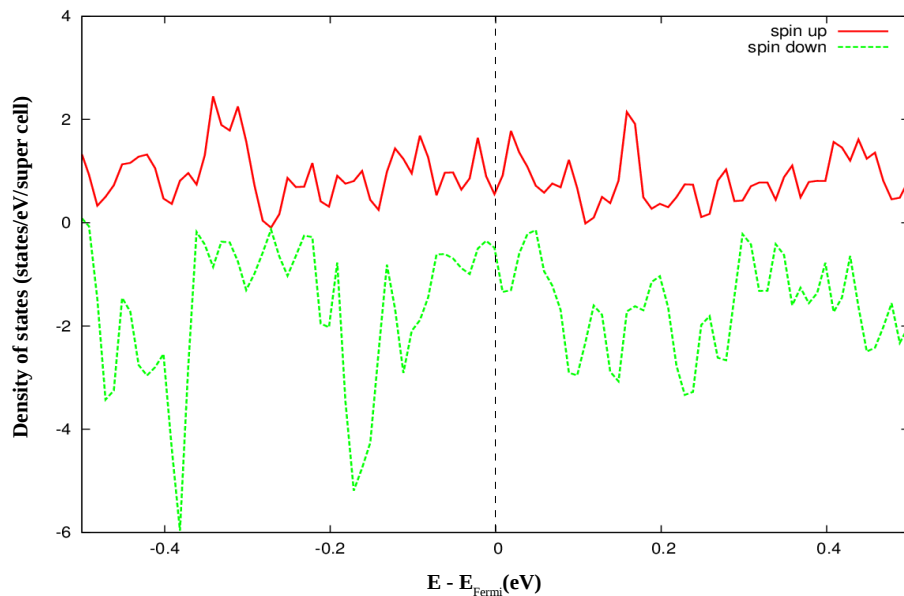


Figure 6-16. Total density of states for Ni₂MnGa in martensitic phase ($c/a < 1$) close to Fermi level.

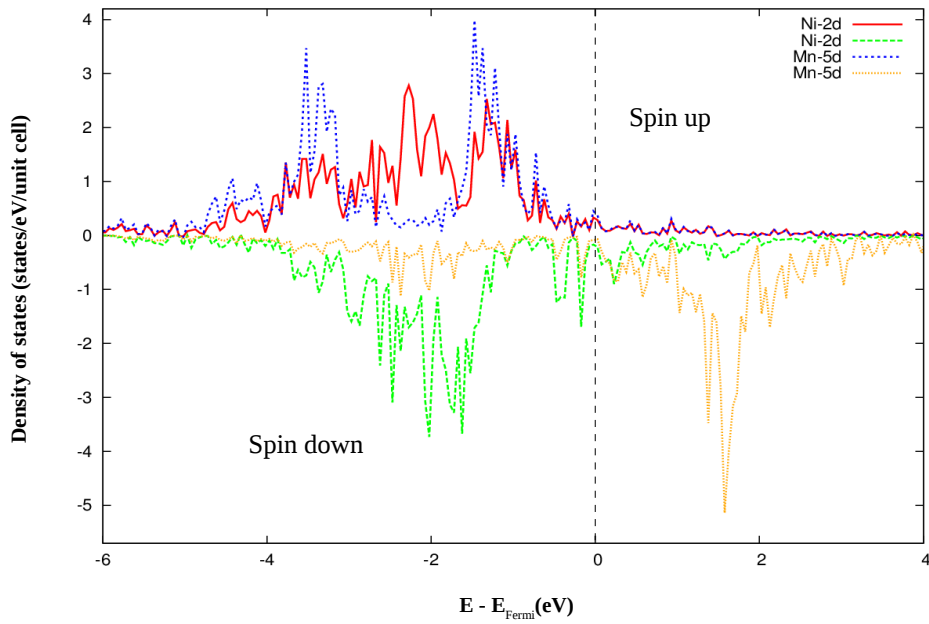


Fig 6-17. Density of states of Ni and Mn d-orbitals for martensitic phase ($c/a < 1$).

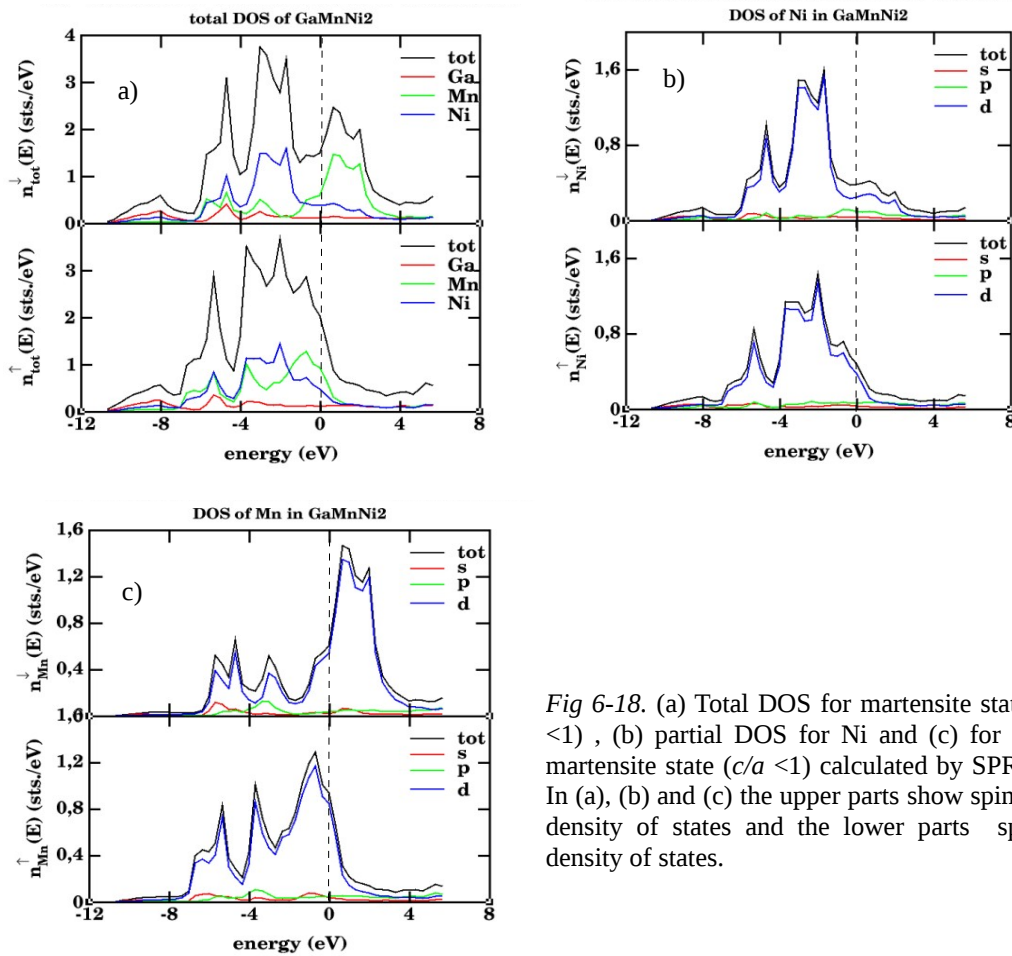


Fig 6-18. (a) Total DOS for martensite state ($c/a < 1$), (b) partial DOS for Ni and (c) for Mn in martensite state ($c/a < 1$) calculated by SPRKKR. In (a), (b) and (c) the upper parts show spin down density of states and the lower parts spin up density of states.

With regard to Figs. 6-16 and -18(a) for $c/a < 1$ neither Q-Espresso nor SPRKKR results show a peak at Fermi level meaning this state is stable which is in contrast to stability discussions done before.

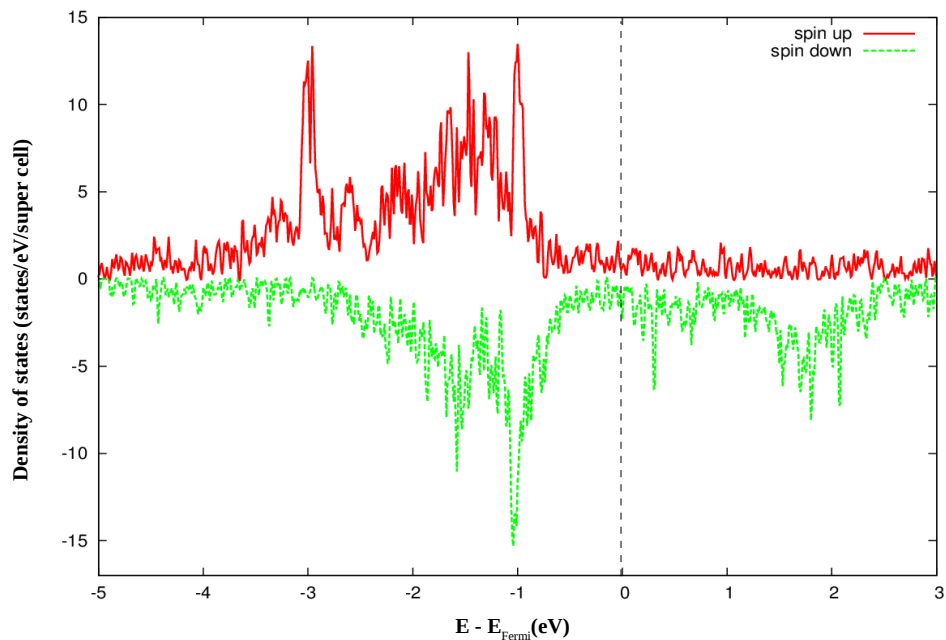


Figure 6-19. Total density of states for Ni_2MnGa in martensitic phase ($c/a > 1$).

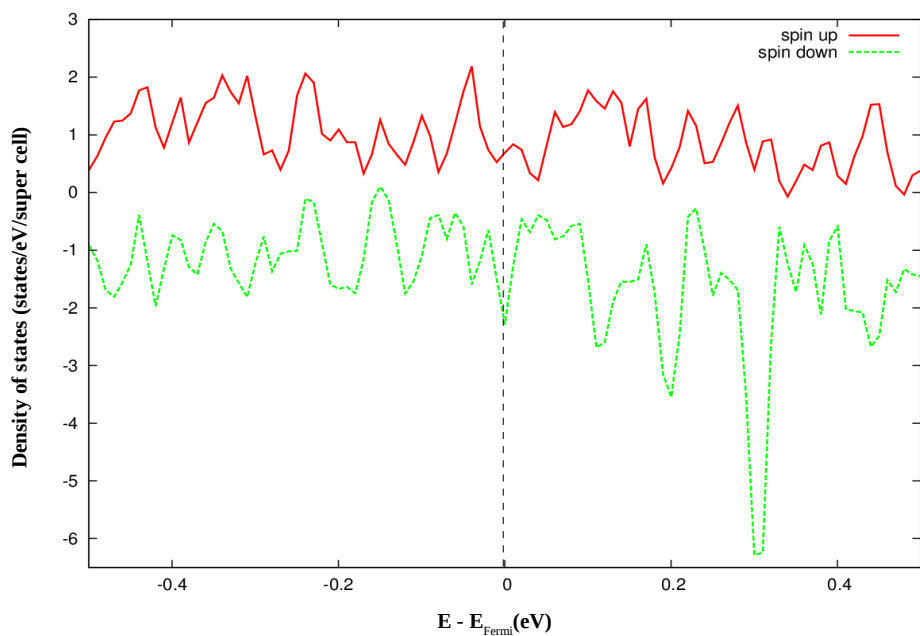


Figure 6-20. Total density of states for Ni_2MnGa in martensitic phase ($c/a > 1$) close to Fermi level.

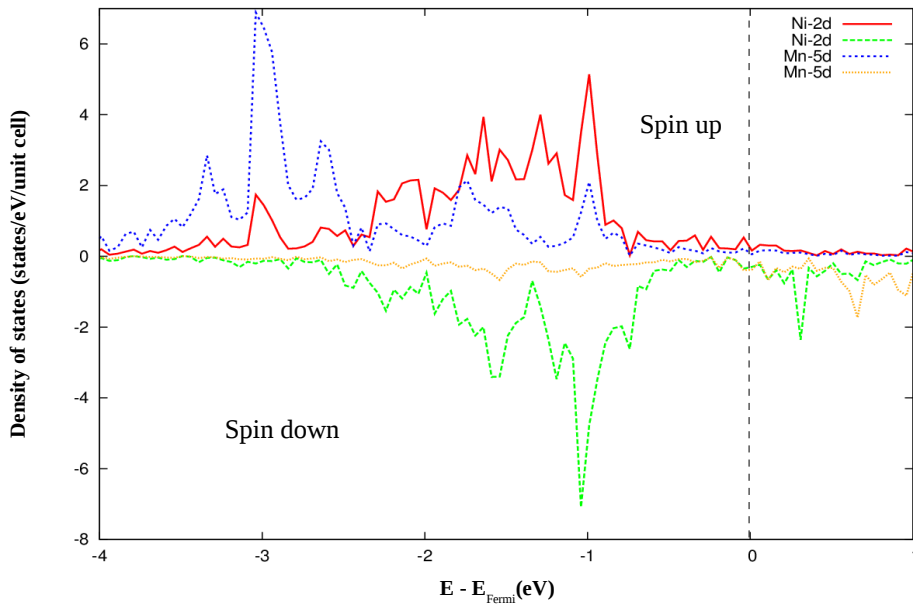


Figure 6-21. Density of states of Ni and Mn d-orbitals for martensitic phase ($c/a > 1$).

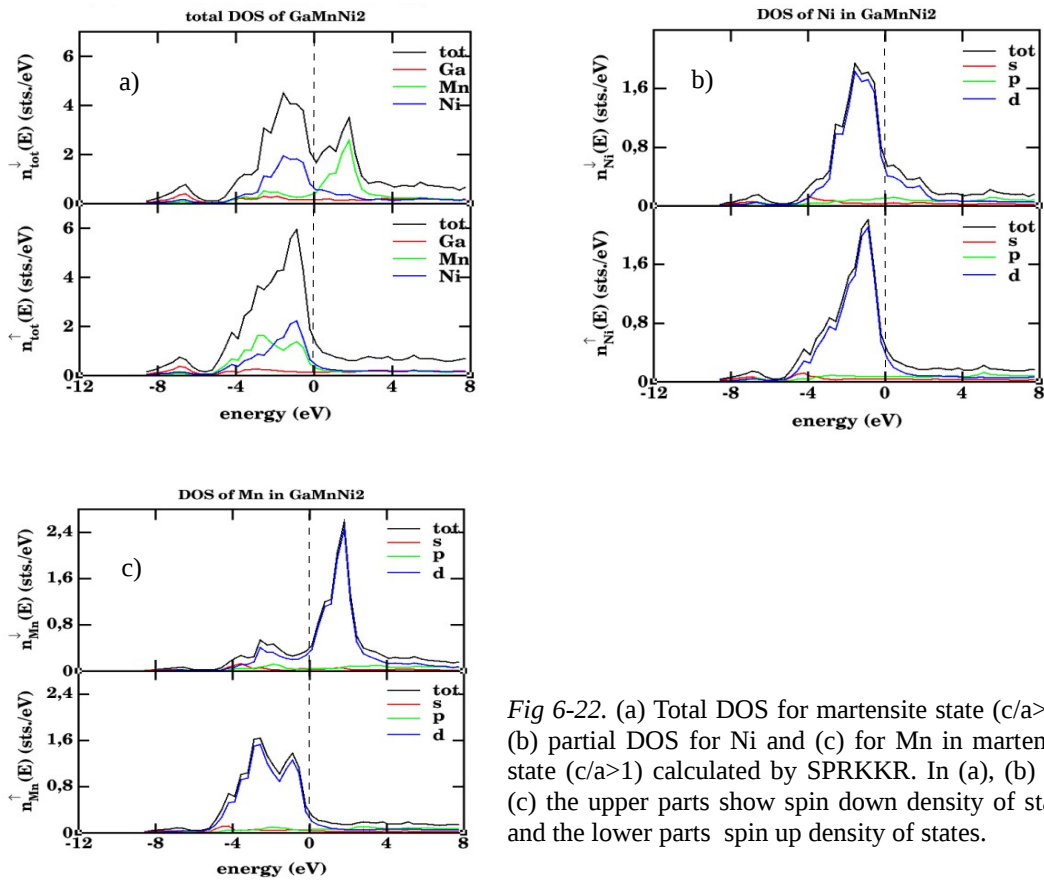


Fig 6-22. (a) Total DOS for martensite state ($c/a > 1$), (b) partial DOS for Ni and (c) for Mn in martensite state ($c/a > 1$) calculated by SPRKKR. In (a), (b) and (c) the upper parts show spin down density of states and the lower parts spin up density of states.

Fig. 6-20 depicts calculated total density of state by Q-Espresso close to Fermi level showing a small peak at Fermi level which in comparison to the peak appeared in L2₁ total DOS (Fig. 6-11) could not cause a splitting in energy at Fermi level, hence it is concluded martensitic state with $c/a > 1$ is also stable which is in agreement with stability discussion. But with regard to Figs. 6-16 and -20 martensitic state with $c/a < 1$ seems to be more stable than $c/a > 1$ which is contrary to stability discussions.

In conclusion, through figures of total density of states neither by Q-Espresso nor by SPRKKR the most stable phase could not be determined. Instead of that total energy per unit cell volume must be considered to determine the right state for martensitic phase. However, the figures of density of states calculated by utilizing an all-electron program as presented in [8] show the expected graphs as density of state for Ni₂MnGa. Therefore it is inferred for achieving the coincident results with experiments the core electrons must be considered to do these calculations.

It is noted that total magnetic moment of Ni₂MnGa in L2₁ state is estimated better with Quantum-Espresso in comparison to experimental data, while the site projected magnetic moments resulted from SPRKKR calculations (Table 6-II) are closer to experimental results.

At the end the charge density distribution obtained by Q-Espresso in the (0 0 1) plane where martensite transition appears involving the different atoms, i.e., Ni, Mn and Ga for these minima are presented in Fig. 6-23. In this figure the charge density is changing between 0.00-0.09 $e/a.u^3$ (e is the absolute value of the electron charge).

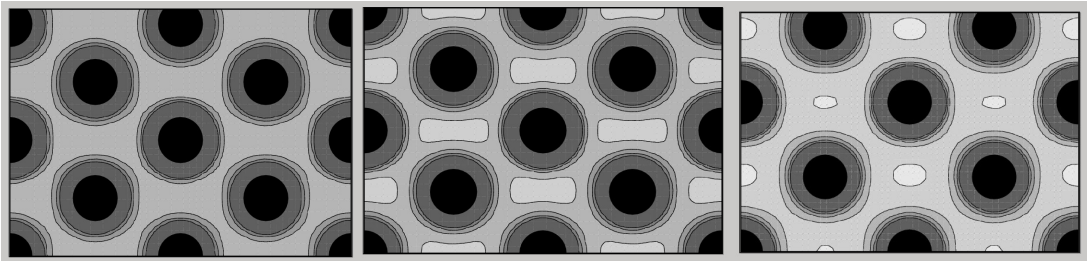


Figure 6-23. Charge density distribution in the (0 0 1) plane from left to right for: a) $c/a=0.94$, b) $c/a=1$ and c) $c/a=1.25$.

As it was expected, this figure confirms this fact that by contracting the structure ($c/a < 1$) the density of charge becomes denser, while for $c/a > 1$ phase it is thinner in comparison to L2₁ [Fig.6-23 (b)]. As a result total magnetic moment will increase from $c/a < 1$ to $c/a > 1$ which is in agreement with Table 6-II.

7 Shape Memory Effect in Ni–Mn–Sn alloys

Although it is reported that Ni₂MnSn stoichiometric alloy shows no martensitic transformation, in Ni-Mn-Sn off-stoichiometric alloys a first-order magnetic transition (FOMT) from a high temperature cubic phase (austenite) to a low temperature orthorhombic phase (martensite) with decreasing temperature is observed. The MT in these alloys is often accompanied by the abrupt changes of magnetization and resistance which result in several interesting phenomena such as meta-magnetic SME (Shape Memory Effect), large magneto-resistance, and large magneto-caloric effect (MCE). As a result, applications of Ni-Mn-Sn-based Heusler alloys are highly expected in actuators, sensors, and magnetic refrigerators, etc. While Ni₂MnSn stoichiometric compound in the austenitic phase has a L2₁ cubic structure, the martensitic structure can be 10M, 14M, L1₀, 4O depending on composition. [7,75]

In the following, the possibility of occurrence of Shape Memory Effect in Ni₂MnSn stoichiometric alloy in austenitic phase is investigated by calculation the Density Of State (DOS) and observation at Fermi level.

7.1 Density of State Calculation for Ni₂MnSn

The total Density Of States (DOS) for Ni₂MnSn calculated by applying „Q-Espresso“ code is shown in Figs. 7-1 and -2. Fig. 7-2 representing total DOS close to Fermi level shows a peak for minority electrons at the Fermi level contrary to literature [45] to deny the existence of martensitic transformation.“ In Fig.7-3 site spin projected for Ni and Mn d-electrons has been depicted. This figure presents that Ni- and Mn-minority electrons contribute to forming the peak at Fermi level.

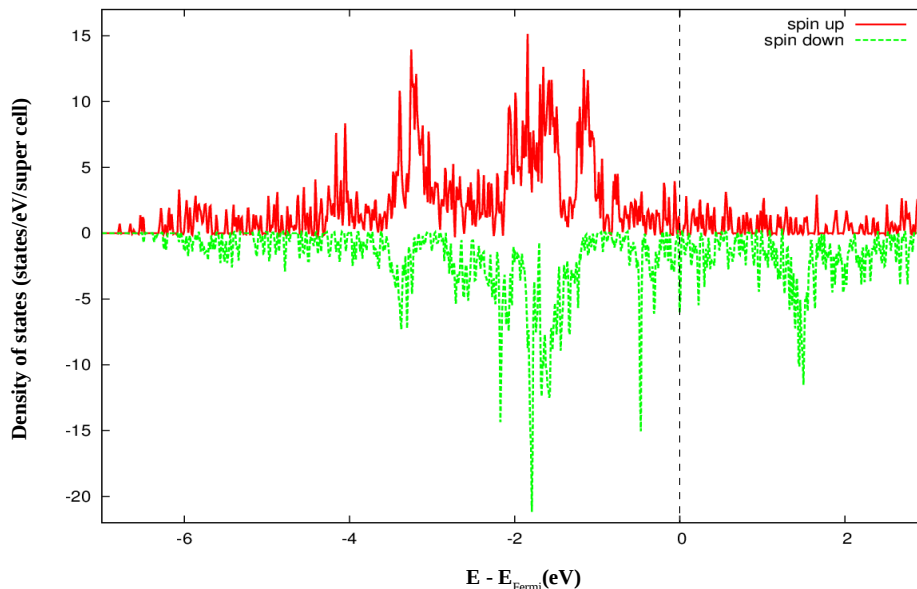


Figure 7-1. Total DOS for Ni₂MnSn in austenitic phase.

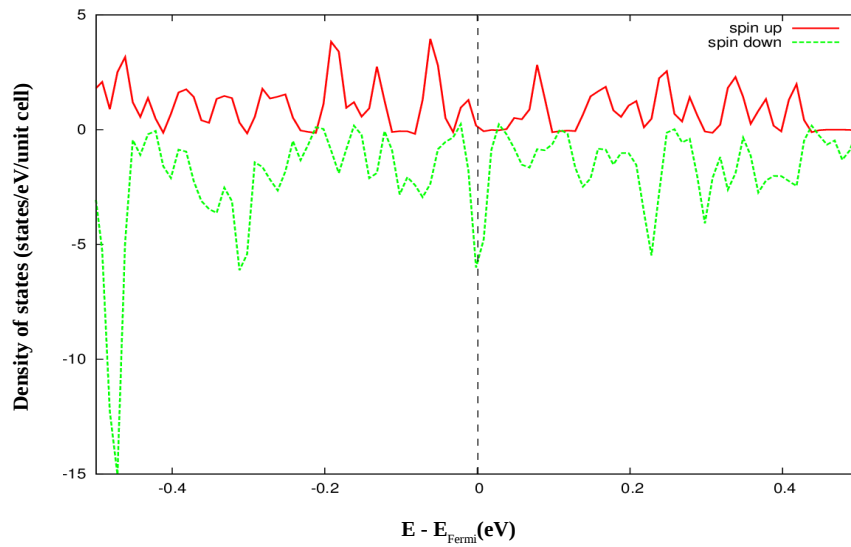


Figure 7-2. Total DOS for Ni₂MnSn in austenitic phase close to Fermi level.

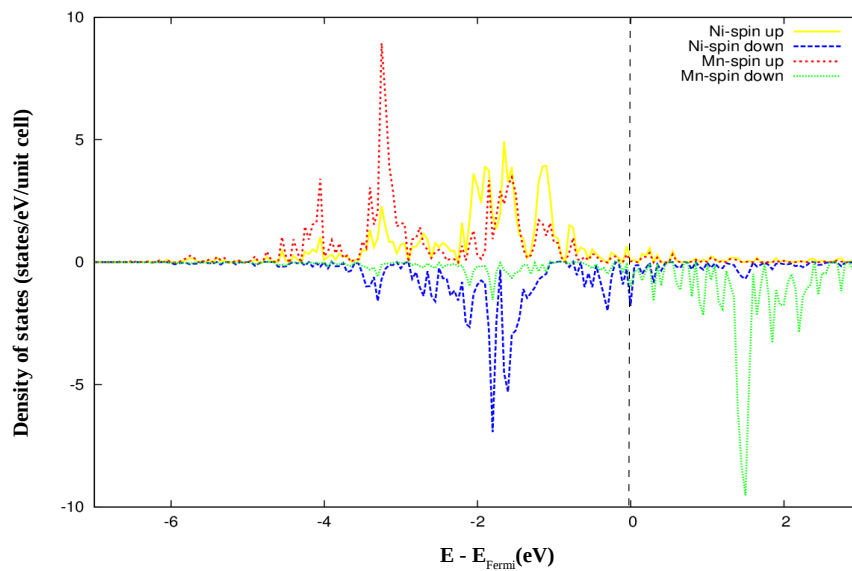


Figure 7-3. Site spin-projected d-electron state densities for Ni and Mn in Ni₂MnSn austenitic phase.

To prove the results achieved by „Q-Espresso“, Density Of State for Ni₂MnSn has also been calculated with SPRKKR program. As it could be seen in Fig. 7-4, SPRKKR results also confirm the result of „Q-Espresso“ and shows only a small peak at Fermi level. Table 7-I shows the total and local magnetic moments resulted from „Q-Espresso“ and „SPRKKR“ programs. In Fig. 6-6 the total energy difference relative to L2₁ for Ni₂MnSn austenite structure has been shown as a function of tetragonality (c/a).

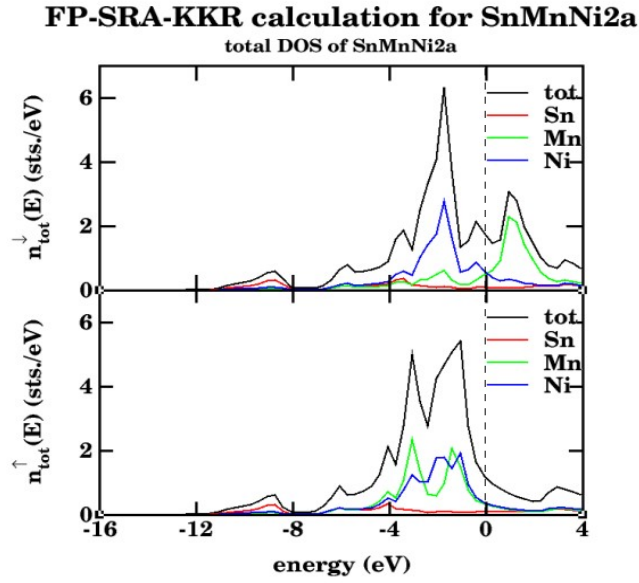


Figure 7-4. SPRKKR calculated total DOS and site spin-projected d-electron state densities for Ni, Mn and Sn in Ni₂MnSn austenite phase. Upper part presents spin down density of states and lower part spin up density of states.

Concerning electronic aspects, the magnetic moment as a function of tetragonality has been investigated and is presented in Fig.7-5. The total and local magnetic moments obtained by running „Q-Espresso“ and „SPRKKR“ programs are given in Table 7-I. Magnetic moments calculated by Q-Espresso are overestimated as a result of applying ultrasoft pseudopotentials to do these calculations while in SPRKKR method full potential is considered.

Table 7-I. Total and local magnetic moments per site in units of μ_B .

$L2_1$		Ni	Mn	Sn	μ_{tot}
Q-Espresso	Th.	0.21	3.96	-0.13	4.21
SPRKKR	Th.	0.19	3.55	-0.05	3.87
	Exp. [45]	-	-	-	4.05

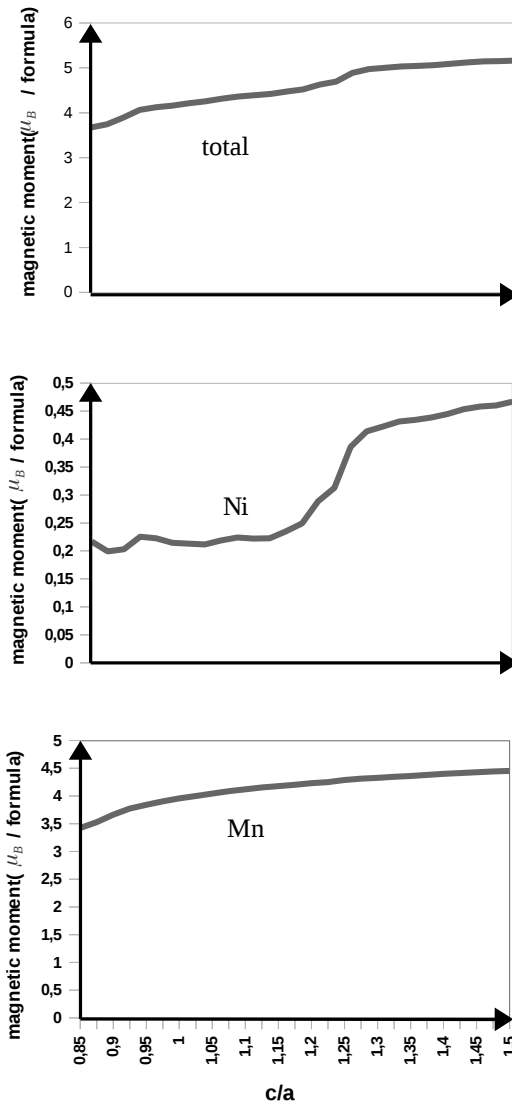


Figure 7-5. Total magnetic moment and contributions associated with Ni and Mn atoms in Ni_2MnSn as a function of tetragonality (c/a).

8 Multilayer systems consisting of Ni₂MnGa and Ni₂MnSn

In this section electronic and magnetic moment structures of some multilayers consisting of Ni₂MnGa and Ni₂MnSn Heusler alloys in austenite phase are studied to investigate the occurrence of martensitic transformation. Spin polarization is also studied for these configurations.

1) Ga-Sn-Ga trilayer system

First, the trilayer structure consisting of two Ni₂MnGa layers as upper and lower layers and Ni₂MnSn as middle layer with a layer of vacuum above all of them to simulate better the real system, are studied, Fig. 8-1 shows the structure of this trilayer system from two aspects, plotted by Xcrysden [76], a crystalline and molecular structure visualisation program. As it has been mentioned in chapter 5 Fig. 5-2 austenite structure can also be shown as a tetragonal positioned in the center of austenite structure which makes the calculations much easier and faster because of less number of atoms existing in the tetragonal unit cell in comparison to L2₁ cubic structure. As a result to do the calculations of this chapter a simple tetragonal with an average constant cell (average of Ni₂MnGa and Ni₂MnSn constant cells) of 4.2425 Å is assumed as supercell. This system contains 26 atoms including 14 Ni, 6 Mn, 4 Ga and 2 Sn -atoms. From this point on, this system will be referred to as Ga-Sn-Ga. It should be noted that the thickness of each layer is 6 Å and of vacuum is about 10 Å.

Fig. 8-2 shows the total density of states for the system, separated for electrons with spin-up and -down and Fig.8-3 shows the total density of states close to Fermi level. According to the manner for concluding whether a diagram shows a martensitic transformation or not in [45] this diagram shows a very small peak at Fermi level, as a result no martensite transition is expected for this system. Fig. 8-4 presents the site projected density of states for d-electrons of Ni- and Mn- atoms of Ni₂MnGa layers. It should be noted that density of states of Ni and Mn constructing Ni₂MnSn alloy are a little different from those of Ni₂MnGa. Fig. 8-5 presents the magnetic moments for Ni, Mn and Sn versus thickness of multilayer. Total magnetic moment of the system is 26.97 μ_B and the total energy is -2314.84 Ry.

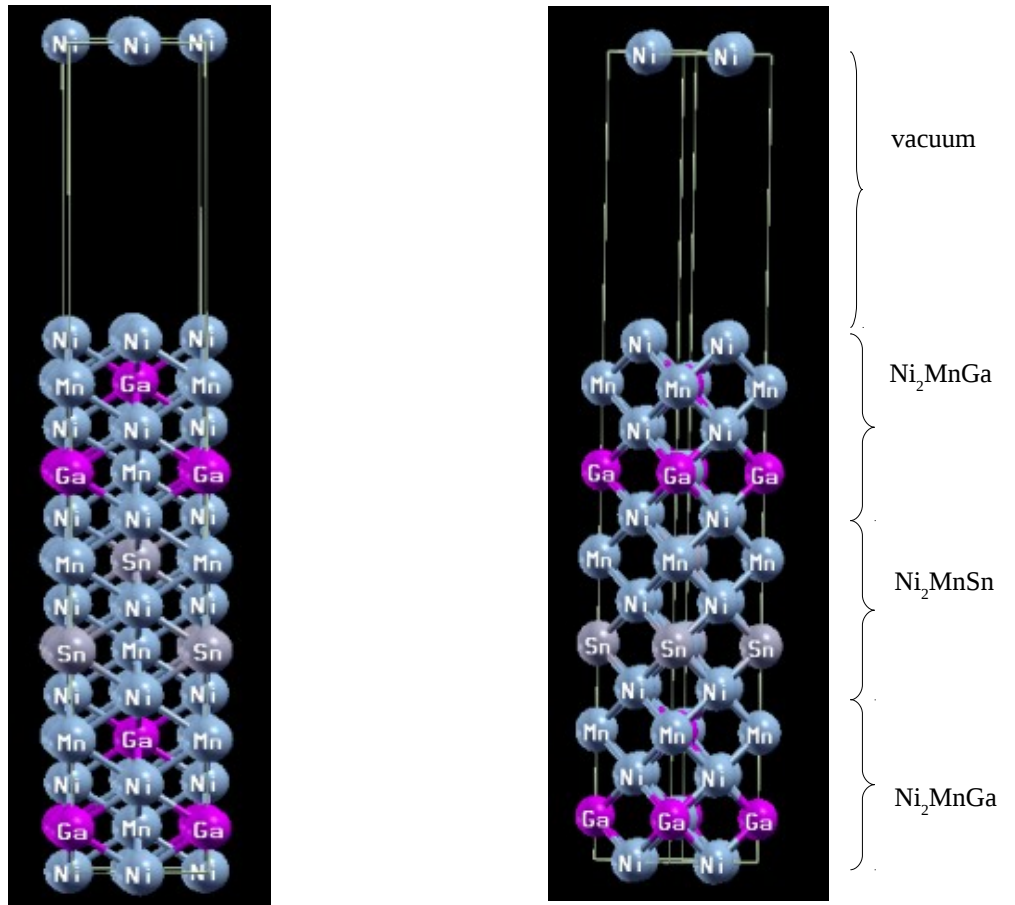


Figure 8-1. Structure of trilayer system in austenitic phase consisting of two Ni₂MnGa layers as upper and lower layers and one Ni₂MnSn layer in the middle with a layer of vacuum on top of the system [76].

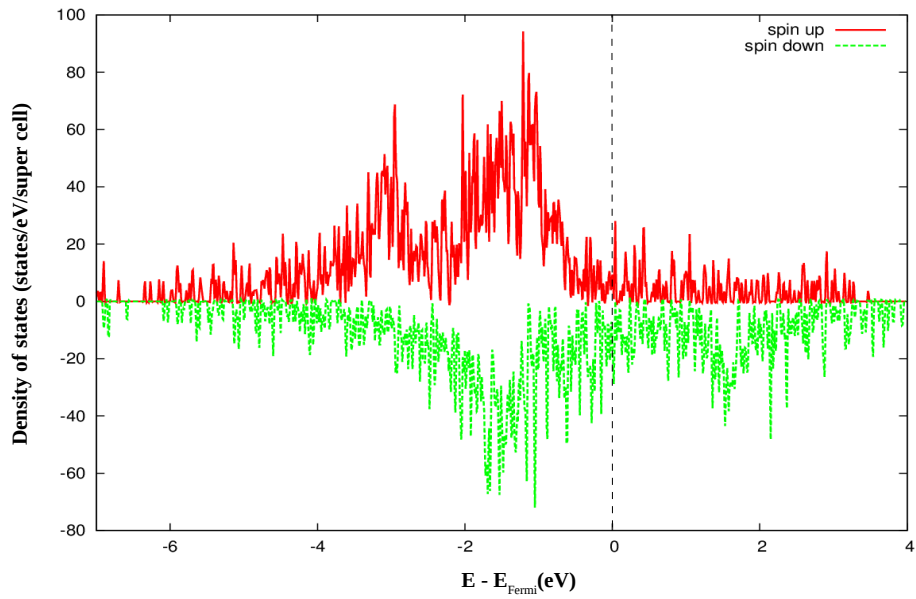


Figure 8-2. Total DOS for Ga-Sn-Ga austenitic trilayer system.

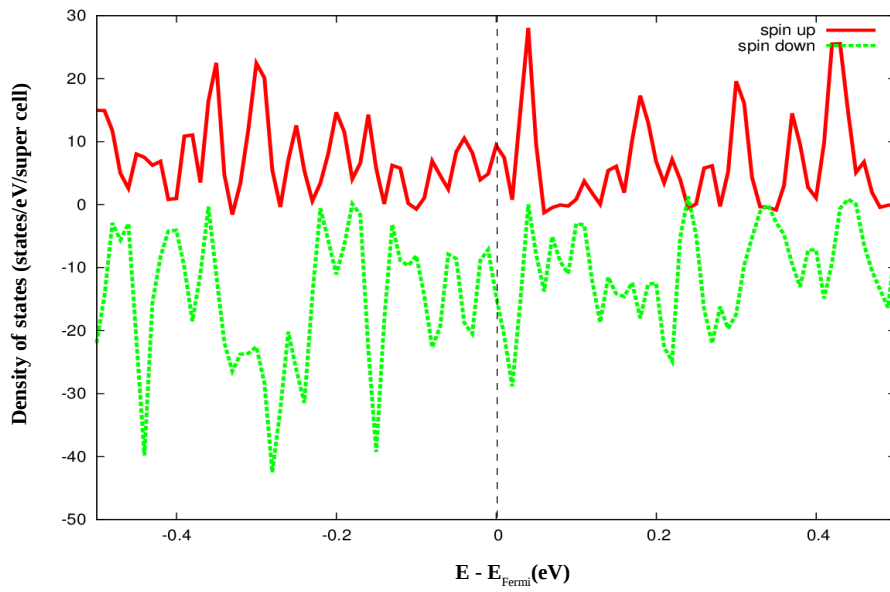


Figure 8-3. Total DOS for Ga-Sn-Ga austenitic trilayer system close to Fermi level.

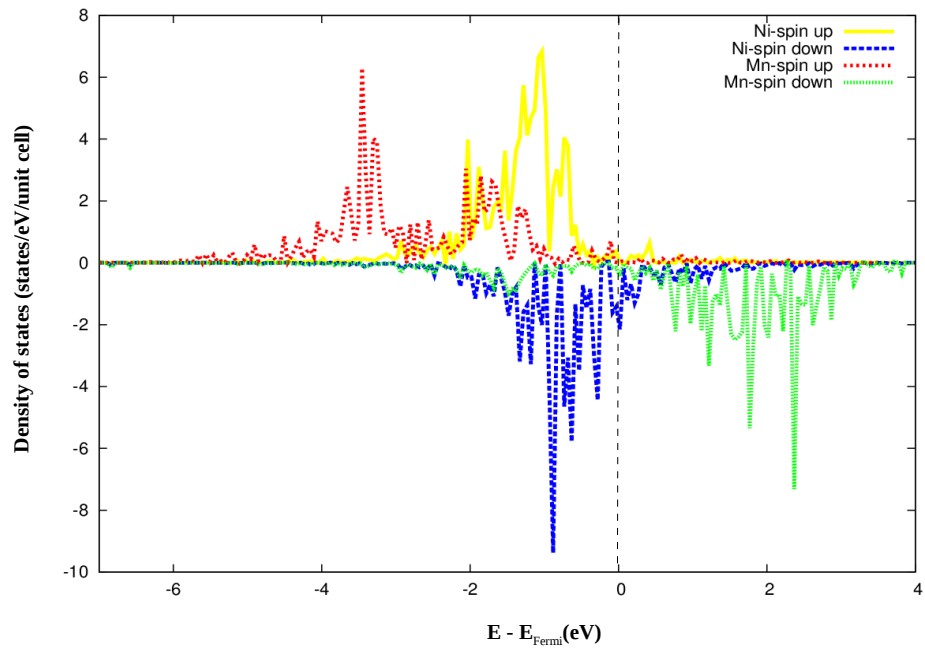


Figure 8-4. PDOS for Ni and Mn d-electrons of Ni_2MnGa -layer involving the austenitic trilayer system Ga-Sn-Ga.

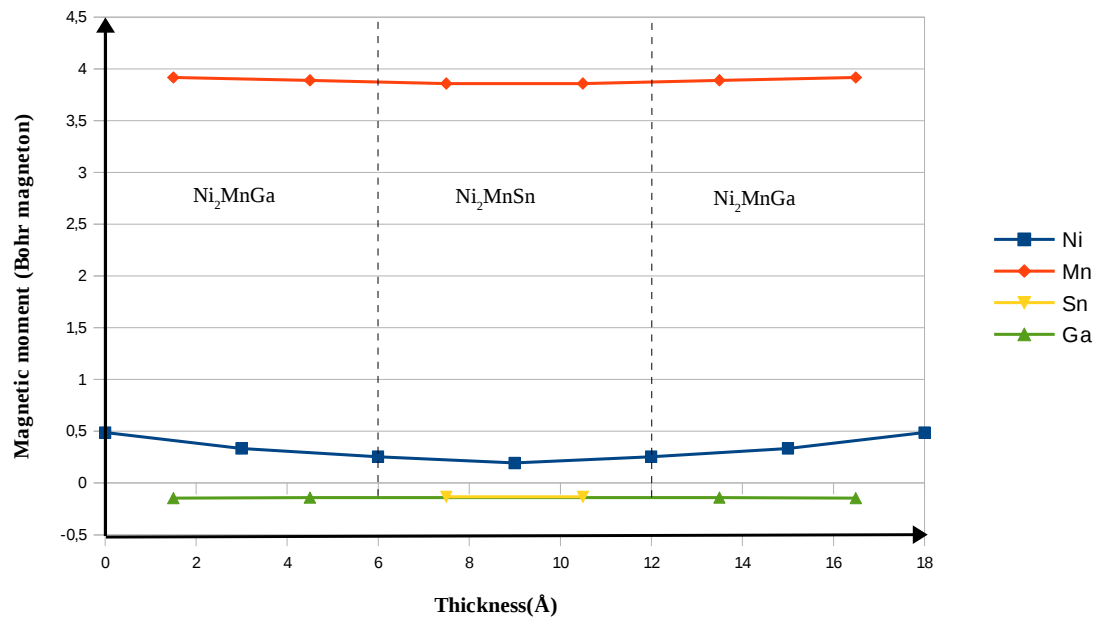


Figure 8-5. Magnetic moments of Ni, Mn, Ga and Sn involving the austenitic trilayer system Ga-Sn-Ga vs. thickness of trilayer.

2) Sn-Ga-Sn trilayer system

In order to compare, the trilayer system which would be referred to as Sn-Ga-Sn has been studied as well; upper and lower layers are of Ni₂MnSn and the middle layer is of Ni₂MnGa. The assumed structure is the same as previous one. The total energy is -2312.85 Ry. The total energy of Ga-Sn-Ga system is lower than Sn-Ga-Sn system, this means that the previous system is a little more stable than the current system. This system contains 26 atoms including 14 Ni, 6 Mn, 2 Ga and 4 Sn -atoms. Total magnetic moment for this system is $25.90\mu_B$ that is less than previous structure. Fig. 8-6 shows the total density of states for Sn-Ga-Sn system, and Fig. 8-8 presents the site projected density of states for Ni and Mn atoms separated for electrons with spin-up and -down. Fig. 8-9 presents the change of magnetic moments of four elements along this trilayer. As it is seen magnetic moments for Ga and Sn are the same, of Mn is almost constant of $4\mu_B$, Ni magnetic moment oscillates along the multilayer. Regarding to Fig. 8-7 it is probable this system shows the martensitic transformation due to majority electrons resulting from Ni- and Mn- majority electrons.

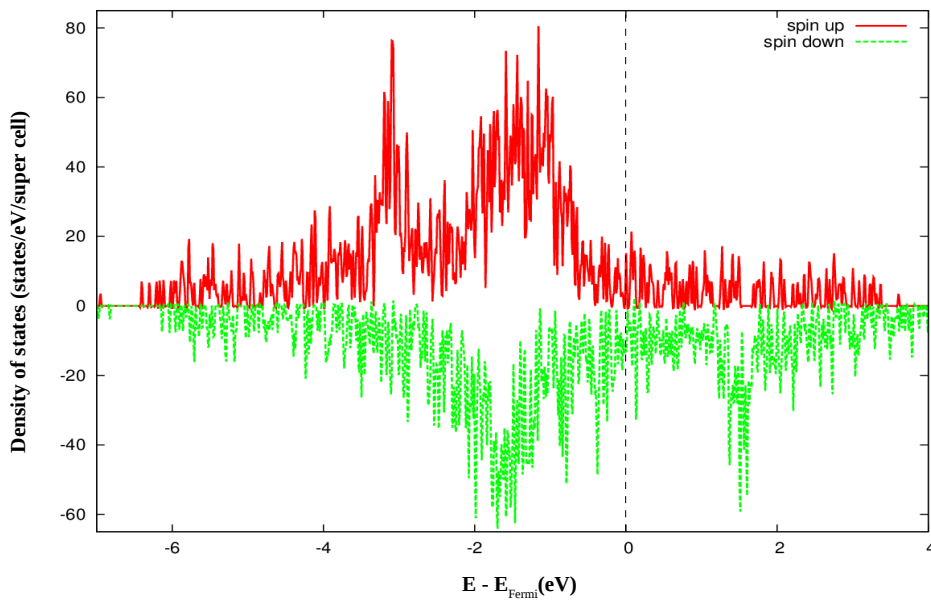


Figure 8-6. Total DOS for Sn-Ga-Sn austenitic trilayer system.

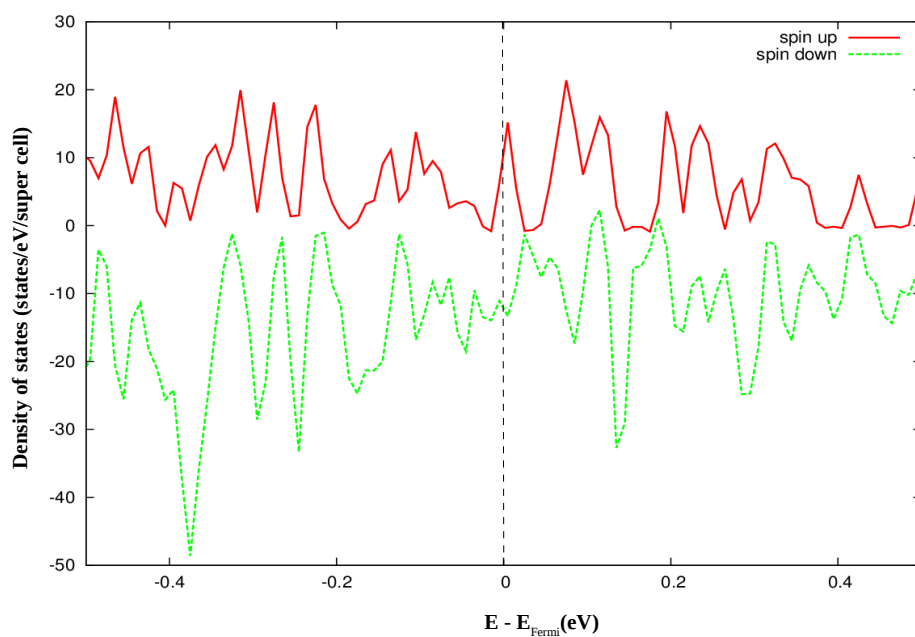


Figure 8-7. Total DOS for Sn-Ga-Sn austenitic trilayer system close to Fermi level.

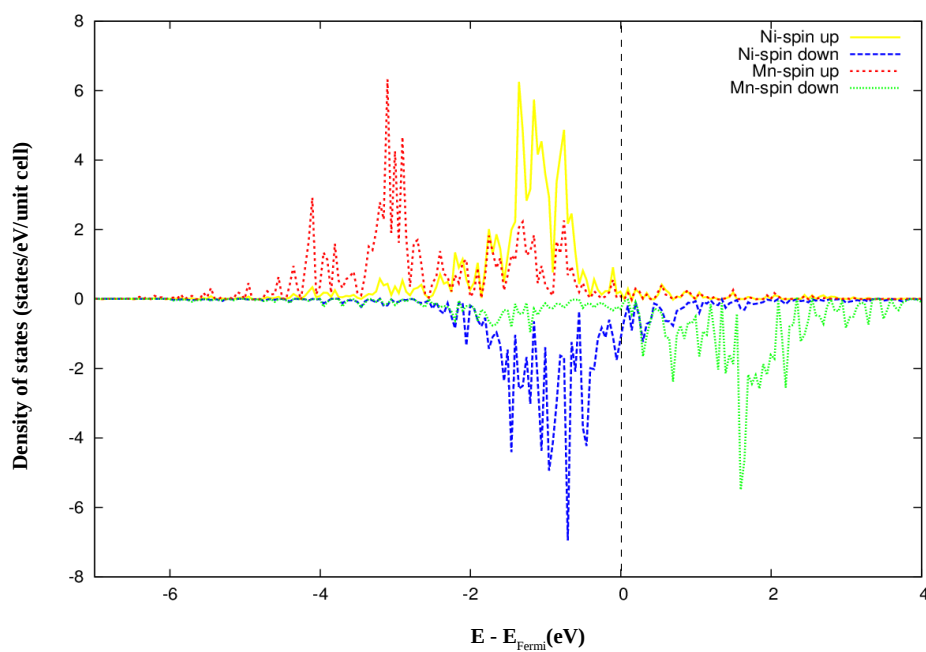


Figure 8-8. PDOS for Ni and Mn d-electrons involving the austenitic trilayer system Sn-Ga-Sn.

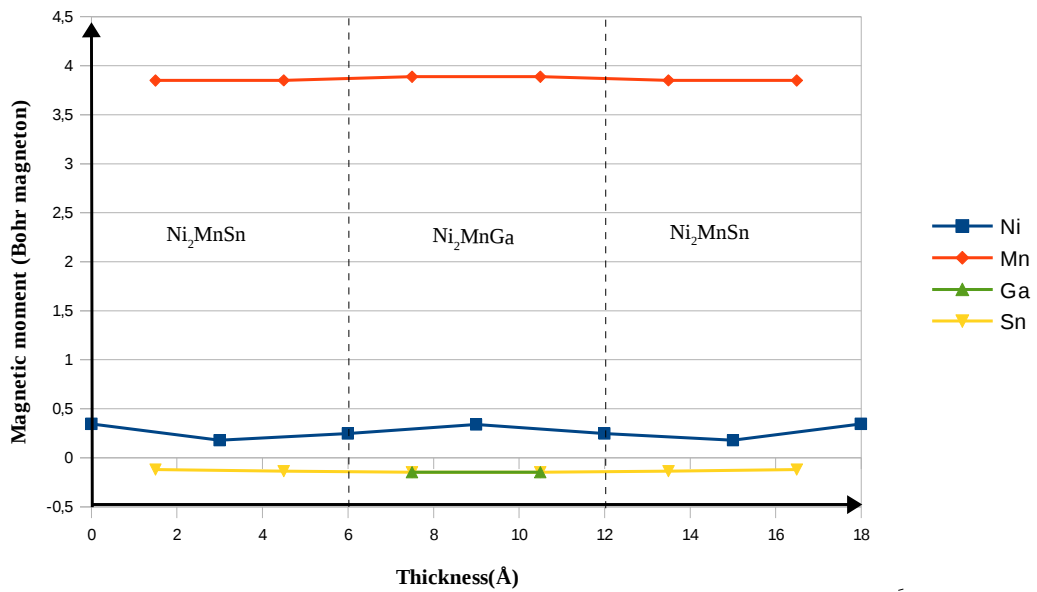


Figure 8-9. Magnetic moments of Ni, Mn, Ga and Sn involving the austenitic trilayer system Sn-Ga-Sn vs. thickness of trilayer.

For further information from the trilayer Ga-Sn-Ga system the thickness of layers will be increased; in this way that first only the thickness of Ni₂MnGa layers and then only of Ni₂MnSn layer and finally of all three layers will be increased and the results will be discussed.

3) 2Ga-Sn-2Ga fivelayer system

Fivelayer system consisting of four layers of Ni₂MnGa and one layer Ni₂MnSn which is sandwiched between these four Ni₂MnGa layers in the way that two layers of Ni₂MnGa are above and two others are below the Ni₂MnSn layer. This means, in this system Ni₂MnGa layer has a thickness of 6 Å but the thickness of Ni₂MnSn layer is doubled to 12 Å and vacuum is about 12 Å. The current fivelayer system will be named as 2Ga-Sn-2Ga in this work. This system contains 42 atoms including 22 Ni, 10 Mn, 8 Ga and 2 Sn -atoms. The total magnetic moment of system is 44.50 μ_B and the total energy is -3745.13 Ry. Figs. 8-10 and -12 present the total DOS and PDOS for Ni and Mn atoms respectively, Fig.8-11 shows the changes close to Fermi level. As it could be seen there is no peak at Fermi level, therefore martensite transition for this system is impossible. Fig.8-13 shows the changes of magnetic moment for either element along the thickness of fivelayer-system.

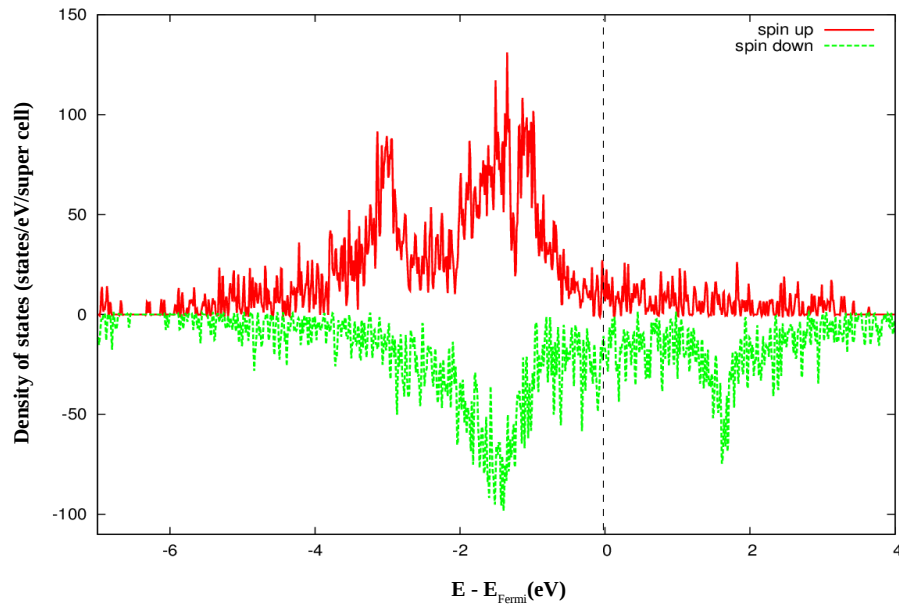


Figure 8-10. Total DOS for 2Ga-Sn-2Ga austenitic fivelayer system.

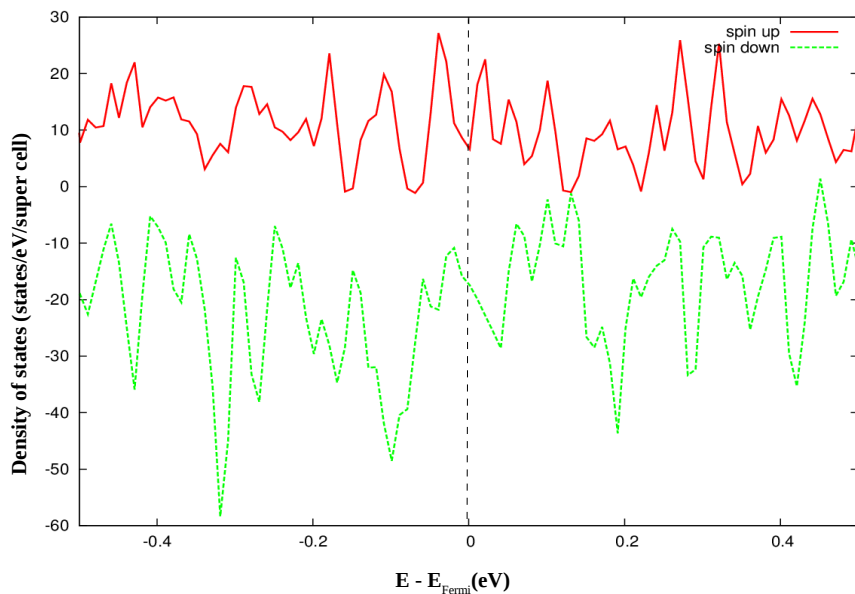


Figure 8-11. Total DOS for 2Ga-Sn-2Ga fivelay system close to Fermi level.

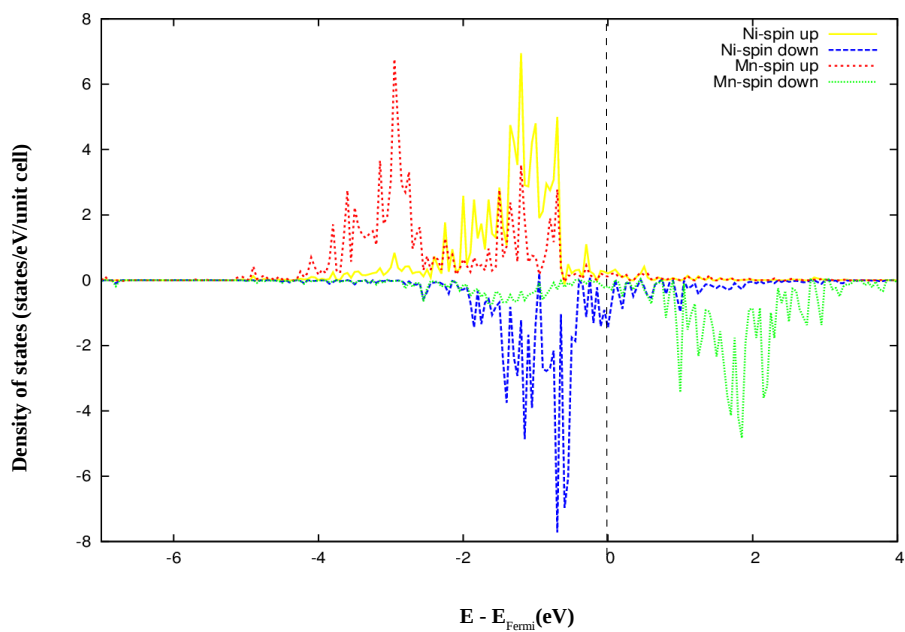


Figure 8-12. PDOS for Ni and Mn d-electrons involving the austenitic fivelay system 2Ga-Sn-2Ga.

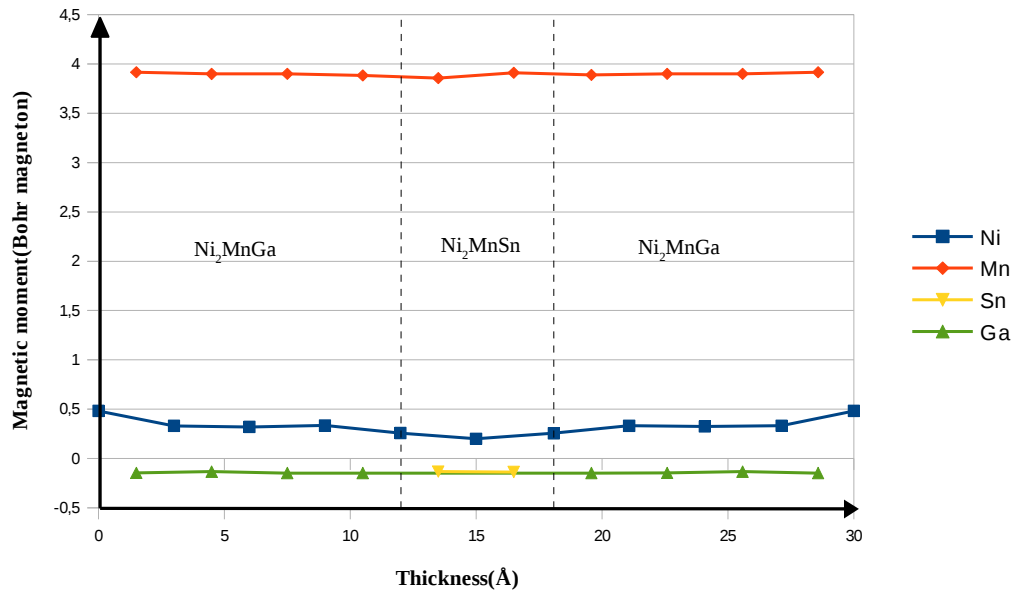


Figure 8-13. Magnetic moments of Ni, Mn, Ga and Sn involving the austenitic fivelay system 2Ga-Sn-2Ga vs. thickness of fivelay.

4) Ga-2Sn-Ga fourlayer system

As the next step, as mentioned before the system in which the thickness of Ni_2MnSn layer of previous studied trilayer system would be doubled to 12 Å and it will be referred to as Ga-2Sn-Ga. The vacuum thickness is about 12 Å. For this system also a supercell like previous cases is assumed.

Figs. 8-14 and -15 show total DOS and Fig.8-16 shows PDOS of Ni and Mn atoms for Ga-2Sn-Ga system. Fig. 8-15 shows a large peak at the Fermi level due to the minority d-electrons of Ni (Fig. 8-16) therefore a martensitic transformation is expected for this system, although the simple Ga-Sn-Ga system has shown no martensitic transformation. This system contains 34 atoms including 18 Ni, 8 Mn, 4 Ga and 4 Sn -atoms. The total energy for this system is -3027.97 Ry . Total magnetic moment for this system is $35.23\mu_B$ and the change of magnetic moments of individual atoms versus thickness of system is depicted in Fig. 8-17.

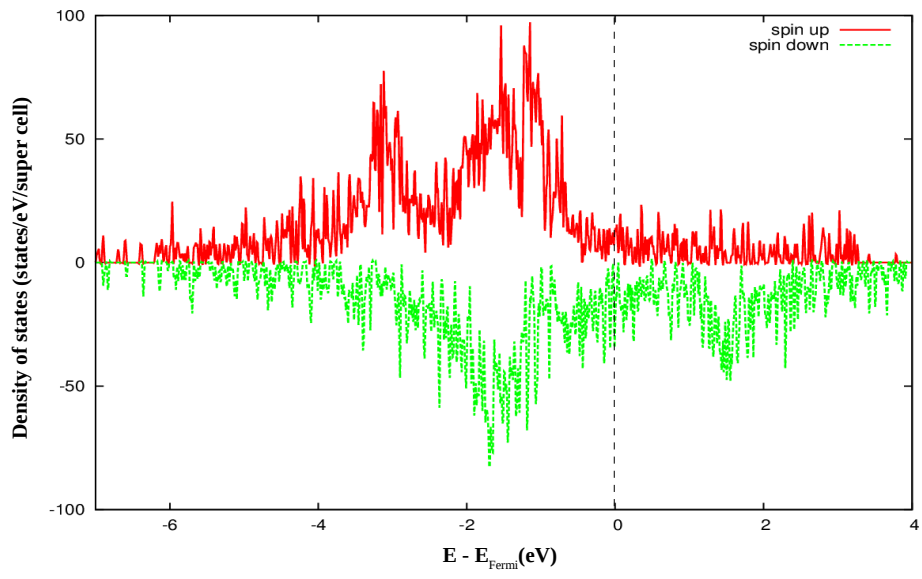


Figure 8-14. Total DOS for Ga-2Sn-Ga austenitic fourlayer system.

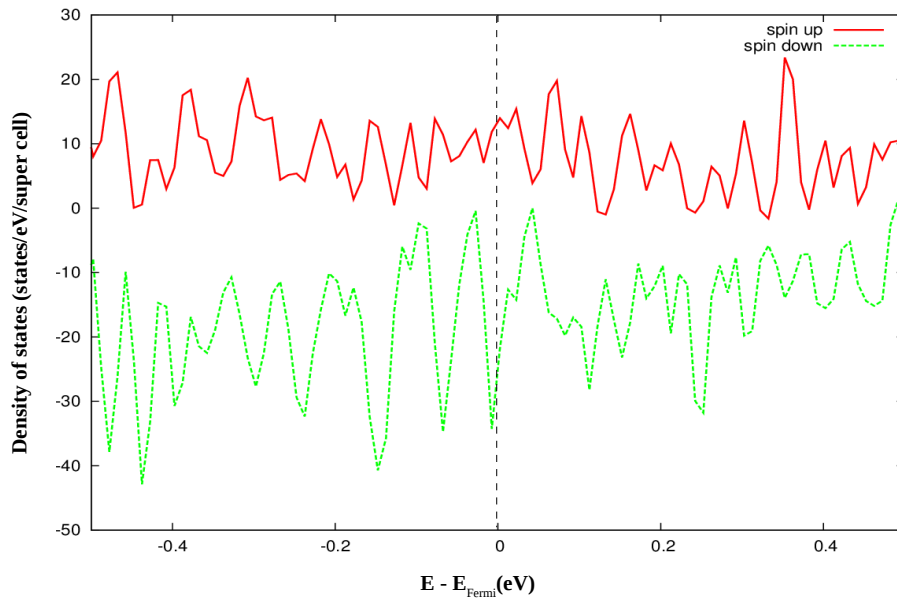


Figure 8-15. Total DOS for Ga-2Sn-Ga fourlayer system close to Fermi level.

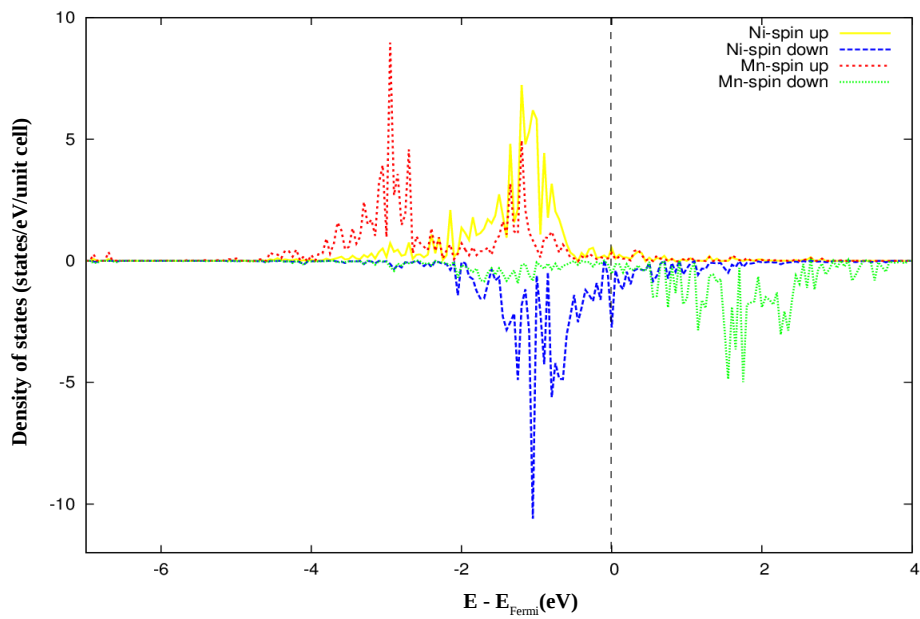


Figure 8-16. PDOS for Ni and Mn atoms in Ga-2Sn-Ga austenitic fourlayer system.

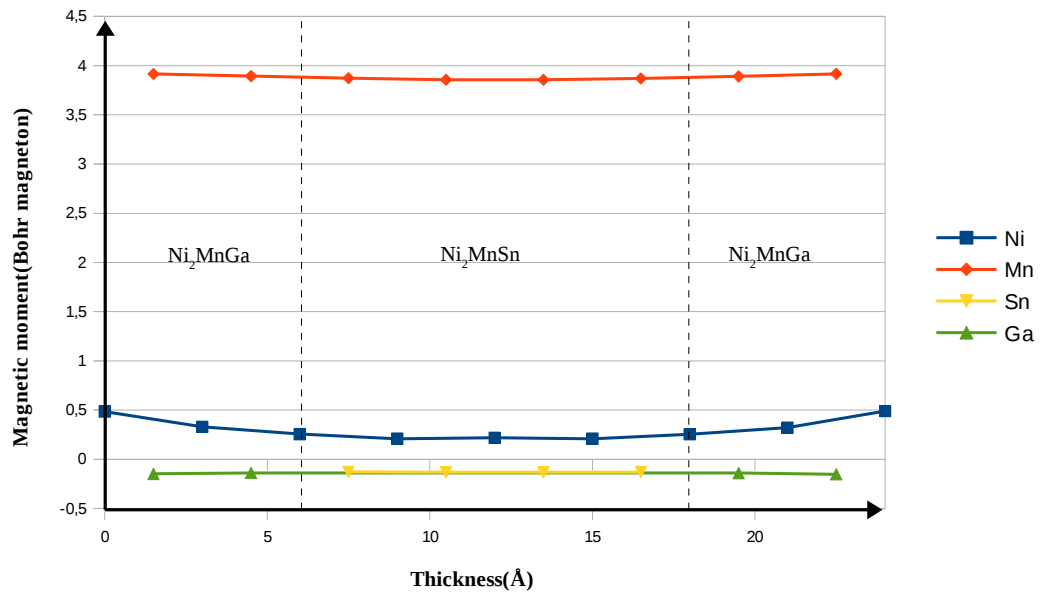


Fig. 8-17. Magnetic moments of Ni, Mn, Ga and Sn involving the austenitic fourlayer system Ga-2Sn-Ga vs. thickness of fourlayer.

5) 2Sn-Ga-2Sn fivelayer system

The five layer configuration involving a layer Ni₂MnGa sandwiched between couple layers of Ni₂MnSn are also studied. Total and partial DOS are presented in Figs. 8-18, -19 and -20. According to Fig. 8-19 like Sn-Ga-Sn system it is possible that this system shows a martensitic transformation due to majority electrons. Fig. 8-21 shows the changes of magnetic moments for elements involving in this system versus thickness of system. This system contains 42 atoms including 22 Ni, 10 Mn, 8 Sn and 2 Ga-atoms. Total magnetic moment for this system is $42.11\mu_B$ and the total energy is -3739.11 Ry.

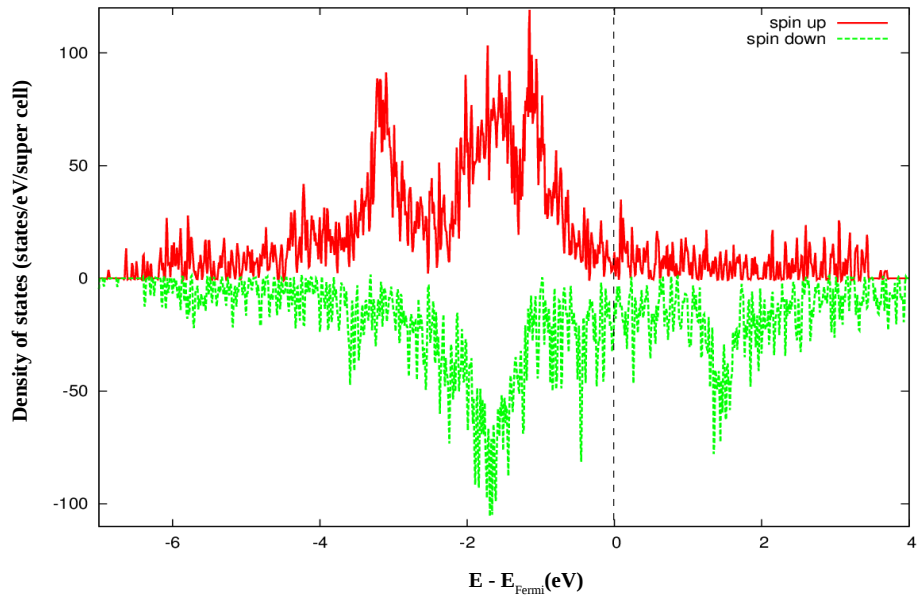


Figure 8-18. Total DOS for 2Sn-Ga-2Sn austenitic five-layer system.

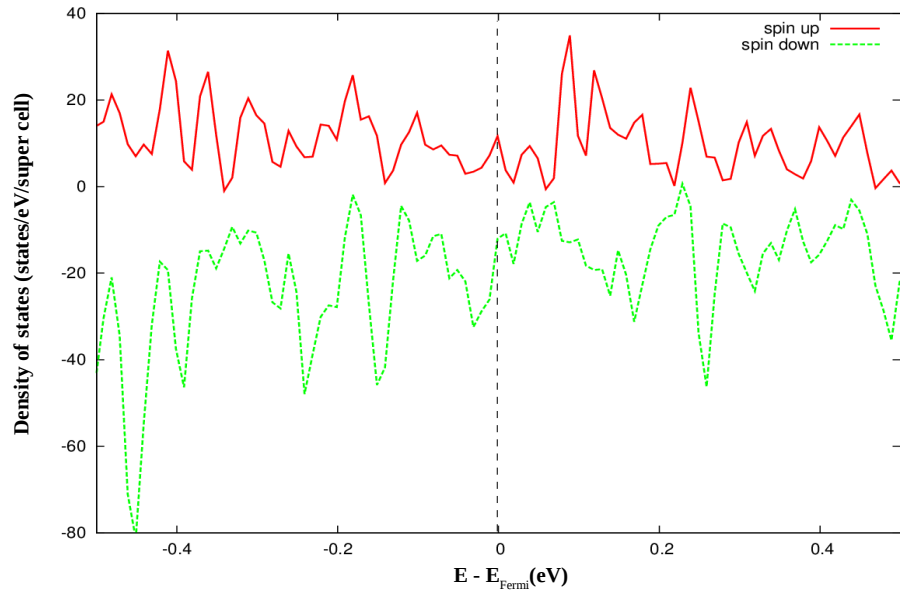


Figure 8-19. Total DOS for 2Sn-Ga-2Sn five-layer system close to Fermi level.

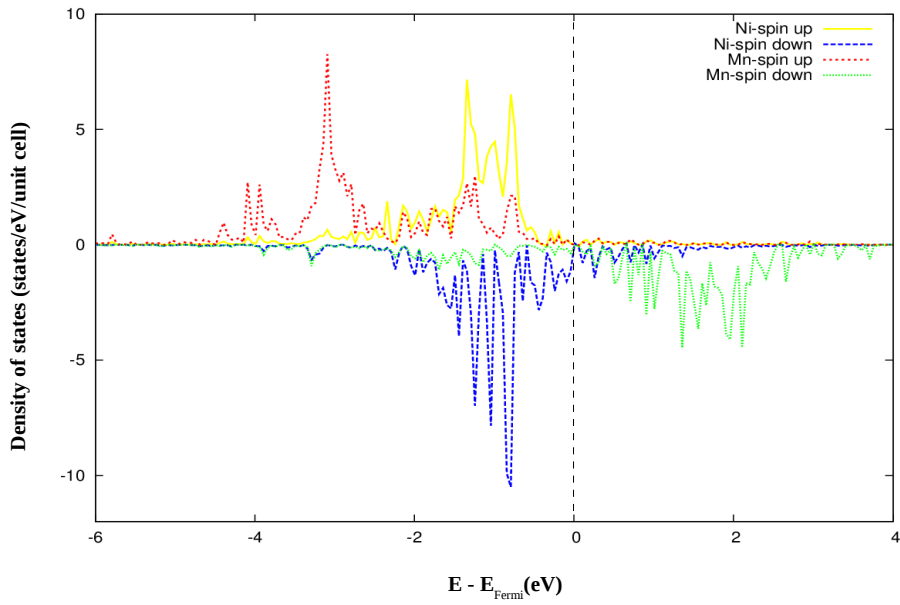


Figure 8-20. PDOS for Ni and Mn atoms in 2Sn-Ga-2Sn austenitic five-layer system.

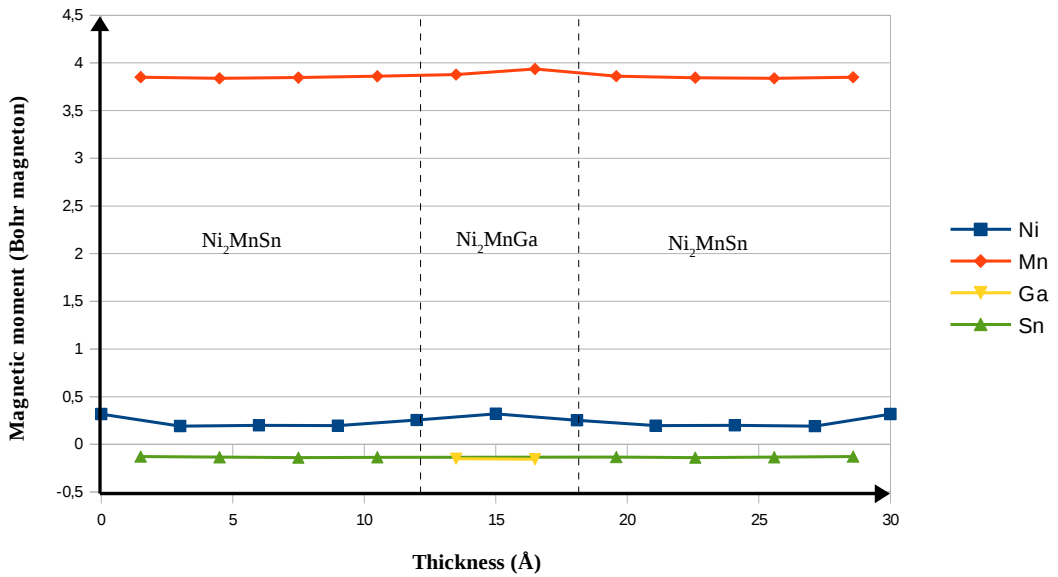


Fig. 8-21. Magnetic moments of Ni, Mn, Ga and Sn involving the austenitic five-layer system 2Sn-Ga-2Sn vs. Thickness.

6) Sn-2Ga-Sn four-layer system

Now it is interesting to study Sn-2Ga-Sn configuration as well. It involves 2 layers of Ni_2MnGa layer sandwiched between Ni_2MnSn layers. In order to do calculation a supercell as previous is used. Fig. 8-22 shows the total density of states for this configuration. Fig. 8-23 shows the total density of states close to Fermi level. Fig. 8-24 presents the partial density of states for this system. As it could be seen in Fig. 8-

23, in contrast to Ga-2Sn-Ga system, this system shows no martensitic transformation. The change of magnetic moments of individual atoms versus thickness of system is depicted in Fig. 8-25. Total magnetic moment for this configuration is $34.75\mu_B$ and total energy is -3028 Ry.

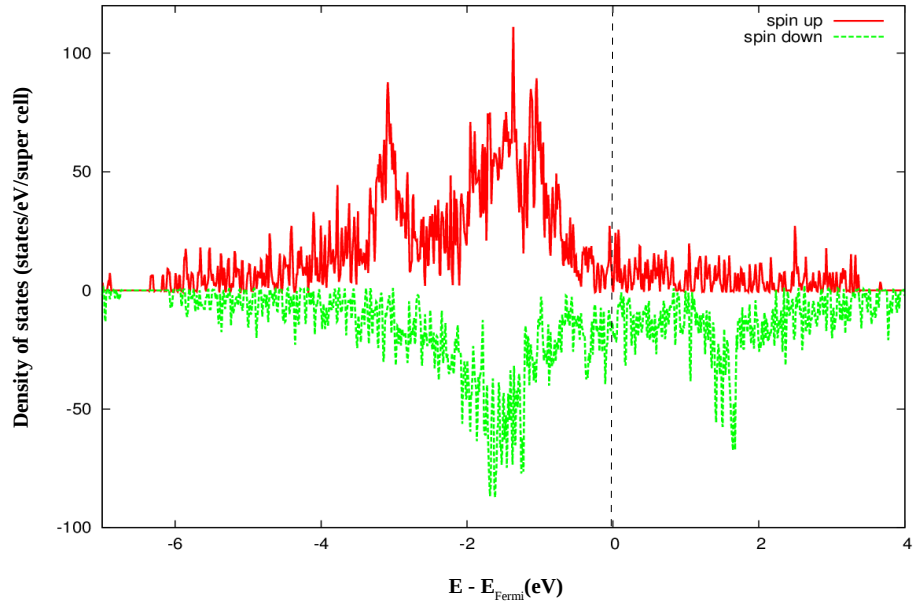


Figure 8-22. Total DOS for Sn-2Ga-Sn fourlayer austenitic system.

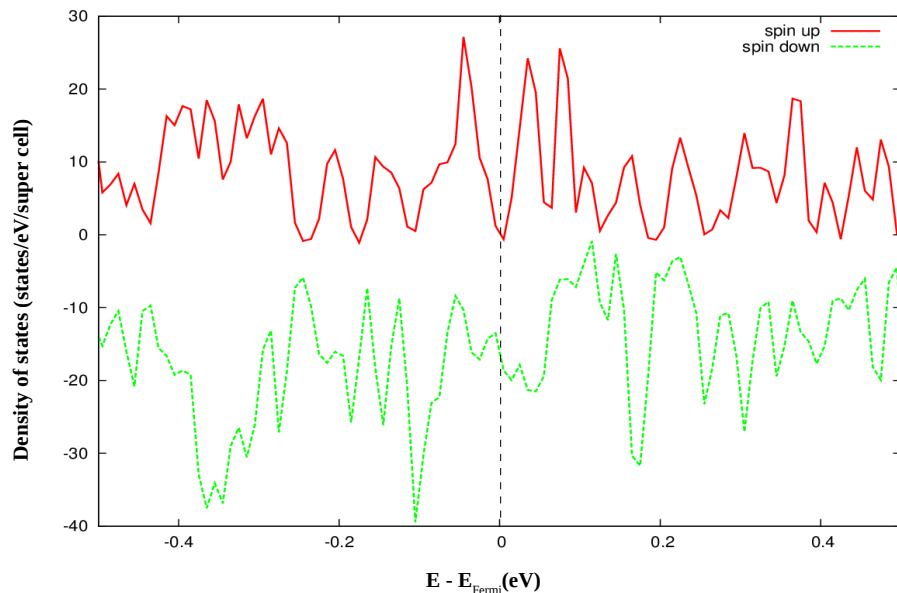


Figure 8-23. Total DOS for Sn-2Ga-Sn fourlayer system close to Fermi level.

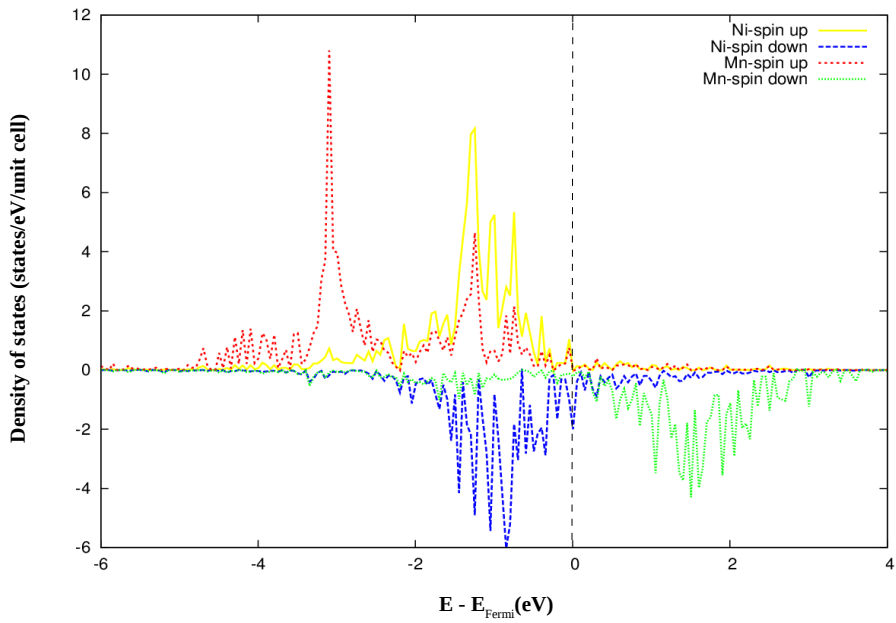


Figure 8-24. Partial DOS of Ni and Mn involving Sn-2Ga-Sn fourlayer system

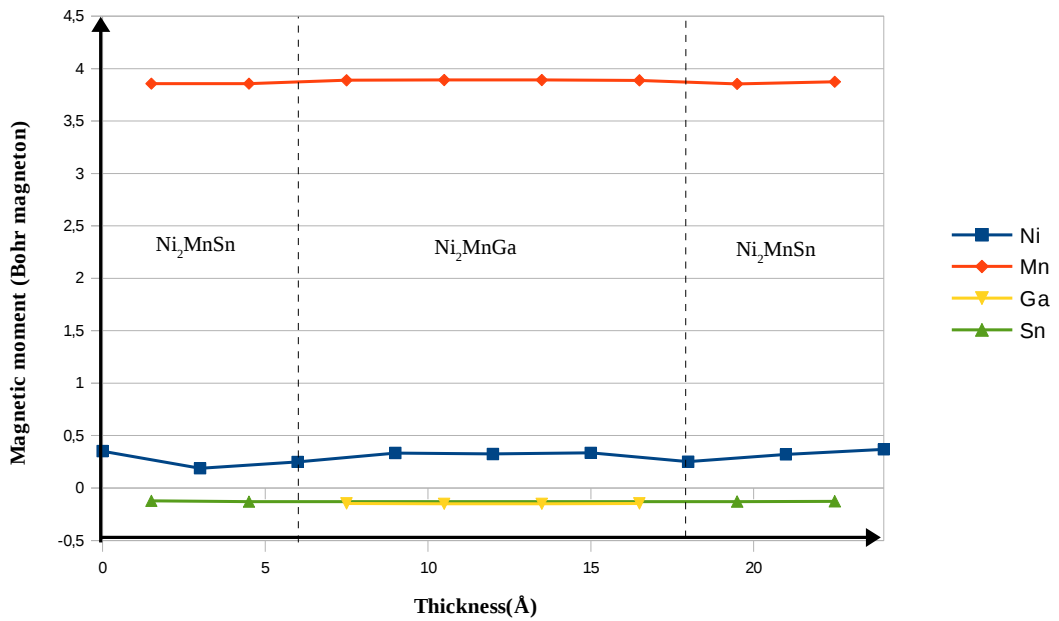


Figure 8-25. Magnetic moments of Ni, Mn, Ga and Sn involving the austenitic fourlayer system Sn-2Ga-Sn vs. thickness of fourlayer.

7) 2Ga-2Sn-2Ga sixlayer system

In the next step the case with three doubled layers will be studied. And it will be named by 2Ga-2Sn-2Ga system. Figs. 8-26 and -27 show the total density of states and Fig.8-28 presents partial density of states for Ni and Mn atoms. Fig. 8-29 shows

changes of magnetic moments for individual atom types along the thickness of system involving six 6 Å layers. To do calculation a supercell as mentioned before is assumed. As it is seen in Fig. 8-27 a peak present just after Fermi level so a martensitic transformation is eventually possible for this system. The total energy is -4458.26 Ry and system contains 50 atoms including 26 Ni, 12 Mn, 8 Ga and 4 Sn atoms. Charge density distribution is also studied and the result was the same as the 2Ga-Sn-2Ga system.

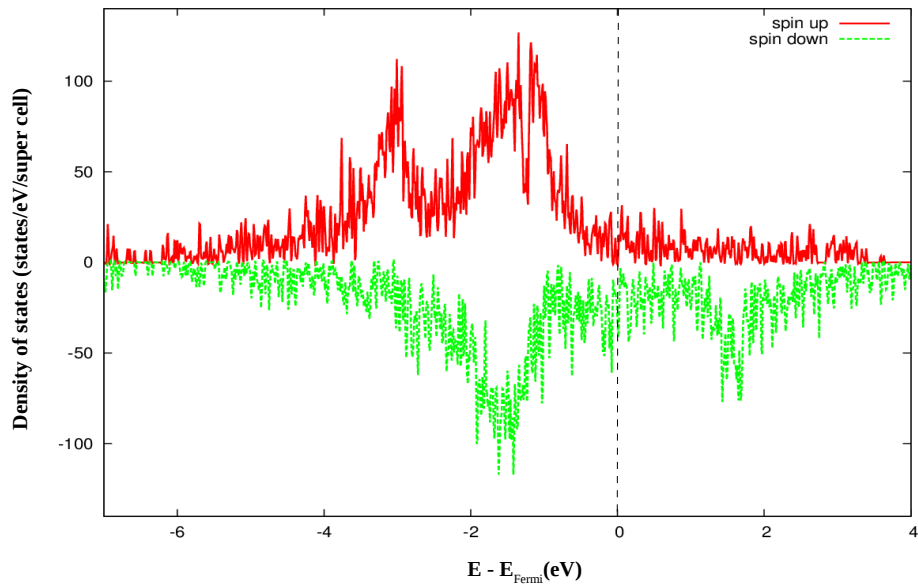


Figure 8-26. Total DOS for 2Ga-2Sn-2Ga austenitic sixlayer system.

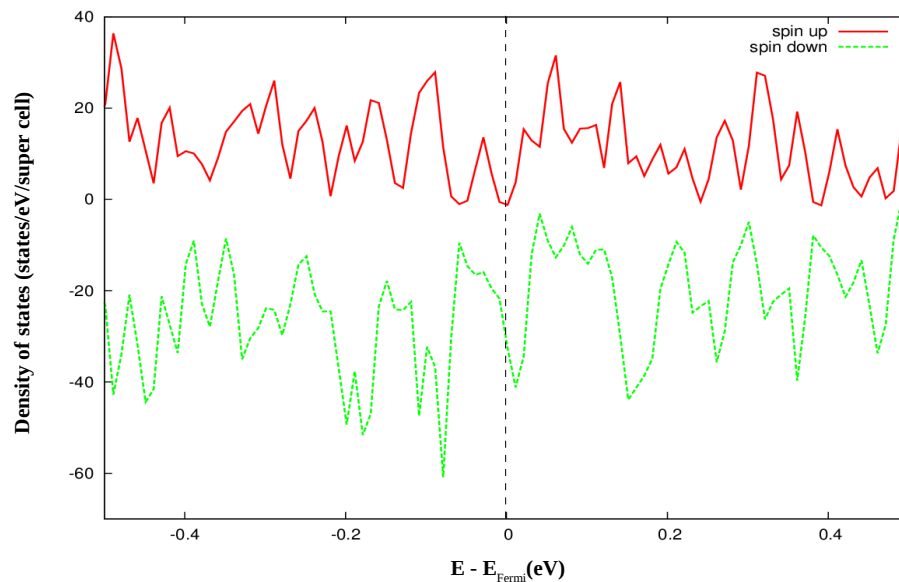


Figure 8-27. Total DOS for 2Ga-2Sn-2Ga sixlayer system close to Fermi level.

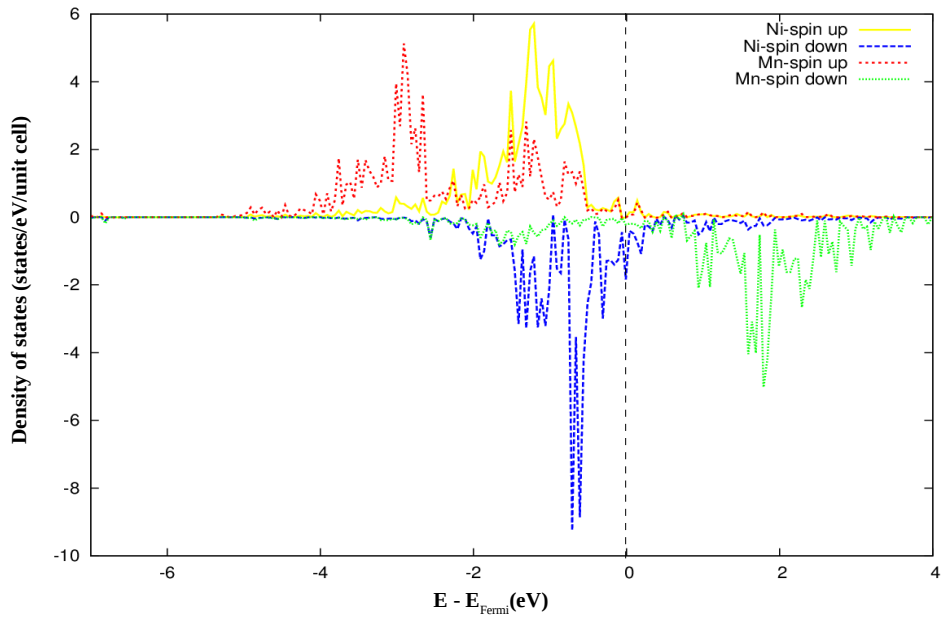


Figure 8-28. PDOS for Ni and Mn atoms in 2Ga-2Sn-2Ga.

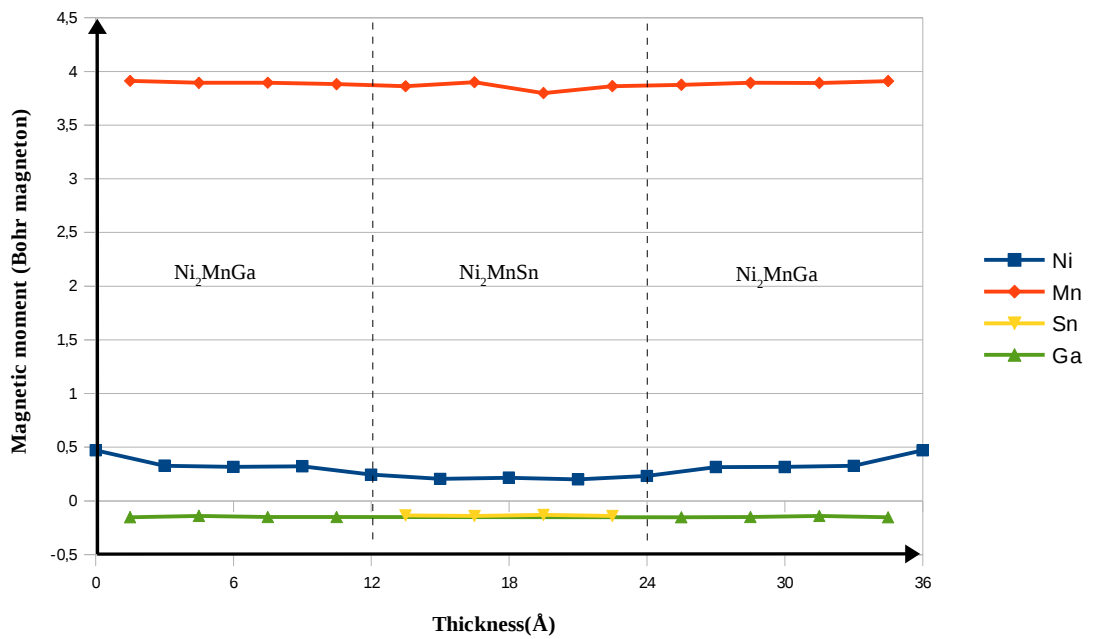


Figure 8-29. Magnetic moments of Ni, Mn, Ga and Sn involving the austenitic sixlayer system 2Ga-2Sn-2Ga vs. thickness of sixlayer.

8) Multilayer stack consisting of Ga-2Sn-Ga fourlayer system

At the end a multilayer stack with 60 Å lang making up of Ga-2Sn-Ga fourlayer system shown a strong peak at Fermi level with a vacuum of 10 Å thereon has been considered to study. The outcoming results are presented in Figs. 8-30 to -33. In comparison to simple Ga-2Sn-Ga system, total DOS also shows a martensitic transformation due to the Ni-minority d electrons. Changes the magnetic moments is presented in Fig. 8-33.

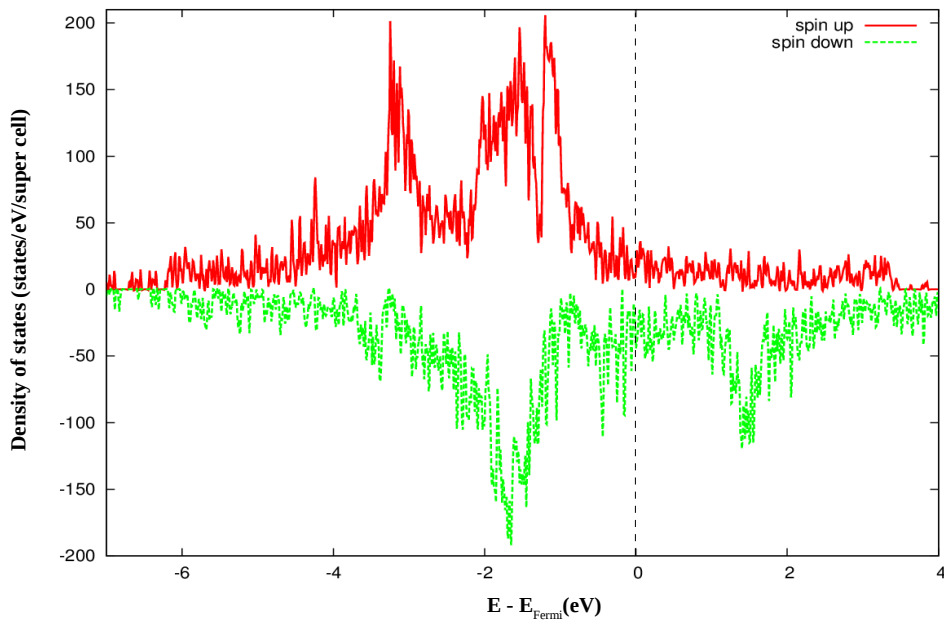


Figure 8-30. Total DOS for multilayer stack composing of Ga-2Sn-Ga austenitic fourlayer system.

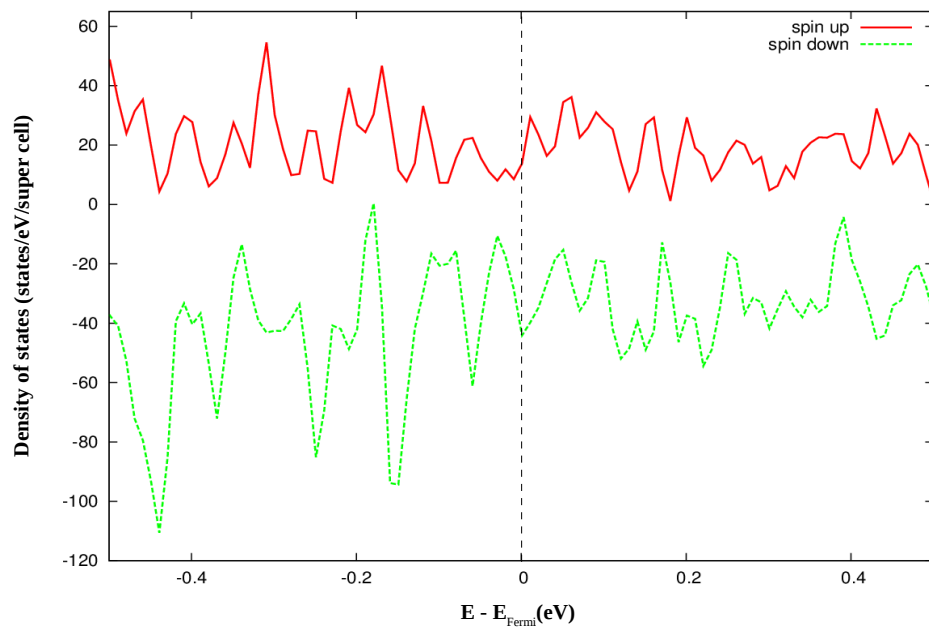


Figure 8-31. Total DOS for multilayer stack of Ga-2Sn-Ga system close to Fermi level.

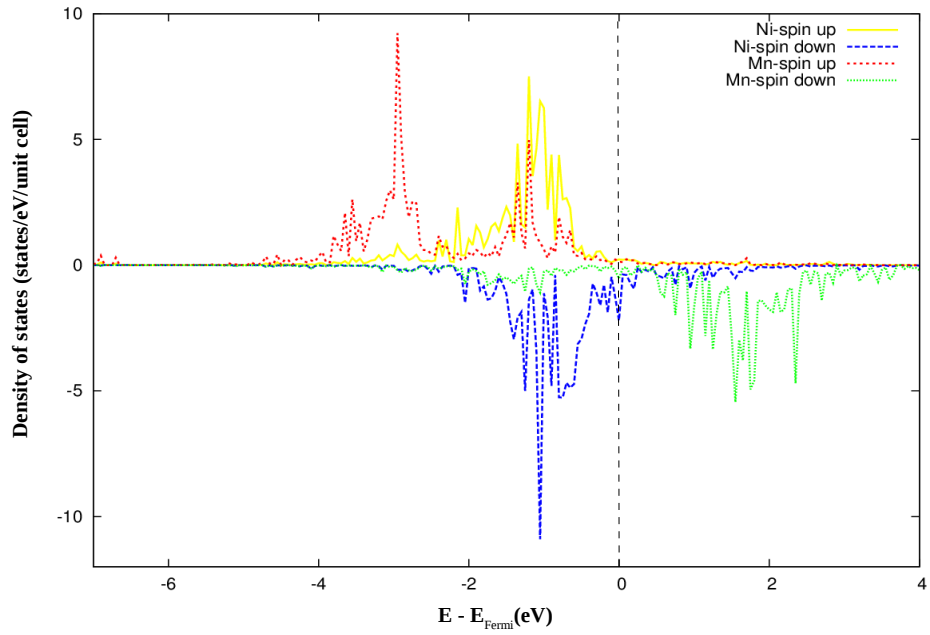


Figure 8-32. PDOS for Ni and Mn d-electrons involving the multilayer stack.

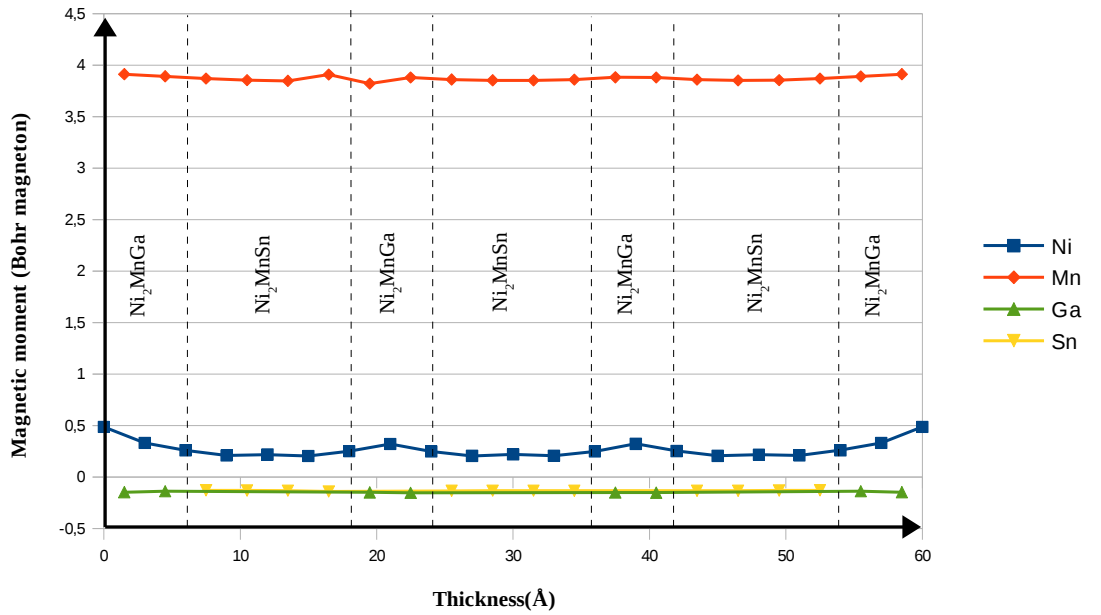


Figure 8-33. Magnetic moments of Ni, Mn, Ga and Sn involving the austenitic multilayer stack.

Conclusion- Among different configurations of Ni_2MnGa and Ni_2MnSn layers which are studied in this thesis, with regard to the graphs of total and partial density of states for systems including Ga-2Sn-Ga fourlayer, and 2Sn-Ga-2Sn fivelayer it is concluded that these systems might show martensitic transformation due to d-minority electrons of Ni atoms. Although Ga-Sn-Ga and Sn-Ga-Sn trilayers do not show a martensitic transformation occurrence, the Ga-2Sn-Ga fourlayer and 2Sn-Ga-2Sn fivelayer systems do. For all these studied configurations, magnetic moments for either element possess almost the same value; for Mn is circa $4\mu_B$, Ni magnetic moment is changing from 0.2 to $0.5\mu_B$ and Sn and Ga's magnetic moments are among -0.1 to $-0.2\mu_B$, but the Ga's magnetic moment is always higher than Sn's. A multilayer stack of Ga-2Sn-Ga also shows the martensitic transformation probability as the simple system. One interesting point in these studied configurations is that the amount of magnetic moments in interfaces do not change significantly and it could be a proof for „exchange interaction“ between atomic magnetic moments attempting to align all other atomic magnetic moments with itself. In the following for Ga-2Sn-Ga fourlayer system a comparison between magnetic moments of these elements with their bulk amounts is done the result is presented in Fig. 8-34. In this diagram the atoms involving in bulks are denoted with a star (*). As it is seen for Ga and Sn in multilayer no changes are observed but for Ni and Mn atoms involving in Ni_2MnGa of multilayer a little increase for Mn magnetic moments could be seen. For Ni atoms at the free side of configuration a little increase and in interfaces a little decrease are observable in comparison to Ni_2MnGa bulk. These results show that by multilayer configurations the magnetic moments amount could be manipulated.

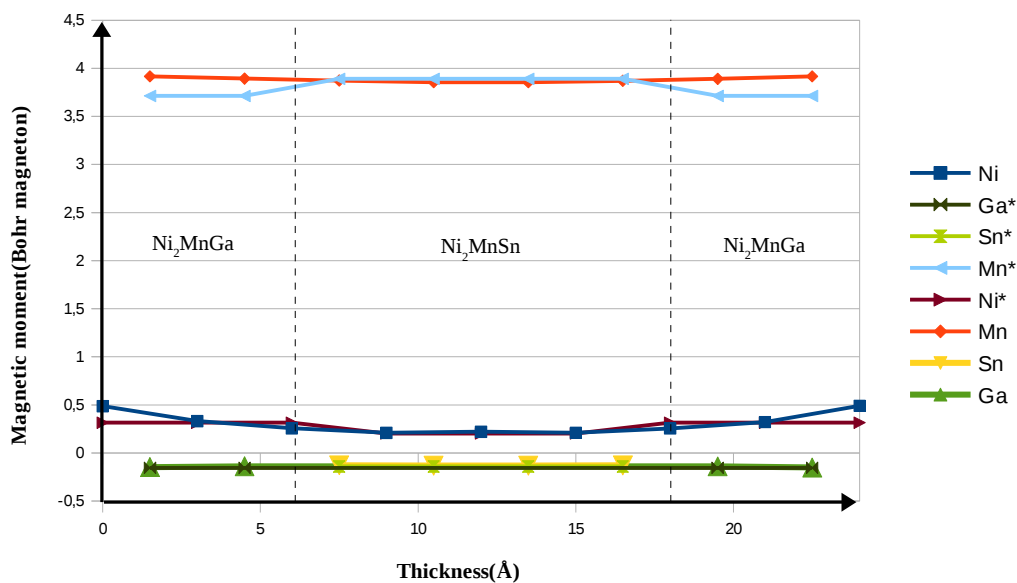


Figure 8-34. Magnetic moments of Ni, Mn, Ga and Sn involving the austenitic multilayer stack Ga-2Sn-Ga and in Ni_2MnGa and Ni_2MnSn bulks denoted with (*).

Finally to compare magnetic moments of Ni and Mn in these different configurations, once the magnetic moments of Ni and Mn for trilayers and sixlayer system are depicted in one graph and once those of four- and fivelayer systems in another one. The results are presented in Figures 8-35 to -38. In general it is seen that Ni and Mn of Ni_2MnGa possess higher magnetization than that of Ni_2MnSn , but in the cases that Ni_2MnGa comes between Ni_2MnSn layers maybe due to exchange interaction the magnetization of Ni and Mn of Ni_2MnSn in these cases increase to the level of Ni_2MnGa .

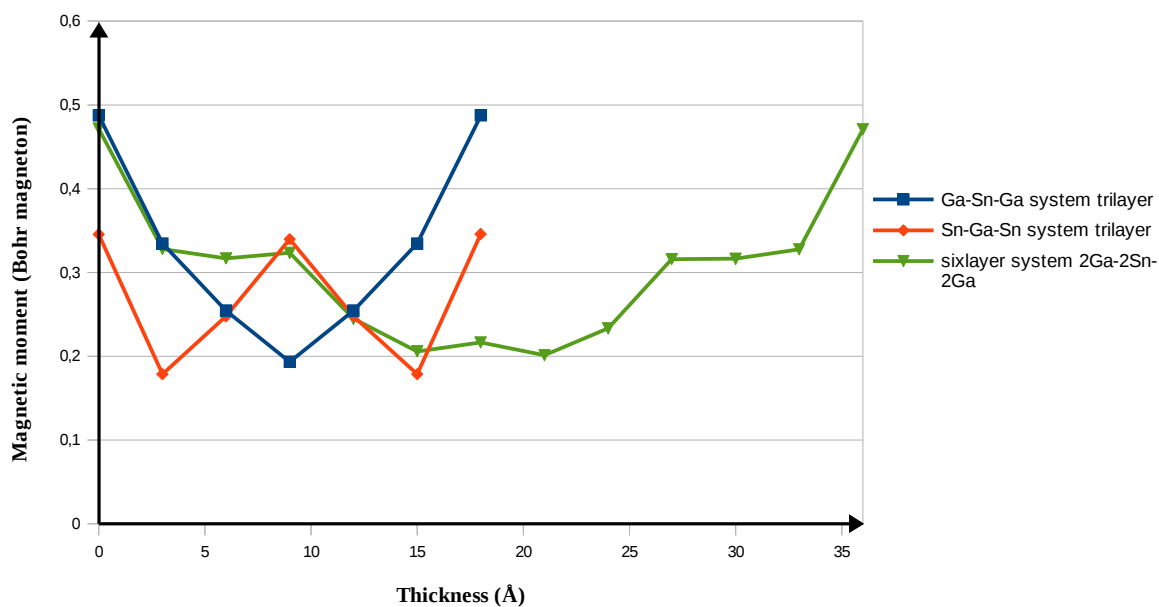


Figure 8-35. Ni magnetization changes through thickness of tri- and sixlayer austenitic systems.

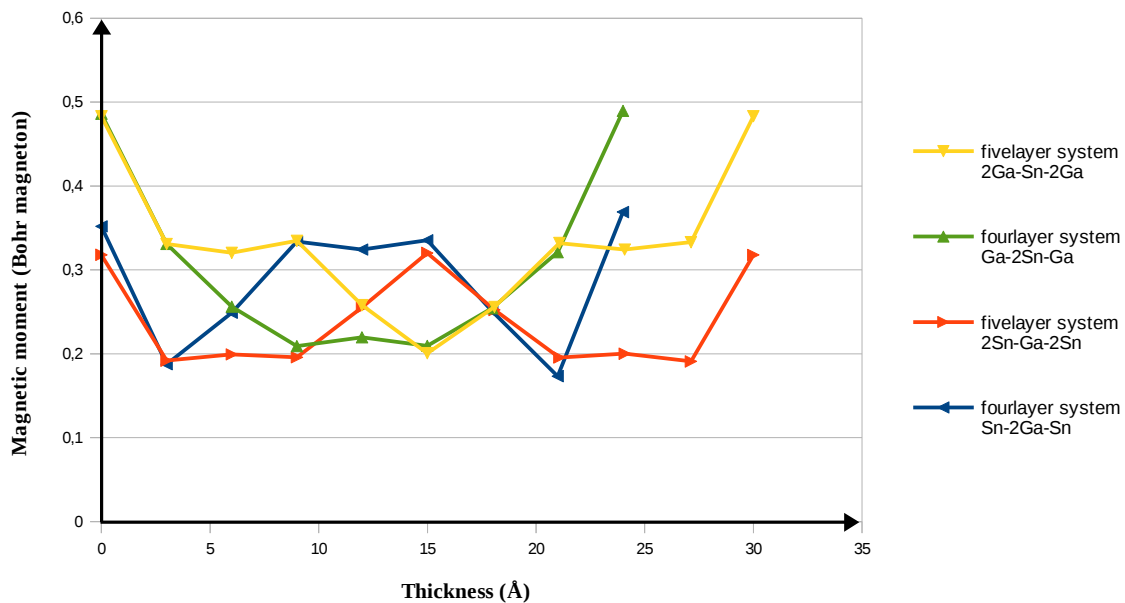


Figure 8-36. Ni magnetization changes through thickness of four- and fivelay austenitic systems. Thickness(Å)

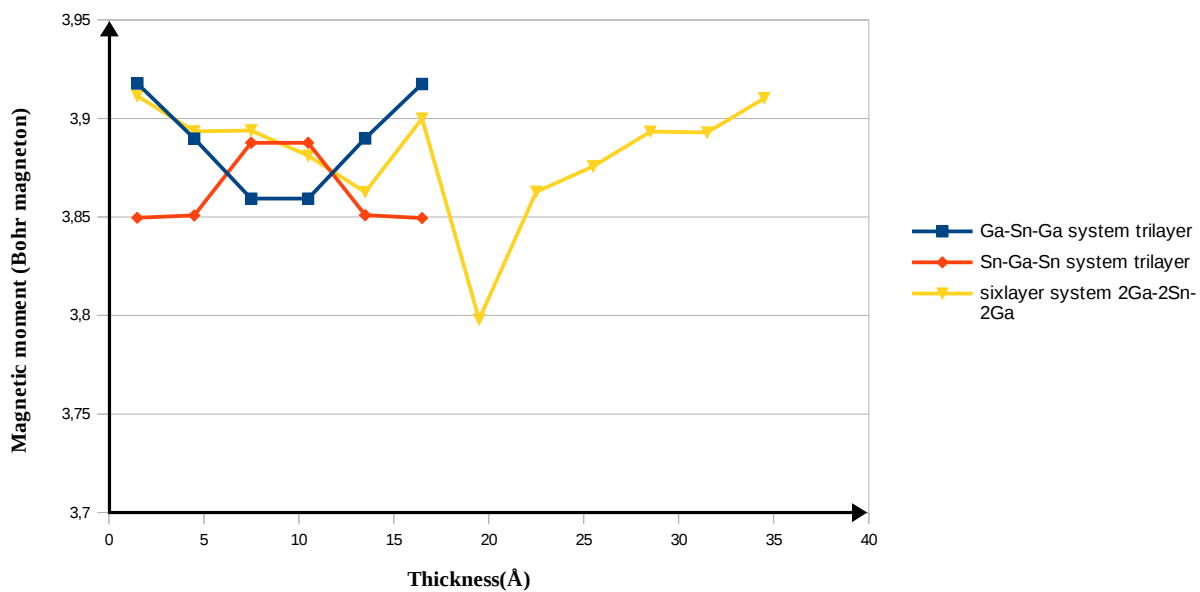


Figure 8-37. Mn magnetization changes through thickness of tri- and sixlayer austenitic systems.

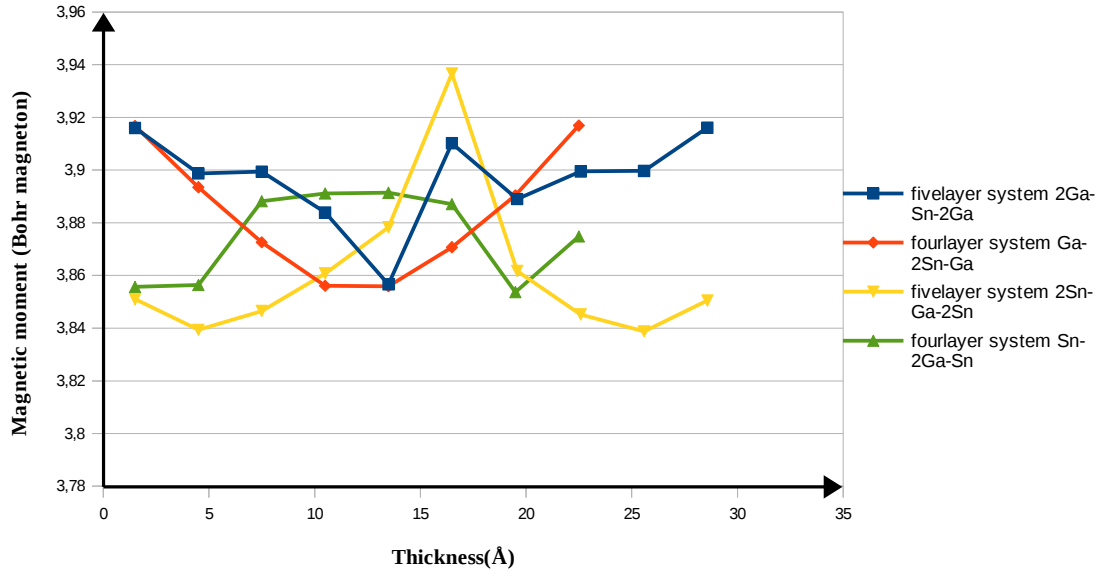


Figure 8-38. Mn magnetization changes through thickness of four- and five layer austenitic systems.

For these systems the spin polarization from Eq.(8.1) which shows spin polarisation as a ratio of difference of density of states for spin up and down electrons at the Fermi level to the sum of them is calculated and presented in Table 8-I.

$$P = \frac{D_{\uparrow}(E_F) - D_{\downarrow}(E_F)}{D_{\uparrow}(E_F) + D_{\downarrow}(E_F)} \quad (8.1)$$

Table 8-I. Total energy and spin polarization for each configuration

Configuration	total Energy(Ry)	P
Sn-Ga-Sn	-2312.86	0.28
Ga-Sn-Ga	-2314.84	0.22
Sn-2Ga-Sn	-3028.00	0.84
Ga-2Sn-Ga	-3027.97	0.22
2Ga-Sn-2Ga	-3745.13	0.45
2Sn-Ga-2Sn	-3739.11	0.016
2Ga-2Sn-2Ga	-4458.26	1.00
2Sn-2Ga-2Sn	-4454.26	0.018

Interestingly, it is seen that 2Ga-2Sn-2Ga system shows a spin polarisation about 1 which is desirable for having an optimum spin current in spintronics therefore 2Sn-2Ga-2Sn sixlayer system has been also investigated to know whether the same behavior occurs for that system or not. As it could be seen in Table 8-I, 2Sn-2Ga-2Sn sixlayer system in contrast to 2Ga-2Sn-2Ga system shows a weak spin polarization.

9 Shape Memory Effect of Non-Stoichiometric Compounds

In this section two non-stoichiometric Heusler alloys including $\text{Ni}_{54.5}\text{Mn}_{20.5}\text{Ga}_{25}$ and $\text{Ni}_{47}\text{Co}_{3.1}\text{Mn}_{36.6}\text{Sn}_{13.3}$ which could be also expressed as $\text{Ni}_{2.18}\text{Mn}_{0.82}\text{Ga}$ and $\text{Ni}_{1.92}\text{Co}_{0.09}\text{Mn}_{1.46}\text{Sn}_{0.53}$, respectively, would be studied in both austenite ($c/a=1$) and martensite ($c/a=1.25$) states.

In order to do related calculations for this section SPRKKR code by applying PBE, generalized gradient approximation, as exchange-correlation functional within the spin-polarized scalar relativistic approximation has been used.

In $\text{Ni}_{2.18}\text{Mn}_{0.82}\text{Ga}$ compound with $e/a = 7.63$, 18% of Mn sites (4b wyckoff position) are occupied by Ni atoms which would be referred in the following graphs as Ni_a and Ni atoms at Ni sites (8c wyckoff position) are specified with Ni_b. The T_M for this alloy is 335K, and $T_C = 350\text{K}$ [77].

In other studied compound, $\text{Ni}_{1.92}\text{Co}_{0.09}\text{Mn}_{1.46}\text{Sn}_{0.53}$ with $e/a = 8.07$, 6% of Ni sites (8c) and 1% of Sn sites (4a) are occupied by Co atoms which would be referred to as Co_b and Co_a, respectively. 46% of Sn sites (4a) are also filled by Mn atoms [referred to as Mn_a and Mn_b are Mn atoms at their sites (4b)], with $T_M = 300\text{K}$ and $T_C = 335\text{K}$ [78]. Figs. 9-1, -2, -3 and -4 show the total DOS of these compounds in austenite and martensite states and site projected DOS for Ni and Mn atoms. Tables 9-I, -II show the total and local magnetic moments and total energy for both austenite and martensite states. With a glance at total energies for these compounds in both states, it seems that austenite states are more stable than the martensite states.

From the graphs for austenite states for both compounds, it could be inferred that like the stoichiometric compound Ni_2MnGa , minority d-electrons of Ni atoms which are localized at their sites, in 8c wyckoff position (0.25, 0.25, 0.25), are responsible for occurring martensite states. Regarding the magnetic moment values presenting in Table 9-I and martensitic temperature, it could be concluded that $\text{Ni}_{1.92}\text{Co}_{0.09}\text{Mn}_{1.46}\text{Sn}_{0.53}$ compound could be a good choice for practical applications. Because according to [79] yielding a large magnitude of saturation magnetization difference, between the parent and martensite phases causing the driving force for the field-induced transformation is provided by the Zeeman energy difference between the two phases, *i.e.*, $E_{\text{Zeeman}} = \mu_0 \Delta M \cdot H$, where H is the strength of the applied field. Because of the large magnitude of ΔM , $\text{Ni}_{1.92}\text{Co}_{0.09}\text{Mn}_{1.46}\text{Sn}_{0.53}$ alloy is considered to be capable of generating a large magnetic driving force with a relative small magnetic field.

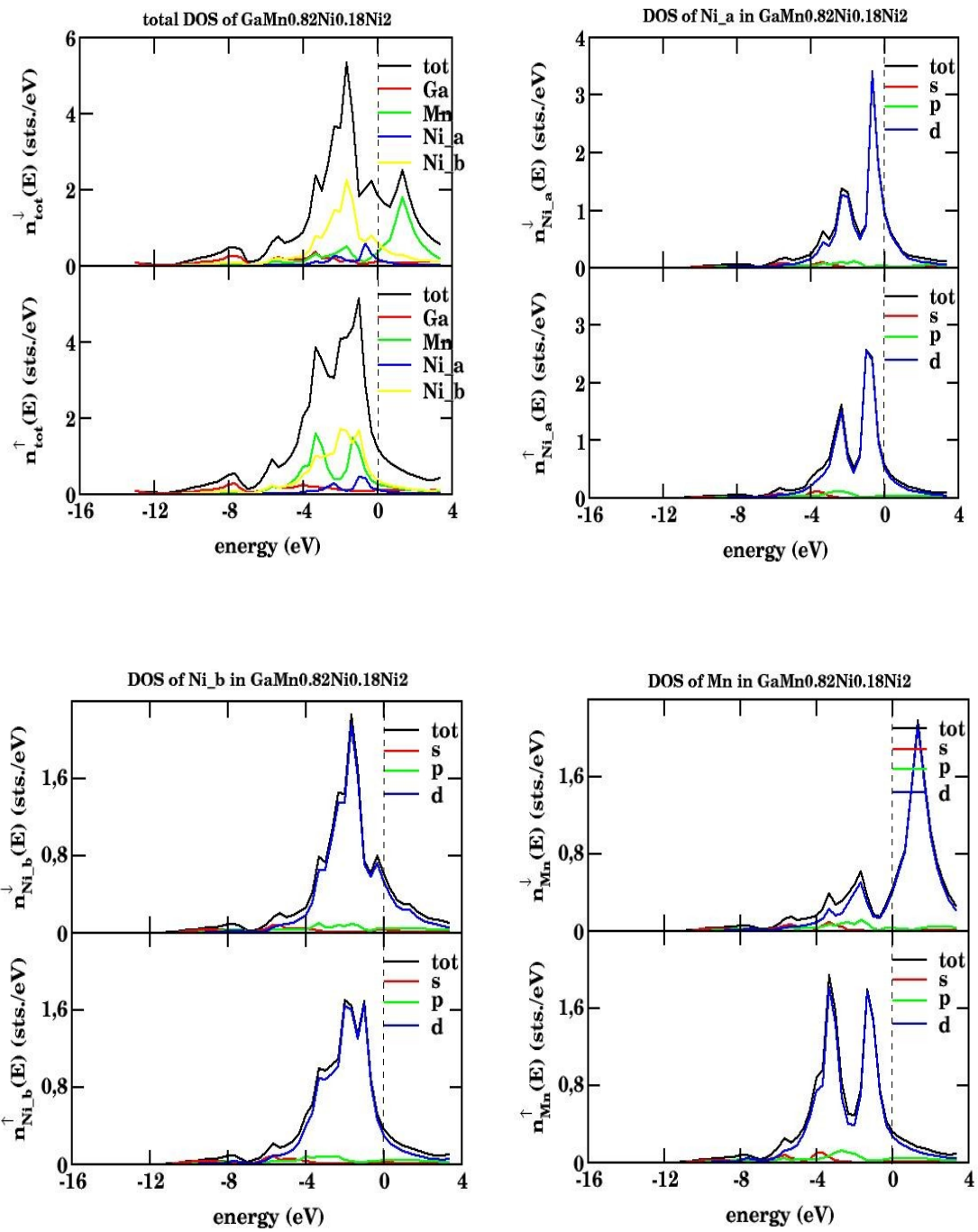


Figure 9-1. Total DOS and spin-projected DOS for Ni_a, Ni_b and Mn atoms of Ni_{2.18}Mn_{0.82}Ga in austenite state.

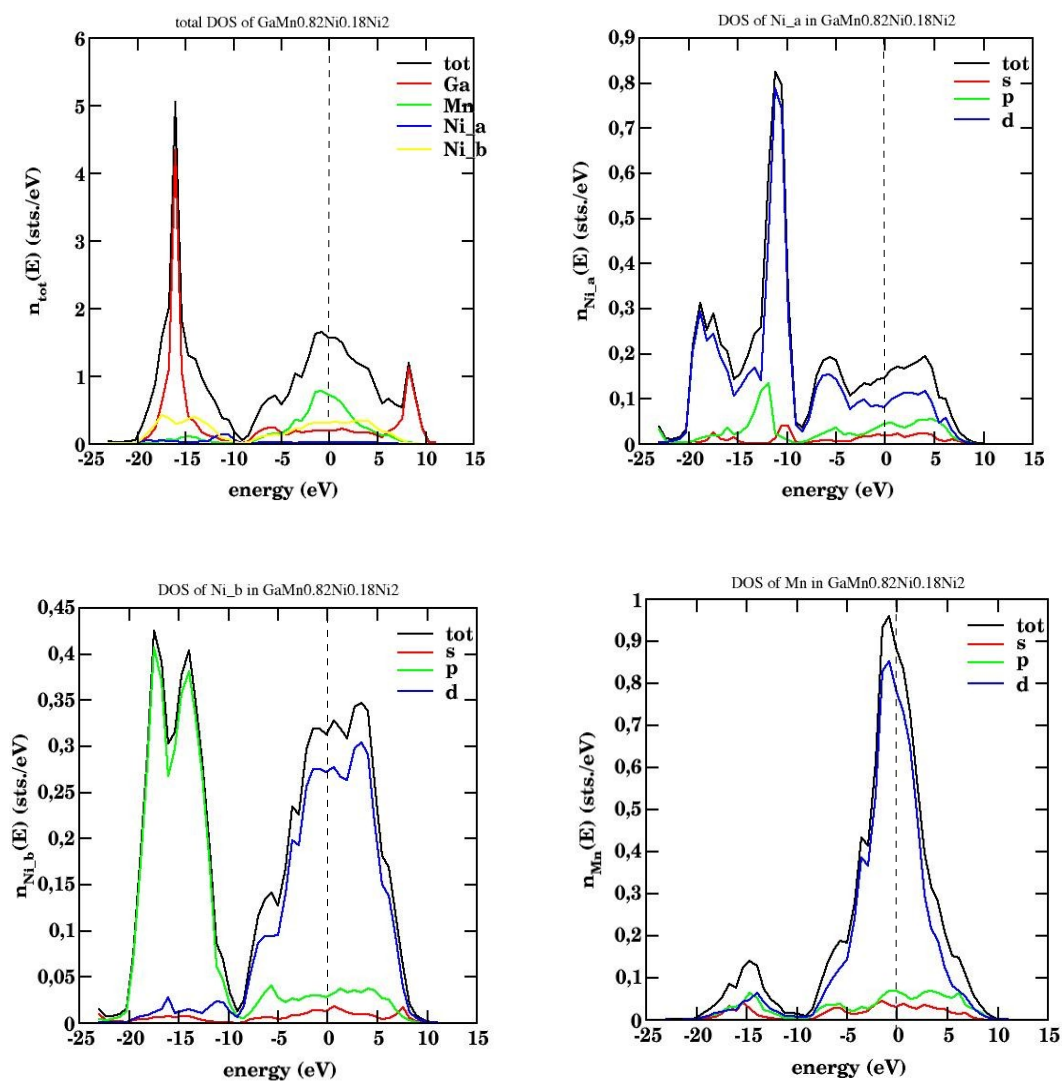


Figure 9-2. (Color online) Total DOS and spin-projected DOS for Ni_a, Ni_b and Mn atoms of Ni_{2.18}Mn_{0.82}Ga in martensite state.

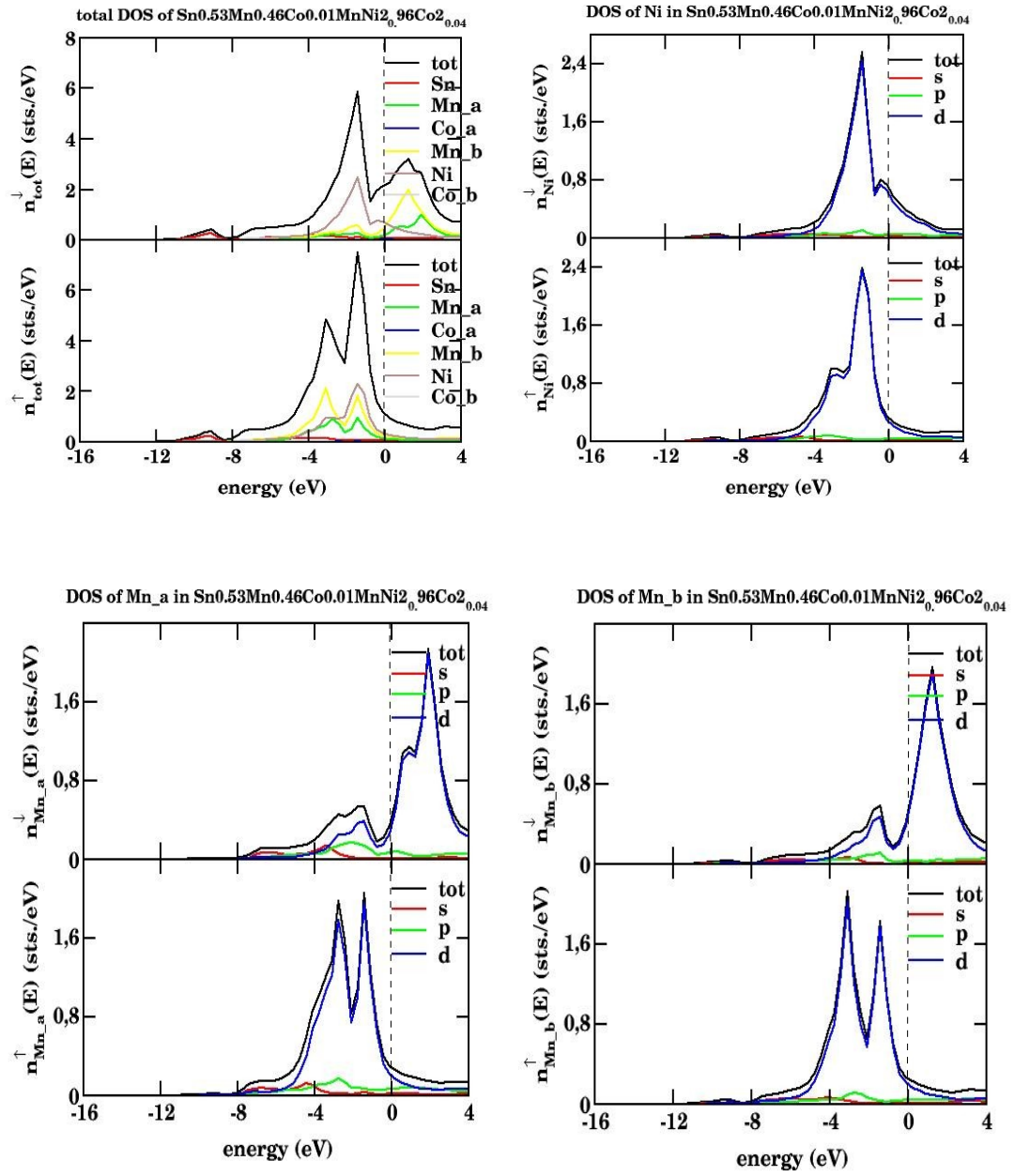


Figure 9-3. (Color online) Total DOS and spin-projected DOS for Ni, Mn_a and Mn_b atoms of $\text{Ni}_{1.92}\text{Co}_{0.09}\text{Mn}_{1.46}\text{Sn}_{0.53}$ in austenite state.

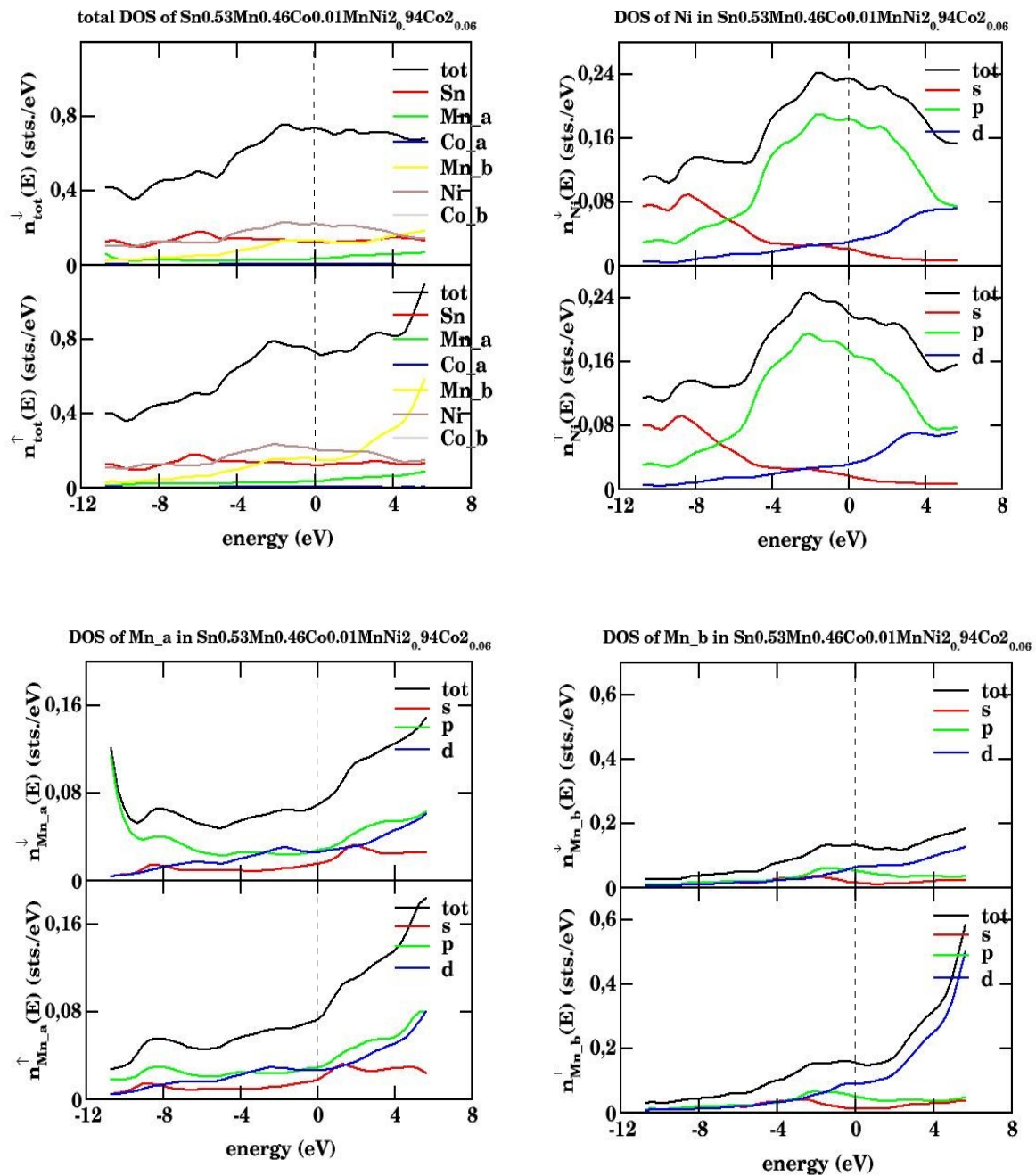


Figure 9-4. (Color online) Total DOS and spin-projected DOS for Ni, Mn_a and Mn_b atoms of $\text{Ni}_{1.92}\text{Co}_{0.09}\text{Mn}_{1.46}\text{Sn}_{0.53}$ in martensite state.

Table 9-I. Total and Local magnetic moments per site in units of μ_B

$Ni_{2.18}Mn_{0.82}Ga$		$Ni_a (4b)^1$	$Ni_b (8c)$	$Mn (4b)$	$Ga (4a)$	μ_{tot}	
$L2_1$	$c/a=1$	0.22	0.27	3.5	-0.07	3.38	
	$c/a=1.25$	0.00	0.00	0.0002	0.00	0.0002	

$Ni_{1.92}Co_{0.09}Mn_{1.46}Sn_{0.53}$		$Ni(8c)$	$Mn_a(4a)$	$Mn_b(4b)$	$Co_a(4a)$	$Co_b(8c)$	$Sn(4a)$	μ_{tot}
$L2_1$	$c/a=1$	0.42	4.00	3.69	1.95	0.21	-0.09	6.33
	$c/a=1.25$	0.07	4.30	-0.00	2.16	0.03	0.01	2.14

1. In parentheses show the wyckoff positions of atoms in austenite state

Table 9-II. Total energy (Ry)

$Ni_{2.18}Mn_{0.82}Ga$		<i>total energy (Ry)</i>
$L2_1$	$c/a=1$	-12419.39
	$c/a=1.25$	-12357.64

$Ni_{1.92}Co_{0.09}Mn_{1.46}Sn_{0.53}$		<i>total energy (Ry)</i>
$L2_1$	$c/a=1$	-16021.67
	$c/a=1.25$	-16002.68

10 Summary and Conclusions

In this work Density Of States (DOS) for different materials including cobalt in three alpha, beta and epsilon phases, Fe_2CoO_4 and Co_2FeO_4 of spinel ferrites in both normal and inverse structures, and Heusler alloys containing Ni_2MnGa and Ni_2MnSn for both stoichiometric and non-stoichiometric alloys, and diverse arrangement of Ni_2MnGa and Ni_2MnSn layers have been calculated. By study the calculated DOS for spinels it has been clear, whether they could be used as a spin filter in Multi Tunnel Junction (MTJ) systems or not. And for Heusler alloys it is shown whether they could experience a martensite transition or not which is interesting to develop novel materials for engineering applications.

For calculating DOS of Co, spin polarized DFT-based Elk Code with considering PBE (Perdew, Burke and Ernzerhof), generalized gradient approximation (GGA), as exchange-correlation functionals have been carried out, the results show a very high density of states for epsilon-Cobalt phase. The ϵ -Co phase is a very special case when compared to the other cobalt phases, exhibits different structural properties. The ϵ -Co, described by Dinega et al. [27] posses a cubic structure, space group $P4_132$, with a unit cell similar to that of β -manganese. This structure contains 20 cobalt atoms, per unit cell, divided in two types: eight atoms of type I and twelve atoms of type II. The calculated total energy per cobalt atom shows that, for GGA calculations, the α -Co phase is more stable than the β - and ϵ -Co phases. However, the structural stability should be expressed as energy per cell volume (E_x/V_x , where x is Co-phase), the calculated $\Delta E/V$ ($E_\alpha/V_\alpha - E_x/V_x$, where x is Co-phase) values show that the α -Co structure is the most stable, as expected from experimental studies. A special $20 \times 20 \times 20$ k-point mesh is considered for α - and β -Co phases while for ϵ -Co due to being time-consuming a $8 \times 8 \times 8$ k-point mesh. The obtained results are for OK.

Spinel ferrites are represented by the formula unit AB_2O_4 . Most of the spinel ferrites form cubic spinel structure belonging to space group $Fd\bar{3}m$ with oxygen anions in fcc positions and cations in the tetrahedral and octahedral coordinated interstitial lattice sites, forming the A and B sublattices. Depending upon the nature (magnetic or non-magnetic) and distribution of cations among A and B sublattices, spinel ferrites can exhibit properties of different type magnets, like: ferrimagnet, antiferromagnet and paramagnet [32]. The ferrimagnetic features are mediated by antiferromagnetic coupling between the magnetic moments at the A and B sites. For spinels containing di- and trivalent cations there are two extreme ways to distribute the A and B constituents; normal and inverse spinel. In normal spinel distribution pattern all divalent cations are located in the tetrahedrally coordinated locations and the trivalent atoms in the octahedrally ones. In inverse spinel arrangement the tetrahedral sites are filled with trivalent cations and the rest of the trivalent cations together with the divalent cations are distributed over the octahedral sites [80].

DFT-based calculations fail in describing insulating and magnetic properties; the band gap is underestimated, as the valence band maxima (VBM) lies too high and the conduction band minimum (CBM) lies too low and the magnetic moments tend to be

too small. There are alternative ways to have an estimate of the experimental band gap. One possibility is the DFT+U method; it takes orbital dependence of the Coulomb and exchange interactions into account. The position of VBM would be corrected to a large extent by adding Hubbard parameter “ U_{eff} ” to the transition metal d-orbital. To do calculations, the initial unit cells values are taken from the experimental lattice constants. Then by taking the presumed parameters into account, the best lattice value which minimizes the total energy has been chosen as lattice constant.

In planewave calculations, the main problem arises when dealing with rapidly fluctuating electron densities in the vicinity of atomic cores. One needs a very large number of plane waves in order to describe such fluctuations properly. The only possibility to save a purely planewave basis set is to discard core states. The exclusion of the core states from the direct consideration means that one has to deal in the following not with the effect of bare nuclei potentials, but rather with the potentials screened by the core electrons. This potential is more smooth and shallow than the “true” one. This simplification gives rise to a family of pseudopotential methods in contrast to the “all-electron methods” (i.e., those where all electrons, valence and core electrons, are treated in the same way).

In this thesis „Quantum-Espresso“ program by applying „ultrasoft pseudopotentials“ are utilised to do ab initio calculations. Density of states calculations for Fe_2CoO_4 and Co_2FeO_4 ferrite spinels in both normal and inverse structures - confirming the experimental results of Anna-Lena Wolff- have shown Fe_2CoO_4 as an insulator with a gap of 0.21 eV for normal and 0.24 eV for inverse structure and Co_2FeO_4 as a half-metal. For both cases the calculations also proved that inverse structure is the more stable structure regarding the total ground state energies. In these calculations magnetic moments of Co are overestimated and the band gaps are underestimated. As a result of these calculations, Co_2FeO_4 in inverse structure does have the lowest total energy is taken as a reference to determine the specific energy $\Delta E/V$ for Fe_2CoO_4 and Co_2FeO_4 in both normal and inverse structures. These calculations show that Co_2FeO_4 is merely in inverse form stable, but Fe_2CoO_4 is in both normal and inverse structure stable.

As the next step in this work Heusler alloys have been studied especially the shape memory effect in these alloys the capability of alloys to remember their original shape when they deform in the martensitic state and then heated to retransform to the austenitic state [46]. „While the shape memory effect in most of the current commercial actuator materials such as TiNi is related to a martensitic phase transformation driven by temperature [45] or applied stress [47], the magnetic control of such transformation would be faster and more efficient. Ferromagnetic Shape Memory (FSM)-alloys provide the opportunity to drive a transformation of martensitic variants by an external magnetic field. These materials can be used where high switching frequencies are needed (e.g. in actuators) or where the necessary temperature changes are not applicable (e.g. in medical devices) [47].“

In this part of work to do „first principle“ calculations, in addition to the „Q-Espresso“ code, KKR function-based program, SPRKKR, has been also used to investigate the martensitic transition behavior regarding to DOS of these structures in

both austenite (cubic structure) and martensite (tetragonal structure). Both „Q-Espresso“ and „SPRKKR“ calculations showed a martensite transformation for both Ni_2MnGa and Ni_2MnSn which for Ni_2MnGa confirms the literature, but for Ni_2MnSn not. In addition while DOS graphs resulting from Q-Espresso calculations for Ni_2MnGa in both austenite and martensite phases confirms the literature which states the martensitic modulated phase with $c/a < 1$ is the most stable phase, the results regarding energy per unit cell volume present austenite phase as the most stable phase.

Afterwards some multilayers system consisting of Ni_2MnGa and Ni_2MnSn in diverse arrangements involving tri-, four-, five- and six-layers have been studied. The most outstanding result of this part is appearing a peak due to Ni-d minority electrons at the Fermi level in total DOS of the systems that Ni_2MnGa layer is sandwiched by double Ni_2MnSn layers which are named in this thesis by 2Sn-Ga-2Sn fivelayer system and the fourlayer system involving two layers of Ni_2MnSn sandwiched by Ni_2MnGa layers (Ga-2Sn-Ga) show the possibility of occurrence of martensitic transformation due to appearing a peak at Fermi level in their total DOS graphs. Spin polarization calculation for these multilayers showed 2Ga-2Sn-2Ga system possesses spin polarisation about 1 which is desirable for having an optimum spin current in spintronics field.

Finally, two non-stoichiometric Heusler alloys including $\text{Ni}_{54.5}\text{Mn}_{20.5}\text{Ga}_{25}$ and $\text{Ni}_{47}\text{Co}_{3.1}\text{Mn}_{36.6}\text{Sn}_{13.3}$ are also studied, the result of calculations show a magnetic and structural transition for $\text{Ni}_{47}\text{Co}_{3.1}\text{Mn}_{36.6}\text{Sn}_{13.3}$ alloy which can result in effective practical application. This is in agreement with literature [78] yielding a large magnitude of saturation magnetization difference between the parent and martensite phases causing the driving force for the field-induced transformation is provided by the Zeeman energy difference between the two phases, *i.e.*, $E_{\text{Zeeman}} = \mu_0 \Delta M \cdot H$, where H is the strength of the applied field. Because of the large magnitude of ΔM resulted from the calculations it is concluded these alloys are capable of generating a large magnetic driving force with a relative small magnetic field. In contrast, martensitic transformations in many other designated ferromagnetic shape memory alloys, *e.g.*, Ni_2MnGa and Ni_2MnAl have only been found to be inducible by applying temperature or stress but not magnetic field.

11 Outlook

In the future the focus will be on simulating multilayer stack consisting of Ni_2MnGa and Ni_2MnSn Heusler alloys by applying SPRKKR program, mainly for the systems investigated experimentally which are constructed of three layers either of them with a thickness of 30 nanometer.

To be able to calculate phonon density of states, the advanced programs available to do „first principle“ calculations such as VASP (The Vienna Ab initio Simulation Package) could be utilized. In VASP central quantities like the one-electron orbitals, the electronic charge density, and the local potential are expressed in plane wave basis sets. The interactions between the electrons and ions are described using norm-conserving or ultrasoft pseudopotentials, or the projector-augmented-wave method which is an „all-electron“ method which can lead to obtain the experimental observations .

And finally a multilayer stack involving Heusler alloys and Ferrite spinels with vacant positions and defects is in prospect to be studied.

Bibliography

- [1] Y. H. Hou , Y. J. Zhao , Z. W. Liu , H. Y. Yu , X. C. Zhong , W. Q. Qiu, D. C. Zeng and L. S. Wen, "Structural, electronic and magnetic properties of partially inverse spinel CoFe_2O_4 : a first-principles study", *J. Phys. D: Applied Physics*, **43** 445003 (2010)
- [2] Y. U. Wang, "Diffraction theory of nanotwin superlattices with low symmetry phase", *Phys. Rev. B*, **74** 104109 (2006)
- [3] A. Walsh, Su-H. Wei, Y. Yan, M. M. Al-Jassim, J. A. Turner, M. Woodhouse and B. A. Parkinson, "Structural, magnetic, and electronic properties of the Co-Fe-Al oxide spinel system: Density-functional theory calculations", *Phys. Rev. B*, **76** 165119 (2007)
- [4] Z. Szotek, W. M. Temmerman, D. Ködderitzsch, A. Svane, L. Petit, and H. Winter, "Electronic structures of normal and inverse spinel ferrites from first principles", *Phys. Rev. B*, **74** 174431 (2006)
- [5] P. J. Brown, A. Y. Bargawi, J. Crangle, K-U. Neumann and K. R. A. Ziebeck, "Direct observation of a band Jahn–Teller effect in the martensitic phase transition of Ni_2MnGa ", *J. Phys.: Condens. Matter*, **11** 4715–4722 (1999)
- [6] A. T. Zayak, P. Entel, K. M. Rabe, W. A. Adeagbo, and M. Acet, "Anomalous vibrational effects in nonmagnetic and magnetic Heusler alloys", *Phys. Rev. B*, **72** 054113 (2005)
- [7] A. Behera, S. C. Mishra, "Processing and Characterization of Ni_2MnSn FSMA", *Journal of Materials and Metallurgical Engineering (JoMME)*, **2** 46-51 (2012)
- [8] A. Ayuela, J. Enkovaara, and R. M. Nieminen, "Ab initio study of tetragonal variants in Ni_2MnGa alloy", *J. Phys.: Condens. Matter*, **14** 5325–5336 (2002)
- [9] W. Koch, M. C. Holthausen , "A Chemist's Guide to Density Functional Theory", Wiley-VCH Verlag GmbH (2001)
- [10] M.A.L. Marques and E.K.U. Gross, "Time-dependant density functional theory", *Annu. Rev. Phys. Chem.* **55** 427 (2004)
- [11] J. Kohanoff, "Electronic structure calculations for solids and molecules : theory and computational methods", Cambridge Univ. Press (2006)
- [12] Richard M. Martin , "Electronic structure : basic theory and practical methods", Cambridge Univ. Press (2004)

- [13] http://en.wikipedia.org/wiki/Slater_determinant
- [14] http://www2.fkf.mpg.de/keimer/lecture/Magnetism/Magnetism_3.pdf
- [15] Alexey T. Zayak, "A first-principles investigation of the magnetic, structural and dynamical properties of Ni₂MnGa", PhD thesis, University of Duisburg-Essen (2003)
- [16] P. E. Blöchl, "Projector augmented-wave method", *Phys. Rev. B*, **50** 24 (1994)
- [17] <http://www.vasp.at/vasp-workshop/slides/pseudopotdatabase.pdf>
- [18] The Munich SPR-KKR package, version 6.3, H. Ebert et al, <http://ebert.cup.uni-muenchen.de/SPRKKR>
- [19] H. Ebert, D. Ködderitzsch, J. Minár, "Calculating condensed matter properties using the KKR-Green's function method—recent developments and applications", *Rep. Prog. Phys.* **74** 096501 (2011)
- [20] H. Ebert, "A spin polarized relativistic Korringa-Kohn-Rostoker (SPR-KKR) code for Calculating Solid State Properties", User's Guide , version 6.3 (2012)
- [21] J. Minár, "The Munich SPRKKR-program package A spin polarised relativistic Korringa-Kohn-Rostoker code for calculating solid state properties", Ludwig-Maximilians-Universität-München, http://www2.warwick.ac.uk/fac/sci/physics/news/events/kkr_greens/programme/minar.pdf
- [22] T. Huhne, C. Zecha, H. Ebert, P. H. Dederichs and R. Zeller, "Full-potential spin-polarized relativistic Korringa-Kohn-Rostoker method implemented and applied to bcc Fe, fcc Co, and fcc Ni", *Phys. Rev. B*, **58** 10236 (1998)
- [23] J. Minár, L. Chioncel, A. Perlov, H. Ebert, M. I. Katsnelson, and A. I. Lichtenstein, "Multiple-scattering formalism for correlated systems: A KKR-DMFT approach", *Phys. Rev. B*, **72** 045125 (2005)
- [24] H. Ebert et al, "The Munich SPRKKR-program package A spin polarized relativistic Korringa-Kohn-Rostoker (SPR-KKR) code for Calculating Solid State Properties", Universität München, Physikalisches Institut München, KKR07
- [25] Víctor Antonio de la Peña O'Shea, Iberio de P. R. Moreira, Alberto Roldán, and Francesc Illas, "Electronic and magnetic structure of bulk cobalt: The α , β , and ϵ -phases from density functional theory calculations", *The Journal of chemical physics*, **133** 024701 (2010)
- [26] V. F. Puntesa , K. Krishnanb and A. Paul Alivisatos, "Synthesis of colloidal cobalt nanoparticles with controlled size and shapes", *Topics in Catalysis*, **19** 2

(2002)

[27] D. P. Dinega, "Synthesis and characterization of cobalt nanocrystals", PhD thesis, Massachusetts Institute of Technology (2001)

[28] D. P. Dinega and M. G. Bawendi, "A Solution-Phase Chemical Approach to a New Crystal Structure of Cobalt", *Angew. Chem. Int. Ed.* **38**, 1788 (1999)

[29] <http://elk.sourceforge.net/>

[30] C. Kittel, *Introduction to Solid State Physics* (Wiley, New York, 2005)

[31] Landolt-Börnstein Numerical Data and Functional Relationships in Science and Technology, edited by K. H. Hellwege and O. Madelung (Springer, New York, 1986), Vol. **19/a**.

[32] I. Panneer Muthuselvam and R. N. Bhowmik, "Structural phase stability and Magnetism in Co_2FeO_4 spinel oxide", Pondicherry University, <http://arxiv.org/pdf/0810.0449.pdf>

[33] A. Walsh, S-H. Wei, Y. Yan, M. M. Al-Jassim, and J. A. Turner, "Structural, magnetic, and electronic properties of the Co-Fe-Al oxide spinel system: Density-functional theory calculations", *Phys. Rev. B*, **76** 165119 (2007)

[34] "P. Giannozzi et al., "QUANTUM ESPRESSO: a modular and open-source software project for quantum simulations of materials", *J. Phys.:Condens. Matter*, **21** 395502 (2009); URL <http://www.quantum-espresso.org>"

[35] P. James, O. Eriksson, B. Johansson and I. A. Abrikosov, " Calculated magnetic properties of binary alloys between Fe, Co, Ni, and Cu", *Phys. Rev. B*, **59** 1 (1999-I)

[36] F. Tran, P. Blaha and K. Schwarz, "Band gap calculations with Becke-Johnson exchange potential", *J. Phys.: Condens. Matter* **19**, 196208 (2007)

[37] D. Koller, F. Tran, and P. Blaha, "Merits and limits of the modified Becke-Johnson exchange potential", *Phys. Rev. B*, **83** 195134 (2011)

[38] T. R. Paudel, A. Zakutayev, S. Lany, M. d’Avezac, and Alex Zunger, "Doping Rules and Doping Prototypes in A_2BO_4 Spinel Oxides", *Adv. Funct. Mater.*, **21** 4493–4501 (2011)

[39] V. N. Antonov, B. N. Harmon, and A. N. Yaresko, "Electronic structure and x-ray magnetic circular dichroism in Fe_3O_4 and Mn-, Co-, or Ni-substituted Fe_3O_4 ", *Phys. Rev. B*, **67** 024417 (2003)

[40] P. Blaha, K. Schwarz, P. Novák, "Electric Field Gradients in Cuprates: Does

LDA+U Give the Correct Charge Distribution?", *International Journal of Quantum Chemistry*, **101** 550–556 (2005)

[41] A. Jain, S.P. Ong, G. Hautier, W. Chen, W. D. Richards, S. Dacek, S. Cholia, D. Gunter, D. Skinner, G. Ceder, K. A. Persson, "The Materials Project: A materials genome approach to accelerating materials innovation", *Applied Physics Letters Materials*, **1** 011002 (2013) [doi:10.1063/1.4812323](https://doi.org/10.1063/1.4812323)

[42] S. P. Ong, L. Wang, B. Kang, G. Ceder, "Li-Fe-P-O₂ Phase Diagram from First Principles Calculations", *Chemistry of Materials*, **20** 1798–1807 (2008) [doi:10.1021/cm702327g](https://doi.org/10.1021/cm702327g)

[43] A. Jain, G. Hautier, S. P. Ong, C. Moore, C. Fischer, K. Persson, G. Ceder. "Formation enthalpies by mixing GGA and GGA+U calculations", *Phys. Rev. B*, **84** 045115 (2011) [doi:10.1103/PhysRevB.84.045115](https://doi.org/10.1103/PhysRevB.84.045115)

[44] http://www.geocities.jp/ohba_lab_ob_page/structure2.html

[45] A. Ayuela, J. Enkovaara, K. Ullakko and R. M. Nieminen, "Structural properties of magnetic Heusler alloys", *J. Phys.: Condens. Matter*, **11** 2017–2026 (1999)

[46] T. Krenke, M. Acet, E. F. Wassermann, Xavier Moya, Lluís Mañosa, and Antoni Planes, "Martensitic transitions and the nature of ferromagnetism in the austenitic and martensitic states of Ni- Mn- Sn alloys", *Phys. Rev. B*, **72** 014412 (2005)

[47] T. Buesgen, J. Feydt, R. Hassdorf, S. Thienhaus, M. Moske, M. Boese, A. Zayak, and P. Entel, "Ab initio calculations of structure and lattice dynamics in Ni-Mn-Al shape memory alloys", *Phys. Rev. B*, **70** 014111 (2004)

[48] R. Vishnoi, R. Singhal, and D. Kaur, "Thickness dependent phase transformation of magnetron-sputtered Ni–Mn–Sn ferromagnetic shape memory alloy thin films", *Journal of Nanoparticle Research*, **13** 3975–3990 (2011)

[49] Antoni Planes, " Controlling the martensitic transition in Heusler shape-memory materials", *Phys. Rev. Lett.*, **104** 176401 (2010)

[50] L. Righi, F. Albertini, S. Fabbri, A. Paoluzi, "Crystal Structures of Modulated Martensitic Phases of FSM Heusler Alloys", *Materials Science Forum*, **684** 105-116 (2011)

[51] J. Pons, V. A. Chernenko, R. Santamarta, and E. Cesari, "Crystal structure of martensitic phases in Ni-Mn-Ga shape memory alloys", *Acta mater.*, **48** 3027-3038 (2000)

[52] V. V. Khovaylo, T. Kanomata, T. Tanaka, M. Nakashima, Y. Amako, R. Kainuma, R. Y. Umetsu, H. Morito, H. Miki, "Magnetic properties of Ni₅₀Mn_{34.8}In_{15.2}

probed by Mössbauer spectroscopy", *Phys. Rev. B*, **80** 144409 (2009)

[53] A. Planes, L. Manosa, and Mehmet Acet, "Magnetocaloric effect and its relation to shape-memory properties in ferromagnetic Heusler alloys", *J. Phys.: Condens. Matter*, **21** 233201 (2009)

[54] P. Müllner, V.A. Chernenko and G. Kostorz, "A microscopic approach to the magnetic-field-induced deformation of martensite (magnetoplasticity)", *J. Magn. Mater.*, **267** 325-334 (2003)

[55] V.A.Chernenko, P.Müllner, M.Wollgarten, J. Pons and G.Kostorz, "Large cyclic deformation of a Ni-Mn-Ga shape memory alloy induced by magnetic fields", *J. Appl. Phys.*, **92** 6708 (2002)

[56] D. S. Liberman, T. A. Read and M. S. Wechsler, "Graphical Analysis of Diffusionless Phase Changes—the Cubic to Twinned Orthorhombic Transformation", *J. Appl. Phys.*, **28** 532 (1957)

[57] S. Kaufmann, R. Niemann, T. Thersleff, U. K. Rößler, O. Heczko, J. Buschbeck, B. Holzapfel, L. Schultz, and S. Fähler, "Modulated martensite: why it forms and why it deforms easily", *New Journal of Physics*, **13** 053029 (2011)

[58] V. A. Chernenko and V. A. L'vov, "Magnetoelastic Nature of Ferromagnetic Shape Memory Effect", *Materials Science Forum*, **583** 1-20 (2008)

[59] S. Kaufmann, U. K. Rößler, O. Heczko, M. Wuttig, J. Buschbeck, L. Schultz, and S. Fähler, "Adaptive Modulations of Martensites", *Phys. Rev. Lett.*, **104** 145702 (2010)

[60] V. Kohn and S. Müller, "Branching of twins near an austenite-twinned-martensite interface", *Philos. Mag. A*, **66** 697-715 (1992)

[61] R. C. O'Handley, S. J. Murray, M. Marioni, H. Nembach, and S. M. Allen, "Phenomenology of giant magnetic-field-induced strain in ferromagnetic shape-memory materials", *J. Appl. Phys.*, **87** 9 (2000)

[62] G. A. Gehring, K. A. Gehring, "Co-operative Jahn-Teller effects", *Rep. Prog. Phys.*, **38** 1-89 (1975)

[63] M. C. M. O'Brien and C. C. Chancey, "The Jahn-Teller effect: An introduction and current review", *Am. J. Phys.*, **61** 688 (1993)

[64] P. J. Brown, A. Y. Bargawi, J. Crangle, K-U. Neumann, and K. R. A. Ziebeck, "Direct observation of a band Jahn-Teller effect in the martensitic phase transition of Ni₂MnGa", *J. Phys.: Condens. Matter*, **11** 4715-4722 (1999)

- [65] <http://wwwchem.uwimona.edu.jm/courses/CFT.html>
- [66] I. Galanakis, P. H. Dederichs, and N. Papanikolaou, "Slater-Pauling behavior and origin of the half-metallicity of the full-Heusler alloys", *Phys. Rev. B*, **66** 174429 (2002)
- [67] I. Galanakis, Ph. Mavropoulos, and P. H. Dederichs, "Electronic structure and Slater-Pauling behaviour in half-metallic Heusler alloys calculated from first principles", *J. Phys. D: Appl. Phys.*, **39** 765–775 (2006)
- [68] S. Skaftouros, K. Ozdogan, E. Sasioglu, and I. Galanakis, "Generalized Slater-Pauling rule for the inverse Heusler compounds", *Phys. Rev. B*, **87** 024420 (2013)
- [69] P. Entel, V. D. Buchelnikov, V. V. Khovailo, A. T. Zayak, W. A. Adeagbo, M. E. Gruner, H. C. Herper, and E. F. Wassermann, "Modelling the phase diagram of magnetic shape memory Heusler alloys", *J. Phys. D: Appl. Phys.*, **39** 865–889 (2006)
- [70] P. Entel, V. D. Buchelnikov, M. E. Gruner, A. Hucht, V. V. Khovailo, S. K. Nayak, A. T. Zayak, "Shape Memory Alloys: A Summary of Recent Achievements", *Materials Science Forum*, **583** 21-41 (2008)
- [71] N. Lanska, O. Söderberg, A. Sozinov, Y. Ge, K. Ullakko et al., "Composition and temperature dependence of the crystal structure of Ni–Mn–Ga alloys", *J. Appl. Phys.*, **95** 8074 (2004)
- [72] X. Jin, M. Marioni, D. Bono, S. M. Allen, R. C. O’Handley, and T. Y. Hsu, "Empirical mapping of Ni–Mn–Ga properties with composition and valence electron concentration", *J. Appl. Phys.*, **91** 10 (2002)
- [73] P. J. Brown, A. Y. Bengali, J. Crangle, K-U. Neuman, and K. R. A. Ziebeck, *J. Phys.: Condens.Matter*, **11** 4715 (1999)
- [74] P. J. Webster, "Heusler alloys", *Contemp. Phys.*, **10** 559 (1969)
- [75] H. C. Xuan, Y. X. Zheng, S. C. Ma, Q. Q. Cao, D. H. Wang et al., "The martensitic transformation, magnetocaloric effect, and magnetoresistance in high-Mn content $\text{Mn}_{47+x}\text{Ni}_{43-x}\text{Sn}_{10}$ ferromagnetic shape memory alloys", *J. Appl. Phys.*, **108** 103920 (2010)
- [76] A.kokalj, *Comp. Mater. Sci.*, **28** 155 (2003) code available from <http://www.xcrysden.org/>
- [77] M. Khan, S. Stadler, J. Craig, J. Mitchell, and N. Ali, "The Overlap of First- and Second-Order Phase Transitions and Related Magnetic Entropy Changes in $\text{Ni}_{2+x}\text{Mn}_{1-x}\text{Ga}$ Heusler Alloys", *IEEE transactions on magnetics*, **42** 10 (2006)

- [78] T. Krenke, E. Duman, M. Acet, X. Moya, L. Mañosa et al., "Effect of Co and Fe on the inverse magnetocaloric properties of Ni-Mn-Sn", *J. Appl. Phys.*, **102** 033903 (2007)
- [79] Z. H. Liu, Z. G. Wu, X. Q. Ma, W. H. Wang, Y. Liu, and G. H. Wu, "Large magnetization change and magnetoresistance associated with martensitic transformation in $\text{Mn}_2\text{Ni}_{1.36}\text{Sn}_{0.32}\text{Co}_{0.32}$ alloy", *J. Appl. Phys.*, **110** 013916 (2011)
- [80] M. Lie, K. B. Klepper, O. Nilsen, H. Fjellvag and A. Kjekshus, "Growth of iron cobalt oxides by atomic layer deposition", *Dalton Transactions*, 253-259 (2008)

Acknowledgments

My great thank goes to Prof. Dr. Andreas Hütten, my supervisor, who without his supports and accompaniment certainly I could not be able to do this work. I am really grateful for being trusted and gained this position. I would like to thank a special person, who helped me in the beginning of my study at Bielefeld University to handle better with my new environment and to get basics knowledge about the everything that were new and strange for me and of course for her honest friendship, Dr. Britta Vogel. I am also grateful to Dr. Markus Meinert for installation the programs that I used through this work and surely for the discussions which opened me a wide view to „ab initio calculations“ thema, without his helps, this work would not be performed. I would like also to thank my colleagues in D2 for the nice time that I had with them.

Above all I would like to appreciate my dear parents, who supported and accompanied me through all my education with their patience and blessing and undoubtedly I am appreciative to all my brothers and sisters, who helped and reinforced me through this way.

I would like also to thank Mr. Matthias Anwander and Mr. Gerhard Ahlers, IT supporters. And finally I would like to thank administrative ladies, especially Mrs. Ute Tiede and Mrs. Elke Siedlaczek, who made it to me more pleasant to work next to them with their friendly attitude.

And at last, I am thankful to all those people, who have had significant role in my education but they have not been mentioned here.